Suppression of Friction-Induced Oscillations through Use of High-Frequency Dither Signals

A Dissertation
Presented to
The Academic Faculty

By

Michael André Michaux

In Partial Fulfillment
Of the Requirements for the Degree
Doctor of Philosophy in Mechanical Engineering

Georgia Institute of Technology
August 2005

SUPPRESSION OF FRICTION-INDUCED OSCILLATIONS THROUGH USE OF HIGH-FREQUENCY DITHER SIGNALS

Approved by:

Dr. Kenneth A. Cunefare, Advisor
School of Mechanical Engineering
Georgia Institute of Technology

Dr. Aldo A. Ferri, Advisor
School of Mechanical Engineering
Georgia Institute of Technology

Dr. Jerry H. Ginsberg
School of Mechanical Engineering
Georgia Institute of Technology

Dr. Olivier A. Bauchau
School of Aerospace Engineering
Georgia Institute of Technology

Dr. Laurence J. Jacobs
School of Civil and Environmental Engineering
Georgia Institute of Technology

Date Approved: June 15, 2005

ACKNOWLEDGEMENTS

I want to thank my advisors, Dr. Cunefare and Dr. Ferri, for their guidance and support through these last four years. I also want to thank my Ph.D. reading committee, Dr. Bauchau, Dr. Jacobs, and Dr. Ginsberg. I appreciate your time and input in this process.

TABLE OF CONTENTS

LIST OF TABLES

LIST OF FIGURES

SUMMARY

Friction-induced oscillations occur in many engineering systems, often resulting in noise, vibration, and excessive or uneven wear. This research addresses the suppression of such oscillations, especially with application to braking systems, through the use of high-frequency dither signals. Brake squeal is an annoying and elusive problem too often present in braking systems of automobiles, trucks and aircraft.

In previous work, the effectiveness of high-frequency dither to eliminate squeal in an automotive disc brake assembly was demonstrated experimentally. The main features of the dither-squeal cancellation system was the application of a high frequency variation in the brake pressure force accomplished by means of a piezoelectric stack placed behind one of the brake pads.

This thesis contains a theoretical and numerical treatment of the application of dither to frictional systems. Two types of systems are investigated. The first is a classic, mass-on-a-moving belt problem, which experiences friction-induced oscillations similar to those encountered in brake applications. The system is first studied using an analytical technique based on the method of averaging. It is shown that, depending on the system, friction, dither-waveform, and belt-speed parameters, dither can stabilize an unstable system. However, in some cases, dither can destabilize an initially stable system. These results are verified numerically using time integration. The second type of system analyzed in this thesis is an annular plate with a rotating frictional device. The method of multiple scales is used to predict subcritical regions of instability; the results are validated using Floquet theory. The thesis treats both tangential and normal dither, the latter being

closer to the brake application. It is found that normal dither, in addition to being harder to analyze, is much less effective than tangential dither.

CHAPTER 1

INTRODUCTION

Self-excited friction-induced oscillations are present in many engineering systems, provoking unwanted vibrations, noise and excessive wear. This research addresses the suppression of these types of oscillations, with an emphasis on braking system noise, through the use of high-frequency dither signals.

Brake squeal is commonly defined as a sustained, high frequency noise due to vibrations of the braking components of a vehicle during a braking action. There are three types of brake noise, depending on the frequency range: brake “judder” (<100 Hz), brake “groan” (100 – 1000 Hz), and brake “squeal” (1 – 16 kHz), the latter being the focus of this work.

Brake squeal has been a problem in the automotive industry for a long time. In the last few years, brake noise has become a key issue for the rating of vehicle brake systems [1, 2]. Squeal is a very irritating noise to the vehicle passengers and to the passers-by. The comfort issue of audible noise and tactile vibrations of brakes has become a primary attribute and design differentiator. Although the level of theoretical, analytical and experimental effort in understanding and controlling brake noises has grown dramatically, a complete cure has not yet been found.

After a century of study on brake squeal, it is not yet a fully understood phenomenon. There is no general theory to explain this complex and fugitive problem. However, a number of review papers, for example the articles of Kinkaid, et al. [3] and Mottershead [4], provide a good background introduction to the brake squeal literature.

The objective of this research is to understand the mechanisms of brake squeal and develop effective cancellation strategies using dither signals.

BACKGROUND

In this background section, a disc braking system will be a described, the main theories of brake squeal will be presented, as well as the related experimental work. Some of the different techniques to eliminate brake squeal will be listed. In particular, dither signals and different theories of stabilizability through the use of dither signals will be concentrated upon. Finally classical models in the literature of brake systems will be presented.

Disc Braking System

There are several main components to a disc brake system, which are illustrated in Figure 1.1. The rotor is a metal disc that is attached to the wheel hub and bearing by studs and lugnuts. An automobile is slowed by squeezing two brake pads, housed in a caliper, against the rotor.

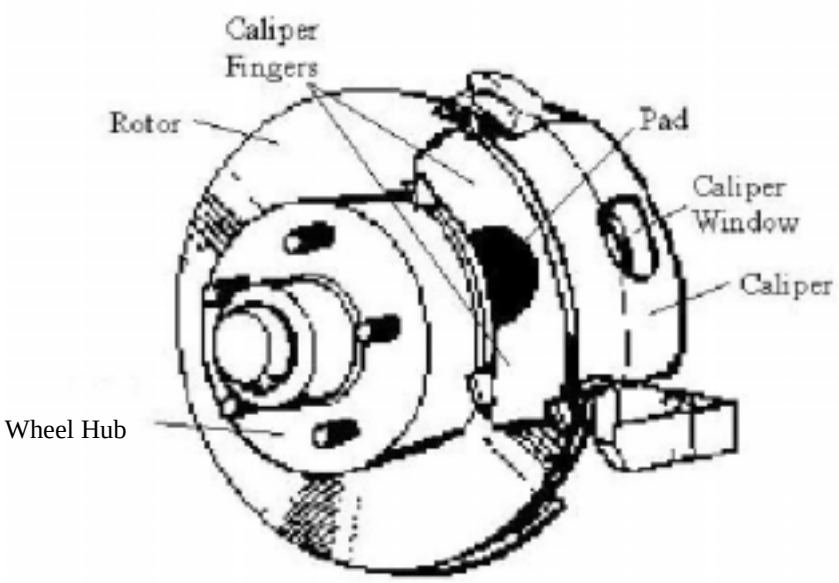

Figure 1.1: Sketch of an automobile disc brake system [5]

The brake caliper, a major component of a brake system, is shown in Figure 1.2. It shows a section of a brake system illustrating a “floating” caliper, which is used in most disc brake systems. This component houses the brake pads and pushes them against the rotor due to a reaction from the brake fluid in the reservoir during a braking application. When the brake system is installed in an automobile the portion of the caliper housing the piston is on the inboard side of the rotor.

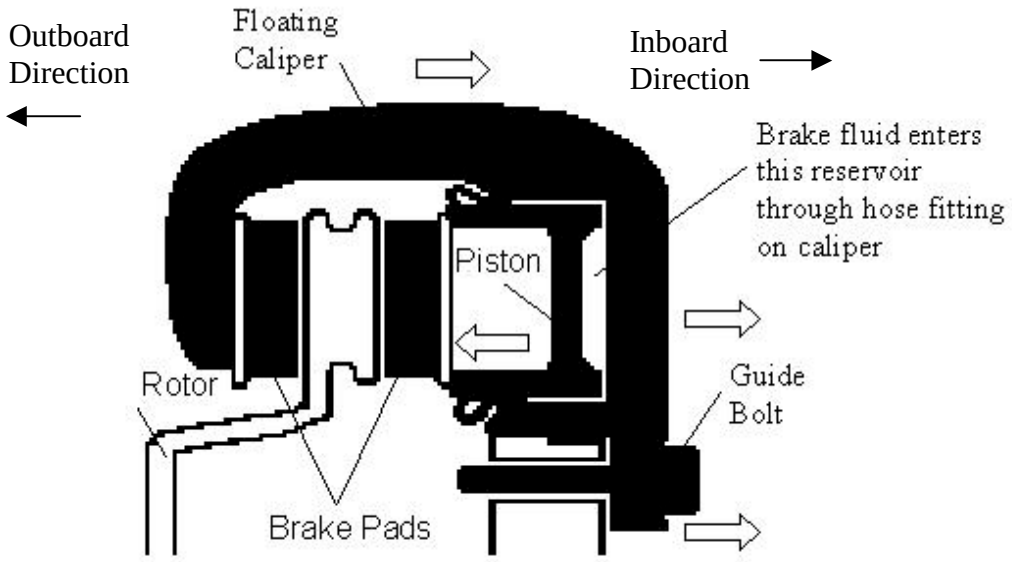

Figure 1.2: Section of a disc brake system showing the components of a “floating” caliper [5]

Brake fluid enters the reservoir in the caliper from the master cylinder. Brake fluid pressure in the reservoir causes two things to happen as the pressure increases. First, the fluid pushes on the back of the caliper piston. The piston in turn puts pressure on the inboard brake pad, which contacts the rotor. As the brake fluid pushes on the piston, it also pushes the inboard side of the caliper further inboard. This part of the caliper contains two guide bolts, which slide in a contained region of the stationary portion of the caliper. The caliper wraps around the rotor and has “fingers” on the outboard side of the brake system, which contacts the outboard brake pad. The outboard pad is pushed toward the rotor as the inboard side of the caliper is pushed inboard by the increase in brake fluid in the reservoir. Thus, the brake line pressure is transferred into brake pad pressure on both sides of the rotor.

Brake Squeal Theory

Mills [6] believed that brake squeal originated because the friction coefficient μ_k is decreasing with increasing slipping velocity v_s. It is known that this relationship can result in negative damping and lead to unstable oscillations. Although the brake squeal phenomenon is not completely explained, it is believed that the "stick-slip" action occurs between the rubbing surfaces. The variation of the friction force with the slipping velocity is the source of the self-sustained oscillations, like a violin string and its bow. This theory is commonly referred as the $\frac{d\mu_k}{dv_s} < 0$ theory of brake squeal.

Spurr [7, 8] described a new theory for brake squeal, that he named sprag-slip. The elastic deformation of the system influences the frictional force, such that the interaction between the pad and disc generates frictionally induced oscillations. This action does not depend on a coefficient of friction varying with the relative slipping velocity, but results from the geometric arrangement and flexibility of the pad.

Another theory of brake squeal contends that squeal occurs when certain types of modes coalesce. The model most often used to explore this mechanism of brake squeal uses a modal expansion for the vibration of the brake rotor [4, 9, 10]. When steady slipping is assumed, friction enters the model as a non-conservative follower force. Since the model is linear and time invariant, the stability is entirely dictated by the complex eigenvalues. If any of the eigenvalues has a positive real part, squeal is assumed to occur. Note that the magnitudes of the complex eigenvalue's real part provide no insight into the magnitude of squeal that will result. The magnitude of the real part only determines the

rate at which the oscillations approach their limit. The theory has also been used to explain instabilities in computer disc models and band brake systems.

Generic Squeal Elimination Methods

Disc brake squeal suppression methods have been investigated extensively through experiments [11-14]. Many researchers attempted to understand the effect of friction coefficient, normal load, temperature, stiffness, and damping on squeal sound level. In many experimental studies, various methods to eliminate brake squeal have been tested and documented. They include shims, tuned vibration absorbers and active control.

Shims are thin pieces of high damping material, placed between the brake pad and piston in order to dampen the vibration of the pads and rotor. The use and effectiveness of noise fix shims have been discussed by many authors [15-18]. Also, Heppes [19] and Nishizawa [20] looked at the effect of vibration damping devices. Earles [21] discussed the effects of several design changes, like the geometry and the amount of damping and stiffness in the different components of the brake.

Tuned vibration absorbers (TVA) are devices implemented to suppress the system's vibration by transferring energy to the absorber mass. They have also been employed to reduce squealing of disc brakes [22].

Active control methods have also been developed to cancel brake squeal, such as the Electronically Controlled Disc Brake Noise Canceling System proposed by Nishizawa [23]. The basis for this technique is to detect the out-of-plane vibration of the rotor and then apply a normal force so as to oppose the motion and thus reduce the amplitude of the rotor vibration. Since the system is closed loop, it must be carefully

designed to prevent control-induced instabilities from occurring. This adds to the cost, complexity and fail-safe aspects of the system.

Dither Based Squeal Cancellation

An innovative open-loop control method has been proposed by Cunefare and Graf [24]. This method involves using high-frequency disturbances, termed dither signals, to "smooth" the effect of frictional forces. This technique forms the basis of the thesis work.

Dither is defined as a high-frequency (relative to the system's characteristic frequency) low amplitude signal. Dither control is known for its ability to stabilize self-excited oscillations in nonlinear systems, by effectively changing the low-frequency dynamics of the system. It has been used in a variety of applications, such as optics, image processing, controls and communications, as noted in the survey paper of Armstrong-Helouvry et al. [25].

In the experimental setup of Cunefare and Graf [26], the dither signal was introduced through piezoceramic elements. These piezoceramic elements are small enough to fit into the brake caliper system, but able to withstand the pressure produced during braking events. A sectioned view of the caliper piston and the placement of the PZT system is shown in Figure 1.3. The caliper piston provided a convenient location for the PZT stack. The piston is a hollow cylinder with the open end in contact with the inboard brake pad, as was illustrated in Figure 1.2.

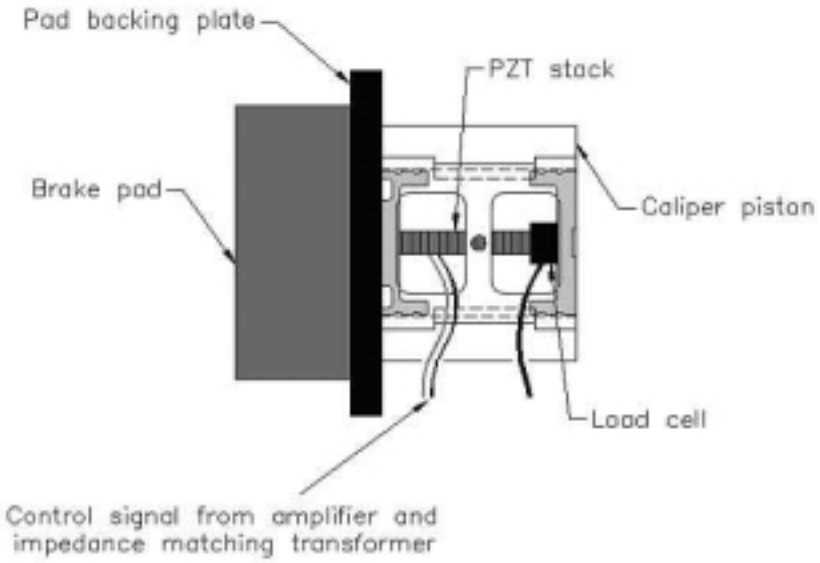

Figure 1.3: PZT control system assembled inside the caliper piston [27]

When a sinusoidal voltage is applied to the PZT stack, it expands and contracts in a similar manner, thus inducing a vibration in the caliper. The vibration is induced directly on the inboard brake pad, but it is also applied to the outboard brake pad since the caliper is of the "floating" type. The reaction of the caliper piston moving back and forth causes the brake fluid to move in and out of the caliper. This in turn causes the outboard part of the caliper and the outboard brake pad to vibrate. Essentially, the PZT system creates a rapid fluctuation in the brake pad pressure, around the static brake line pressure.

Although effective, the dither control did not cause an instantaneous cancellation of the brake squeal [24]. It was observed that the noise level of the squeal gradually decreased as the amplitude of the control signal was increased. Finally, the squeal was totally eliminated when the control signal reached a certain amplitude. This threshold is called synchronization.

The top graph in Figure 1.4 is the frequency spectrum from a nearby microphone during a 5.6 kHz squeal without dither control. The middle graph is the frequency spectrum of the noise emanating from the brake system with the activation of the 20 kHz dither control signal with an amplitude of 75 volts rms. This is a snapshot of the sound pressure from the brake system as the amplitude of the control signal was increased, but before synchronization occurred. Two distinct peaks can be seen, one at the squeal frequency and the other at the control signal frequency. Finally, the bottom graph is the frequency spectrum of the sound pressure level of the brake system with dither control once synchronization occurred for a control signal amplitude of 153 volts rms. The control system eliminated the 5.6 kHz brake squeal, leaving only the 20 kHz forced oscillations from the dither signal.

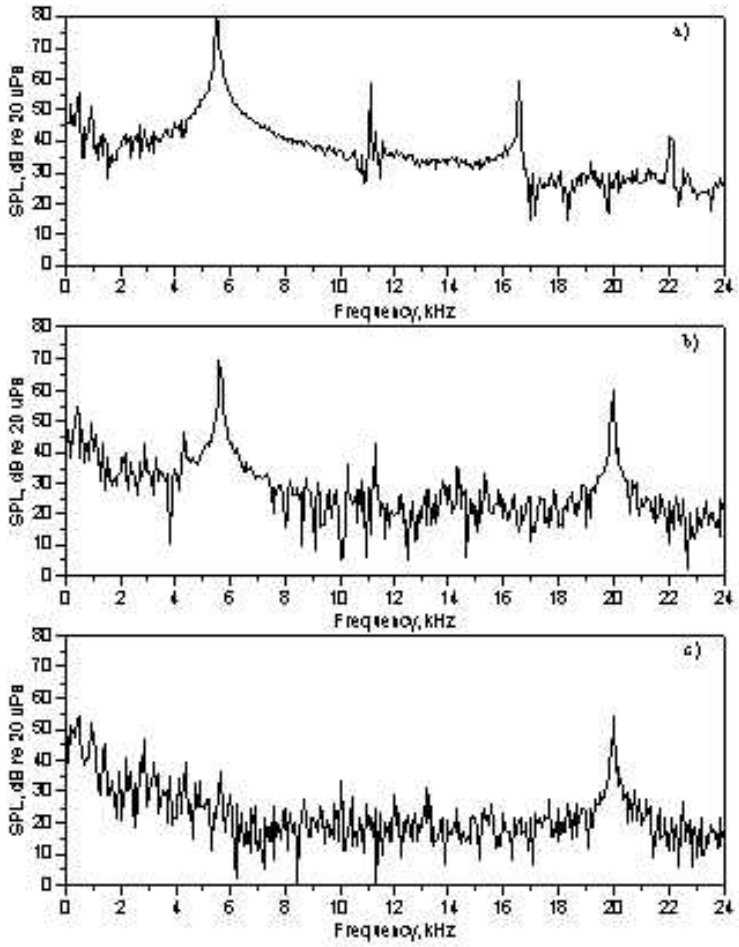

Figure 1.4: Frequency spectrum of the sound pressure level from the brake system during stages of control (top: before control activation, middle: during partial control, and bottom: after synchronization) [24]

Other Applications of Dither

The use of high frequency inputs to affect changes in system dynamics is a classical topic that has been studied for many years, dating back to the work of Floquet and Lord Rayleigh [28, 29].

Oldenburger et al. [30-32] looked at the effects of additional high frequency sinusoidal inputs to nonlinear systems. In particular, they looked at how to remove the self-oscillations of some common nonlinear systems. The authors used the “describing

function" analysis to formulate general rules concerning the effect of dither signal on the stability of given nonlinear systems with limit cycle oscillations. Their analysis concerned systems with a relay or a limiter; systems possessing a relay with dead band or a relay with hysteresis; systems with an absquare or dead band nonlinearity; and systems with a backlash element. The text by Gelb and Van Der Velde [33] further studies this analysis strategy for dual-input describing functions.

One particular strategy for this was pioneered by Meerkov [34, 35], who termed this technique vibrational control theory. In some cases, the introduction of vibration (with zero mean value) does not change the low frequency dynamics of the system. In other words, the integral dynamic properties of the system remain intact. In these cases, there is no improvement in system stability; the system remains unstable. One of Meerkov's contributions was the development of specific conditions under which stabilization was possible. Due to its simplicity, the vibrational control method is useful when conventional methods based on feedback and feedforward principles are infeasible or too expensive and complex.

The use of dither signals in frictional systems has been known for years by mechanical system designers, but it has not been extensively documented. Canudas de Wit et al. [36, 37] and Armstrong Helouvry et al. [25, 38] discussed dither signals with applications to friction control.

Omer Morgul [39, 40] focused on controlling chaotic systems using dither. Three methods have been presented for the selection of dither parameters, in the case of piece constant dither signals.

Thomsen [41-43] extensively studied how friction-induced self-excited oscillations are affected by high-frequency external excitation. The system of interest was a single degree of freedom mass on a moving belt. Analytical approximations were derived to obtain predictions of the self-excited oscillations, and predictions of the necessary frequency and amplitude of the dither signal in order to quench those self-excited oscillations.

Models of Brake Systems

Numerous models have been proposed in the literature, attempting to capture the different effects that could cause brake squeal. This research focuses on two particular types of models: lumped models and continuous type models.

Lumped Models

Lumped models, which can be single degree of freedom (SDOF) or multiple degrees of freedom (MDOF) models, are approximations of the system, in the sense that the different components of the real system are “lumped” into rigid bodies connected by springs and dampers. Lumped models have the advantage of isolating the friction effect from the structural coupling effect. These models are relevant because they allow observation of the effect of dither on the frictional force and the system stability.

The simplest model for a disc brake is a SDOF called the mass-on-moving-belt model, as depicted in Figure 1.5. It consists of a lumped mass restrained by a linear spring and viscous damping element. The mass is pressed into contact with a rigid moving surface. The SDOF model has been extensively investigated by many authors. Depending on system parameters and speed of the moving belt, sustained oscillations or

limit cycles can develop. These limit cycles are characterized by periodic oscillations having a sticking phase followed by a slipping phase. The exact nature of the limit cycle depends strongly on the friction law [22]. In fact, with some friction laws, the relative slip velocity never reaches zero. In this case, the discontinuity in the friction nonlinearity is avoided, and it is possible to apply perturbation methods to obtain analytical results. The best example of this is the work of Thomsen [41-43], who is able to derive the required threshold amplitude for which a tangential dither force can suppress the limit cycle.

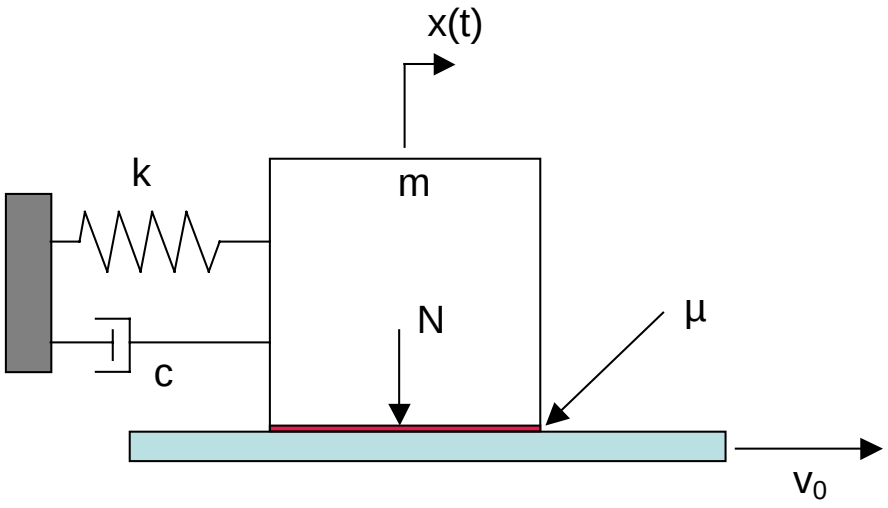

Figure 1.5: SDOF model

An extension of the SDOF model was proposed by Shin et al. [44], who developed a two-degree-of-freedom-model for a brake system. As depicted in Figure 1.6, the disc and the pad are modeled as single masses connected by a sliding friction interface. Linear and nonlinear stability analyses were performed to understand the effect of the disc and pad damping. Various limit cycles in the phase space were demonstrated.

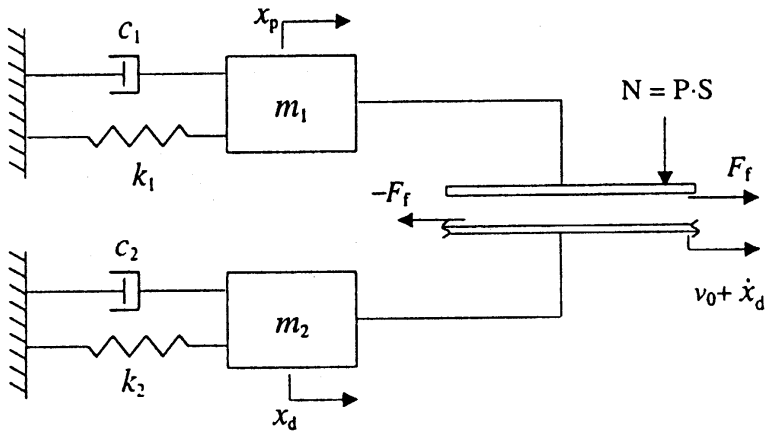

Figure 1.6: “Two-degree-of-freedom” model by Shin et al. [44]

Earles et al. [21] employed a pin-on-disc paradigm to understand brake vibration problems. They developed a five-degree-of-freedom model, as seen in Figure 1.7. The disc, represented by the central block, moves vertically upwards and its motion is resisted by the action of two pins acting on its vertical faces. The two pins are supported independently. The supports have stiffnesses normal and parallel to the disc face, and torsionally about the center. This model predicts states of unstable motions, as a function of the system parameters.

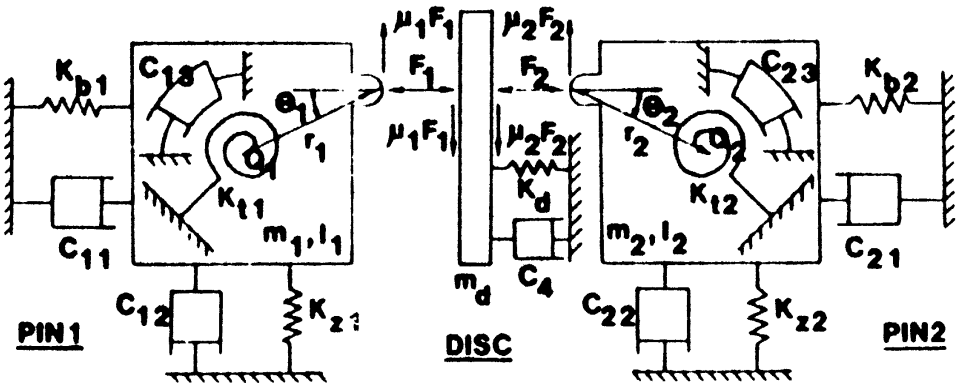

Figure 1.7: “Double-pin-on-disc” model by Earles et al. [21]

Continuous Models

Continuous, or distributed models, are richer approximations of the system compared with the lumped models. The model of the system components represents the real geometry more accurately. Typically finite element models and modal analysis techniques are employed. These more complicated models of the brake assembly permit an enrichment of the system understanding. They can exhibit the different modes coupling, and they allow interactions between normal and tangential direction displacements. These richer models should lead to more accurate results, closer to the experimental observations.

Many researchers have used continuous models for brake rotor systems and computer disc drives. Two survey papers have summarized the research area: Mottershead [4] and Kinkaid et al. [3].

Mottershead [4] gave a thorough account of the understanding gained from recent research investigations in the dynamics of discs with moving loads. The typical system of interest is shown in Figure 1.8. Two variations have been studied: a stationary disc with a rotating spring-mass-damper (SMD) system, and a stationary SMD system contacting a

spinning disc. Due to relatively low speeds encountered in brake system, the disc is usually treated as stationary. Central to a study of disc/load systems are the concepts of critical speed instability, and forward or backward traveling waves. Once the plate motion is described with an eigenfunction expansion, a trigonometric identity can be used and the solution can be interpreted as two traveling waves of speed $\pm\frac{\omega_{jn}}{j}$. The frequency ω_{jn} represents the natural frequency of mode shape with j nodal diameters and n nodal circles. The forward traveling wave is in the direction of advancing θ, and the backward wave travels in the opposite direction. When the speed of the disc is $\Omega=\frac{\omega_{jn}}{j}$, the backward traveling wave remains stationary in space, leading the system to be unstable under the action of a static load. This speed is called the critical speed of the jn^{th} mode.

Iwan and Stahl [9] investigated the dynamic response of a circular elastic disc excited by a moving mass-spring-dashpot system, similar to the one shown in Figure 1.8. Three distinct types of instability were observed. The first instability occurs at the minimum critical speed, denoted by Ω_{crit}. An instability region was located immediately above each critical speed, and was termed a stiffness instability. A final instability region was found for speeds above a certain limiting value, and was named a terminal instability. There are also many other instability regions arising as a consequence of modal interaction. Iwan and Moeller [10] extended this analysis by including the centrifugal stresses, induced by high-speed disc rotation. The main effect of rotation is to stiffen the disc, and thereby increasing its effective natural frequencies compared with those of a stationary disc.

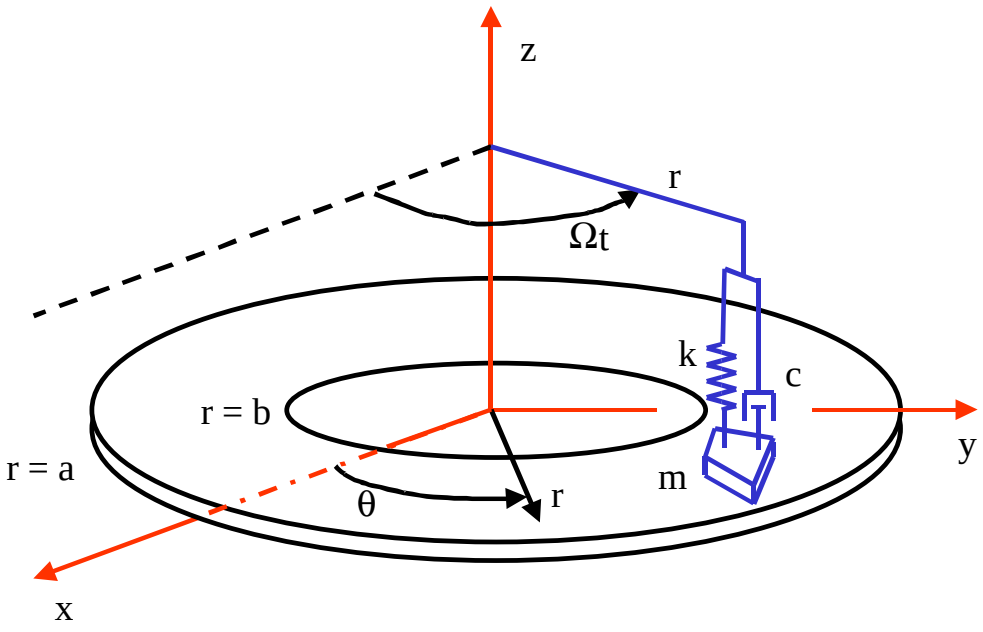

Figure1.8: Continuous plate model with mass-spring-damper system

Many variations on the Iwan and Stahl study [9] have been performed over the years. In many of the studies, the rotating SMD is treated as a small perturbation, and the method of multiple scales is used to predict analytically the unstable rotation speeds. Most studies assume steady sliding, so the friction force is constant in magnitude. Its direction, however, is always tangent to the disc surface. Thus, it manifests itself as a non-conservative follower force. Several researchers have investigated the effect of the frictional follower force [45, 46]. Ouyang et al. [47] extended the frictional follower force to include non-steady sliding. Their model also incorporated a friction coefficient that decreases with increasing velocity.

SCOPE OF THE THESIS

Objective

The goal of this research is the understanding of the effect of dither control. Using dither control as a mean for suppressing brake squeal requires the understanding of several different phenomena, such as friction, geometric instabilities and structural coupling. Characteristics of the dither signal in itself are investigated in order to obtain the best performances.

The research described in the thesis is primarily theoretical and analytical in nature. Several types of models are developed, each designed to test some aspect of the problem or to facilitate some type of analytical technique. Although the experimental setup implements “normal dither”, i.e. dither in a direction normal to the rotor, the analytical study considers both normal and tangential dither.

Lumped Model

The primary use of a SDOF is to study the stick-slip phenomenon, and the effect of $\frac{d\mu_k}{dv_s} < 0$. Chapter 2 examines sinusoidal waveforms for tangential dither. The theory is extended to general waveforms for tangential dither in Chapter 3. Chapter 4 treats the same problem for the case of normal dither. This model is simple enough to permit the application of a Thomsen-type averaging technique to understand the effect of normal and tangential dither.

Continuous model

While the above applies here too, to some extent, the primary use of continuous models is to study mode coalescence of the rotor and the resonance phenomena. In Chapter 5, a modal analysis of a continuous disc-brake model is implemented to understand the mechanisms of geometric and structural instabilities, preferred to finite element techniques for its richer basic understanding of the instability mechanisms. A stability analysis is performed to locate the unstable regions in the parameters space. Then dither signals are injected into the systems in order to understand their effect on the stability.

CHAPTER 2

SDOF WITH TANGENTIAL DITHER

This chapter examines how friction-induced oscillations are affected by high-frequency dither signals. The traditional mass-on-moving-belt system is studied using two different friction models, both exhibiting a negative friction coefficient-velocity relationship. The method of averaging is implemented and compared with numerical simulations. It is shown that there is qualitative agreement between the two approaches, but there are significant quantitative differences. This study also demonstrates how tangential dither is capable of suppressing friction-induced oscillations in many cases. However, it is also shown that dither can destabilize an initially stable system in some circumstances.

MODEL DEVELOPMENT

In this section, the governing equations for a single-degree-of-freedom (SDOF) frictional system is developed and the parameters that characterize the dither inputs are defined. The section also describes the two friction models employed in this study. Finally, a typical stick-slip oscillation is shown, as well as a numerical result showing qualitatively how dither can eliminate a sustained, stick-slip oscillation.

Equation of Motion

The SDOF model consists of a mass pressed into contact with a rigid moving surface, restrained by a linear spring and a viscous damper, as shown in Figure 2.1. The normal force, i.e. the force normal to the friction interface, consists of a constant load N ,

which models the applied braking force. The figure shows a sinusoidal tangential dither force of amplitude A_T and frequency ω_T, which is typically very large compared to the natural frequency and/or the squeal frequency of the system. In Chapter 3, the theory is extended to other types of dither waveform. The belt is assumed to move at the constant speed V_0.

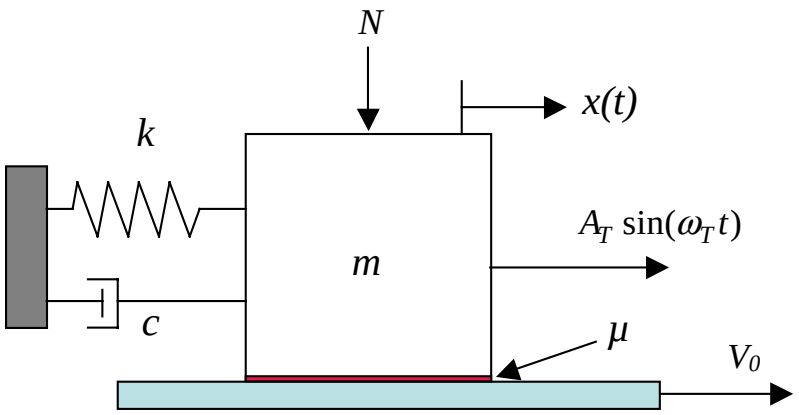

Figure 2.1: SDOF model

The non-dimensional equation of motion of the SDOF system is given by

$$\frac{d^2x}{d\tau^2} + 2\zeta\frac{dx}{d\tau} + x = f\left(\frac{dx}{d\tau}\right) + D_T \sin(R_T\tau) \tag{2.1}$$

where $\omega_0^2 = k/m$ is the system's natural frequency, $\tau = \omega_0 t$ is non-dimensional time, $\zeta = c/2\omega_0 m$ is the damping ratio, and the tangential dither frequency and amplitude ratios are denoted by $R_T = \omega_T/\omega_0$ and $D_T = A_T/k$, respectively. Note that x and D_T have units of length.

The scaled friction force f is defined as

$$f\left(\frac{dx}{d\tau}\right)=\mu(v_r)F \tag{2.2}$$

where $F=N/k$ is a scaled normal force, $v_r=v_0-dx/d\tau$ is the relative velocity or "slip velocity" of the mass, and v_0 is a scaled belt velocity, $v_0=V_0/\omega_0$. Two friction models are considered in this study.

Dynamics of Stick-Slip Transitions

While equations (2.1) and (2.2) govern the dynamics of the mass during slip, a more convenient form is used during sticking episodes. Since the belt moves with constant velocity during sticking, the sticking dynamics can be written as

$$\frac{d^2x}{d\tau^2}=0 \quad \text{and} \quad \frac{dx}{d\tau}=v_0 \tag{2.3}$$

When the slip velocity is zero, the friction coefficient is undefined, thus it becomes an unknown. The resulting static friction force, called the sticktion force, needs to be determined. The unknown sticktion force, denoted by f_s, prevents slip from taking place between the mass and the belt, and can be found by substituting (2.3) into (2.1)

$$f_s=2\zeta v_0+x(\tau)-D_T\sin(R_T\tau) \tag{2.4}$$

When the maximum allowable sticktion force is exceeded, the friction is not able to sustain the sticking phase, and therefore the system transitions back to a slipping phase. During sticking, the mass will begin to slip again if

$$\left| f_s \right| \geq \mu_s F \tag{2.5}$$

where μ_s is the magnitude of the friction coefficient at $v_r = 0$. During slipping, the mass will stick again when

$$\frac{dx}{d\tau} = v_0 \quad \text{and} \quad \left| f_s \right| \leq \mu_s F \tag{2.6}$$

Thus conditions (2.5) and (2.6) are used to alternate between sticking dynamics and slip dynamics.

Friction Models

Stribeck Friction Law

One of the friction laws that has received considerable attention is the Stribeck friction law [25]. The model is characterized by a low-velocity regime where the friction force magnitude decreases with increasing slip velocity. As the magnitude of the slip velocity increases, the friction force magnitude "flattens out." However, as the slip velocity is further increased, the friction force magnitude grows in a manner similar to viscous friction. The increase is associated with light lubrication, a feature that may or may not be appropriate for brake systems. Although many functional forms have been proposed throughout the literature, the mathematical model used by Thomsen [41, 43] is used here.

$$\mu(v_r) = \begin{cases} \mu_s sign(v_r) - \frac{3}{2}(\mu_s - \mu_m)\left(\frac{v_r}{v_m} - \frac{1}{3}\left(\frac{v_r}{v_m}\right)^3\right) & for\ v_r \neq 0 \\ \tilde{\mu}_s & for\ v_r = 0 \end{cases} \tag{2.7}$$

μ_s can be interpreted as the "static" coefficient of friction, which applies when $v_r = 0$. The parameter μ_m is the minimum coefficient of friction; the slip velocity at which this minimum friction coefficient is attained is denoted v_m. As discussed previously, if the interface sticks and $v_r = 0$ for a finite time, the friction force f_s must be determined by equilibrium considerations; this is indicated in equation (2.7) by $\tilde{\mu}_s$, which can be thought of an unknown scaling factor between f_s and the normal load. Note that the friction coefficient $\mu(v_r)$ can be positive or negative, depending on the instantaneous slip velocity v_r.

Decreasing Friction Law

A second friction law that is considered in this study is characterized by a friction coefficient that smoothly decreases with slip velocity, given by

$$\mu(v_r) = \begin{cases} \left[\mu_m + (\mu_s - \mu_m)\exp\left(-\frac{|v_r|}{v_m}\right)\right] sign(v_r) & for\ v_r \neq 0 \\ \tilde{\mu}_s & for\ v_r = 0 \end{cases} \tag{2.8}$$

As with the Stribeck model, μ_s can be interpreted as a static friction coefficient. Unlike the Stribeck model, this model does not have a high-velocity "lubricated regime" acting like a viscous friction. Instead the friction coefficient steadily decreases to a value of μ_m, which could be interpreted as the dynamic friction coefficient. The parameter v_m now

denotes the slip velocity at which $(\mu - \mu_m)$ drops to 36.8% of its initial value, $(\mu_s - \mu_m)$. Figure 2.2 depicts the described friction models, for the case of $\mu_s = 0.4$ and $\mu_m = 0.2587$.

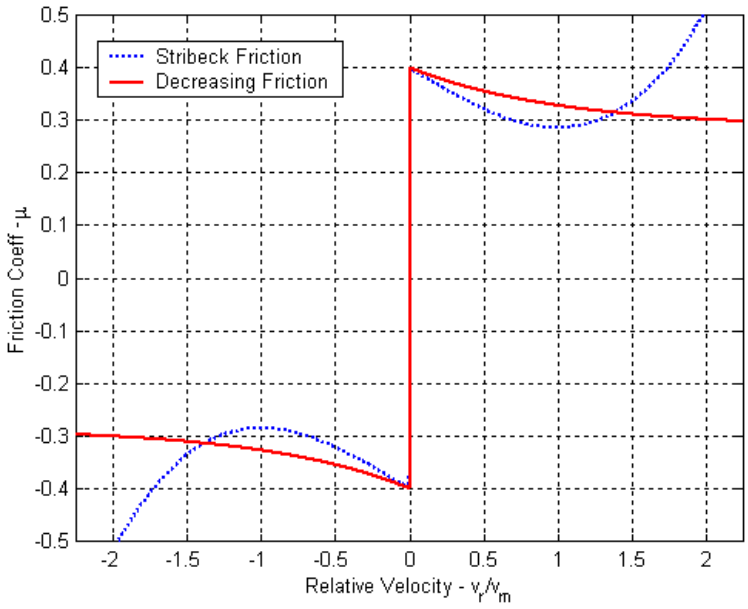

Figure 2.2: Comparison of Stribeck and decreasing friction laws. Parameters: μ_s=0.4, μ_m=0.2857.

Typical System Response

Without dither, the SDOF system described above is well known to be prone to sustained stick-slip oscillations. Figure 2.3 shows typical numerical simulation results using the Stribeck friction model and $R_T = 10$. The dashed lines denote the results for the system with no dither and the solid lines show the results for the dithered system for three different values of tangential dither amplitudes D_T.

For small amplitudes of dither (cases (a) and (b) in Figure 2.3), the response settles into a stable limit cycle after a short transient. The middle time history plot shows that the velocity exhibits episodes of sticking where the mass's velocity is exactly equal to the belt velocity. Over the same time intervals, the displacement increases linearly with time, as expected (top time history plot). This free-response stick-slip oscillation displays a fundamental frequency that is close, yet smaller than the natural frequency ($\approx 0.666\ \omega_0$ with the Stribeck friction law).

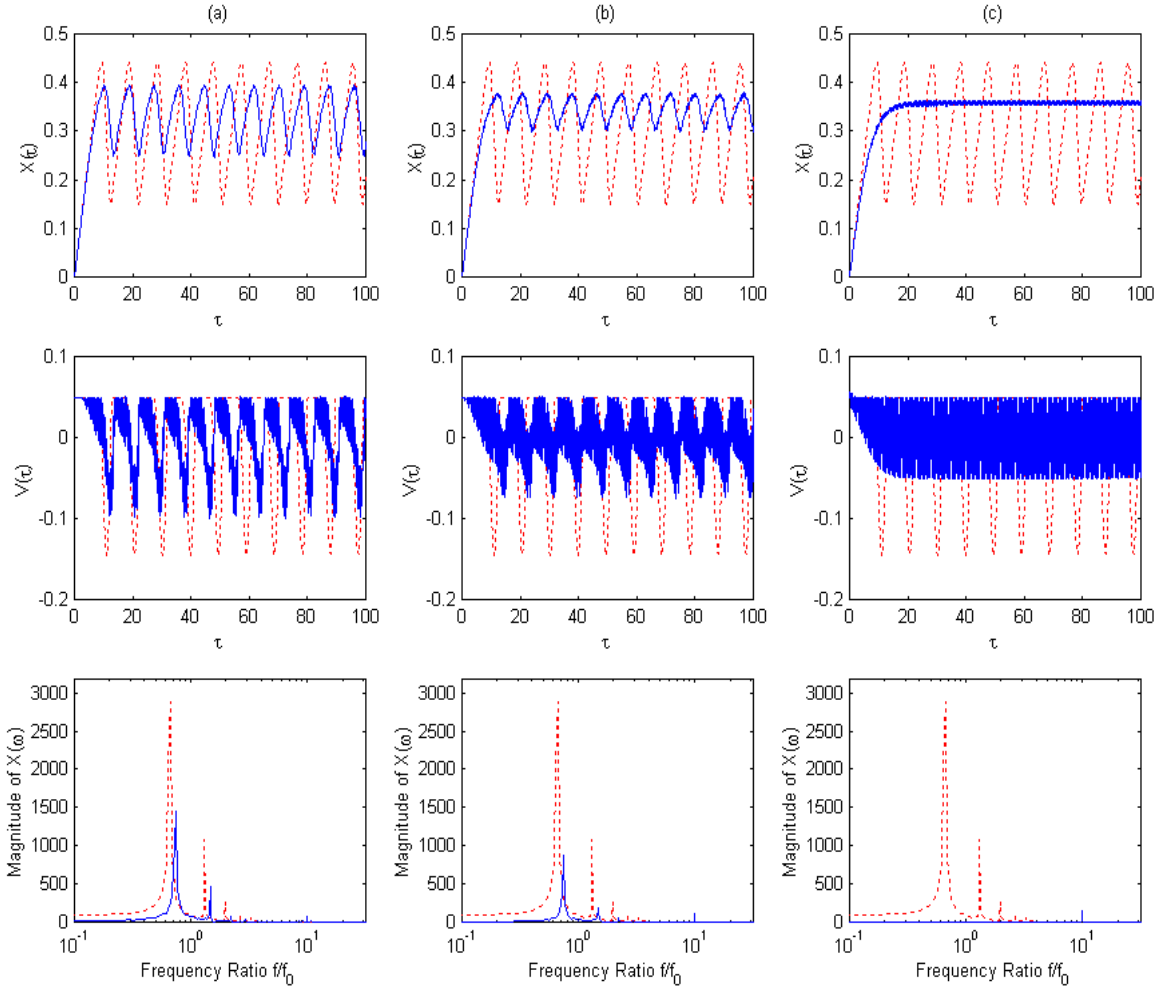

Figure 2.3: System responses with the Stribeck friction model, displacements x(τ) (top row), velocities v(τ) (middle row), and magnitude of X(ω) (bottom row) for three values of tangential dither amplitude D_T. (…) Reference case without dither excitation; (-) Dithered system. Parameters: ω_0=1, ζ=0.005, F=1, v_0=0.05, v_m=0.2, μ_s=0.4, μ_m=0.2857, R_T=10, and (a) D_T=0.3, (b) D_T=0.4, (c) D_T=0.5.

Case (a) in Figure 2.3 shows the response of the SDOF system when subjected to a tangential dither force having frequency ratio of $R_T = 10$ and amplitude $D_T = 0.3$. It is noted that the durations of sticking have been decreased a great deal, but the system still experiences a stable and sustained stick-slip oscillation, but at a higher fundamental frequency ($\approx 0.746\ \omega_0$). When the tangential dither force amplitude is increased to 0.4

and then to 0.5, the stick-slip oscillations are gradually "cancelled," as seen in cases (b) and (c) in Figure 2.3. After a brief sticking episode in the transient, the oscillations gradually decrease in amplitude. Note, however, that the oscillations do not disappear entirely. Instead, the self-excited free-response oscillations are replaced with a forced response at the frequency of the dither input. As will be shown in the following section, the amplitude of the steady-state response can be reduced further by decreasing the dither frequency ratio.

One of the goals of this research is to determine the effectiveness of the tangential dither control process as various parameters are varied. Consider, for example, the scenario depicted in the top and middle plots of Figure 2.3, corresponding to a dither frequency ratio of 10. When the dither amplitude is increased from 0.4 to 0.5, the limit cycle was suppressed. Somewhere between the two dither amplitudes is a *threshold amplitude*, which separates successful, i.e. suppression of stick-slip oscillations, from unsuccessful dither inputs. In order to pinpoint this threshold, a number of numerical simulations must be generated for some range of dither amplitudes at a single frequency ratio. It is important to emphasize that as the threshold amplitude is approached, the time duration of the transient grows longer, necessitating longer time simulations before a determination can be made for stability or instability. This procedure is repeated at each frequency ratio in order to obtain the region in the $D_T - R_T$ plane corresponding to effective dither input parameters. Unfortunately, this region also depends on the belt velocity, the damping ratio, as well as the various parameters of the friction law. With such a large space of possibilities, it is extremely useful to have an approximate,

analytical result that predicts the performance of the dither control strategy. The next section develops such an analytical result, based on the method of averaging.

Perhaps a preferable way to quantify the performance of the dither control method is using the frequency domain. The bottom plots of Figure 2.3 show the spectral estimates of the displacement signal with and without dither. Cases (a) and (b) depict "partial cancellations" because the magnitude of the signal in the vicinity of the self-excited oscillation has been reduced, but yet not completely eliminated. At the same time, there is a slight evidence of a forced response at a scaled frequency equal to R_T. At the increased amplitude of dither, case (c) shows that the signal has almost no portion in the vicinity of the uncontrolled self-excited oscillation. The self-excited oscillations have been replaced by forced oscillations at the dither frequency (and its harmonics.)

The spectral estimates reveal several aspects of the dither control strategy that must be considered in the development of a quantitative measure of effectiveness. First, as the dither amplitude is increased, the fundamental frequency of the self-excited oscillations changes slightly. Second, the stick-slip oscillations are gradually replaced by forced oscillations at the much higher dither frequency. In the brake squeal cancellation system proposed by Cunefare, et al. [26], this was not a drawback because the dither frequency that was used was in the ultrasonic frequency range. Therefore, an annoying squeal noise was replaced by an inaudible one. To measure the effectiveness of brake squeal dither control strategy, then, attention can be focused on a relatively narrow frequency range containing the squeal frequency.

METHOD OF AVERAGING

As stated in the introduction, the method of averaging has been used by a number of authors to analyze the behavior of dynamical systems subjected to high-frequency inputs and/or parametric excitation. Here, the development of Thomsen [41] is followed.

Effective Friction Law

For convenience, the equation of motion can be restated as

$$\frac{d^2x}{d\tau^2}+2\zeta\frac{dx}{d\tau}+x-D_T\sin(R_T\tau)-\mu\left(v_0-\frac{dx}{d\tau}\right)F=0 \tag{2.9}$$

The solution can be decomposed into a "fast" component, φ, and a "slow" component, Z, and written as

$$x(\tau)=Z(\tau)+\frac{1}{R_T}\varphi(\tau,R_T\tau) \tag{2.10}$$

Note that, for $R_T>>1$, the fast component is $O\left(R_T^{-1}\right)$. Also note that φ depends on two time scales. The following shorthand notation for the partial derivatives is used:

$$\dot{x}=\frac{\partial x}{\partial\tau}\qquad\text{and}\qquad x'=\frac{\partial x}{\partial(R_T\tau)} \tag{2.11}$$

Therefore, the total derivatives are given by:

$$\begin{aligned}\frac{dx}{d\tau}&=\dot{Z}+R_T^{-1}\dot{\varphi}+\varphi'\\ \frac{d^2x}{d\tau^2}&=\ddot{Z}+R_T^{-1}\ddot{\varphi}+2\dot{\varphi}'+R_T\varphi''\end{aligned} \tag{2.12}$$

Substitution of (2.12) in to (2.9), and grouping the terms according to orders of R_T yields

$$\begin{aligned}&\left\{\ddot{Z}+2\zeta\dot{Z}+Z+2\zeta\varphi'+2\dot{\varphi}'-\mu\left(v_0-\left(\dot{Z}+R_T^{-1}\dot{\varphi}+\varphi'\right)\right)F\right\}\\&+R_T\left(\varphi''\right)+R_T^{-1}\left(\ddot{\varphi}+2\zeta\dot{\varphi}+\varphi\right)=D_T\sin(R_T\tau)\end{aligned}\tag{2.13}$$

The dither amplitude is assumed to be of order R_T, thus D_T can be expressed as

$$D_T=\alpha_T R_T \quad with\ \alpha_T=O(1)\tag{2.14}$$

Equating terms of order $O(R_T)$ in equation (2.13) yields the relation

$$\varphi''-\alpha_T\sin(R_T\tau)=\mathrm{O}\left(R_T^{-1}\right)\tag{2.15}$$

Equation (2.15) can be solved for the fast component of the solution

$$\varphi(\tau,R_T\tau)=-\alpha_T\sin(R_T\tau)+\mathrm{O}\left(R_T^{-1}\right)\tag{2.16}$$

From the terms of $O(1)$ in equation (2.13), the next equation to be solved is

$$\ddot{Z}+2\zeta\dot{Z}+Z+\mu\left(\left(\dot{Z}+R_T^{-1}\dot{\varphi}+\varphi'\right)-v_0\right)F+2\zeta\varphi'+2\dot{\varphi}'=\mathrm{O}\left(R_T^{-1}\right)\tag{2.17}$$

Using equation (2.16) and its partial derivatives, this yields

$$\ddot{Z}+2\zeta\dot{Z}+Z=-\mu\left(\left(\dot{Z}-\alpha_T\cos(R_T\tau)\right)-v_0\right)F+2\zeta\alpha_T\cos(R_T\tau)+\mathrm{O}\left(R_T^{-1}\right)\tag{2.18}$$

The averaging technique is used to solve equation (2.18). The fast-time-average operator is introduced, which time-averages over one period of the fast excitation, considering the slow time τ to be fixed

$$\left\langle f\left(\tau, R_T\tau\right)\right\rangle \equiv \frac{1}{2\pi}\int_0^{2\pi} f\left(\tau, R_T\tau\right) d\left(R_T\tau\right) \tag{2.19}$$

The fast solution is assumed to be periodic in the fast time $R_T\tau$, such that the fast time average of $\varphi\left(\tau, R_T\tau\right)$ is zero

$$\left\langle \varphi\left(\tau, R_T\tau\right)\right\rangle = \frac{1}{2\pi}\int_0^{2\pi} \varphi\left(\tau, R_T\tau\right) d\left(R_T\tau\right) = 0 \tag{2.20}$$

Applying the averaging operator to equation (2.18) produces the governing equation for the slow dynamics

$$\ddot{Z} + 2\zeta\dot{Z} + Z + \bar{\mu}\left(\dot{Z} - v_0\right)F = 0 \tag{2.21}$$

where $\bar{\mu}$ is called the "effective friction characteristic," which can be thought of as a "smoothed" version of the discontinuous friction law. Using v_r to denote the slow component of the slip velocity, $\bar{\mu}$ can be expressed as

$$\bar{\mu}\left(v_r\right) = \left\langle \mu\left(v_r - \alpha_T \cos(R_T\tau)\right)\right\rangle \tag{2.22}$$

Figures 2.4 and 2.5 depict the effective friction characteristic versus v_r/v_m for the Stribeck friction model and for the decreasing friction model, respectively, for five values of α_T/v_m. Note that the effective Stribeck friction and effective decreasing friction characteristics exhibit some regions of negative sloping friction coefficient. This feature will have a strong influence on the determination of system stability.

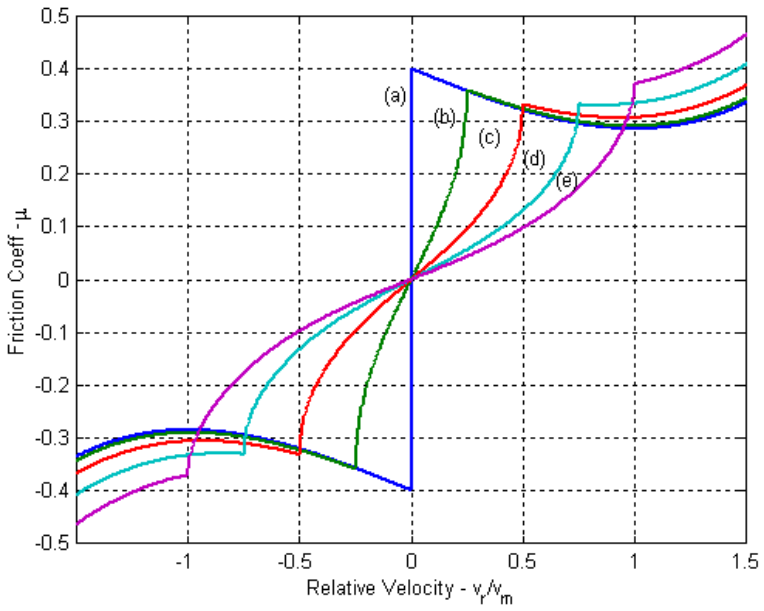

Figure 2.4: Effective Stribeck friction model for five values of tangential dither amplitude α_T. Parameters: μ_s=0.4, μ_m=0.2857, and (a) α_T/v_m=0, (b) α_T/v_m=0.25, (c) α_T/v_m=0.5, (d) α_T/v_m=0.75, (e) α_T/v_m=1.

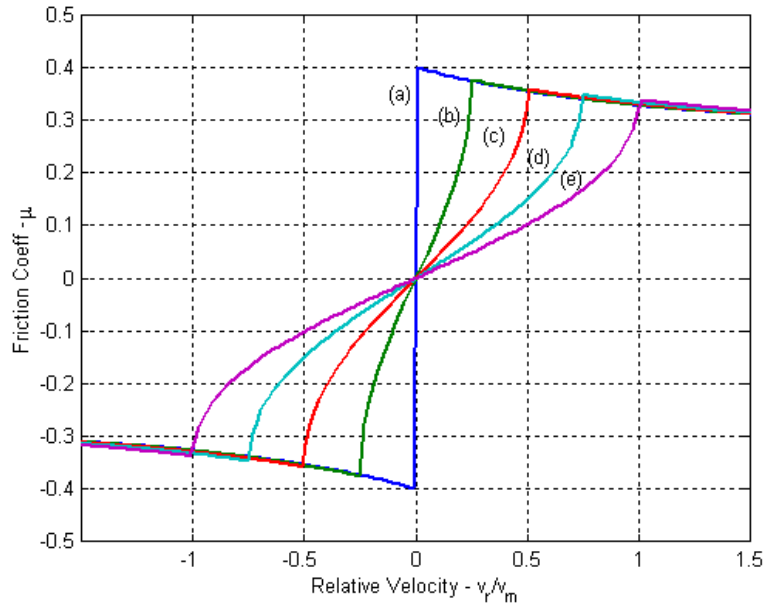

Figure 2.5: Effective decreasing friction model for five values of tangential dither amplitude α_T. Parameters: μ_s=0.4, μ_m=0.2857, and (a) α_T/v_m=0, (b) α_T/v_m=0.25, (c) α_T/v_m=0.5, (d) α_T/v_m=0.75, (e) α_T/v_m=1.

Stability Criterion

The static equilibrium, denoted $\bar{Z}$, of the slow dynamics can be obtained by setting $\ddot{Z} = \dot{Z} = 0$ in equation (2.21) to yield

$$\bar{Z} = -\bar{\mu}(-v_0)F \tag{2.23}$$

To study stability of the system, small perturbations about equilibrium are considered, $z(\tau) = Z(\tau) - \bar{Z}$. Inserting $z(\tau)$ into equation (2.21) one finds

$$\ddot{z} + h(\dot{z}) + z = 0 \tag{2.24}$$

where the function $h(\dot{z})$ incorporates the effective friction term and the viscous damping term

$$h(\dot{z}) = 2\zeta\dot{z} + F\left(\bar{\mu}(\dot{z} - v_0) - \bar{\mu}(-v_0)\right) \tag{2.25}$$

The system's equivalent damping is obtained by taking the first derivative of $h(\dot{z})$. If it is negative, then (2.23) is unstable, and self-excited vibrations will take place. Thus, the criterion for instability is given by

$$\frac{dh(\dot{z})}{d\dot{z}} = 2\zeta + \bar{\mu}'(v_0)F < 0 \tag{2.26}$$

For a particular spring-mass-damper system and for a particular friction model, equation (2.26) can be used to generate stability maps, in the $\alpha_T - v_0$ plane. Figure 2.6 shows the stability map of the dithered system having the Stribeck friction model. Parameter combinations in the shaded region correspond to points where equation (2.26) is satisfied; i.e. where the averaging method predicts instability. The upper bound of the

unstable region decreases monotonically and the lower bound increases monotonically with α_T. This means that, if the undithered system experiences sustained oscillations, there exists a threshold level of dither $\alpha_T = \alpha_T^*$ that is able to quench the limit-cycle oscillations. It is seen that the system is stable for all belt speeds greater than $v_0 = 0.2$ (approximately). For belt speeds roughly less than 0.16, it is seen that the threshold value α_T^* grows linearly with v_0. As the belt speed increases from 0.16 to 0.2, α_T^* decreases with v_0. Due to the downward sloping upper boundary of the shaded region, one can conclude that it is impossible for the system to become destabilized by an increase in the amplitude of the dither signal. On the other hand, Figure 2.7 shows that the decreasing friction model is characterized by having a band of instability in the $\alpha_T - v_0$ plane. The undithered system is seen to be stable for belt velocities greater than 0.8 (approximately). However, because the upper edge of the shaded region increases with α_T, it is now possible to destabilize a system by increasing the dither amplitude. For example, at a belt velocity of $v_0 = 1.0$, the undithered system is stable, but dither amplitudes in the range are predicted to destabilize the system. The band shown in the Figure 2.7 extends far beyond the area displayed, however it gradually becomes more and more narrow as the belt velocity is increased.

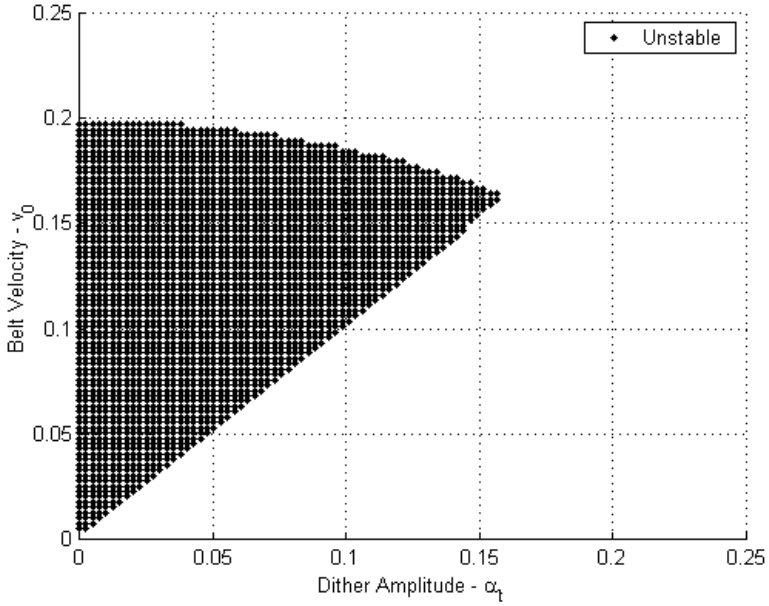

Figure 2.6: Stability map for the Stribeck friction model. Parameters: ζ=0.005, F=1, v_m=0.2, μ_s=0.4, and μ_m=0.2857.

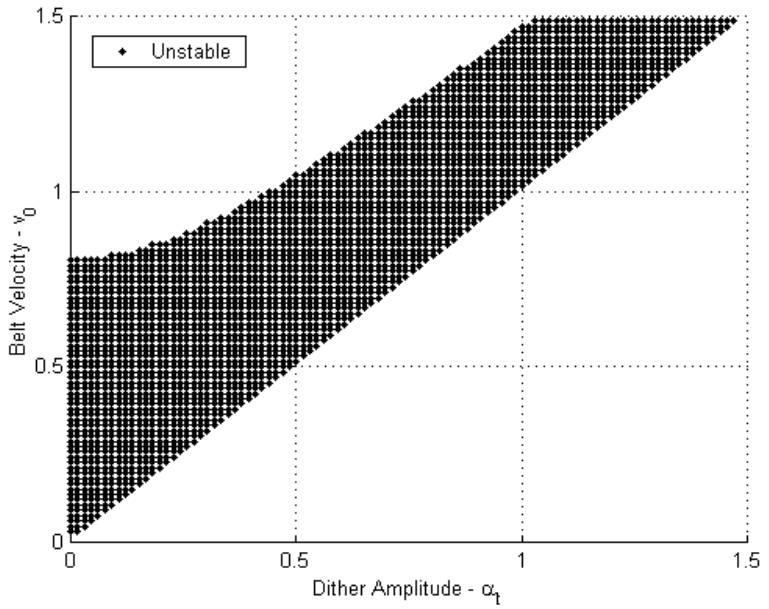

Figure 2.7: Stability map for the decreasing friction model. Parameters: ζ=0.005, F=1, v_m=0.2, μ_s=0.4, and μ_m=0.2857.

NUMERICAL RESULTS

In order to assess the accuracy of the averaging technique, an extensive numerical study was conducted. For a given set of system parameters, the response of the system was time simulated for a variety of dither amplitudes and frequencies. The simulations were performed using the Matlab function *ode45*, which uses an explicit Runge-Kutta algorithm with variable time steps. Sticking episodes are determined by careful determination of the times where the slip-velocity becomes zero. If sticking is found to take place based on the criterion of equation (2.5), the integration is continued using the "sticking dynamics" given by equations (2.3) and (2.4) until the interface breaks free again.

Two different situations are considered below. In the typical situation, the undithered system is unstable, and dither is used to eliminate the self-excited oscillations. The effectiveness of dither in this type of application is considered in the first section. In the second section, numerical integration is used to explore the opposite situation, where dither causes a stable system to become unstable.

Stabilizing Effect of Dither

In order to quantify the effectiveness of the dither cancellation technique, a numerical metric was developed that expresses the relative improvement of the dithered system to the undithered system, named dither amplitude reduction ratio

$$E = \frac{M_1}{M_0} \tag{2.27}$$

where M_1 and M_0 are the maxima of the spectral estimates of the displacement with and without the dither signal applied, respectively. In each case, the maximum is found within a frequency range that encompasses the limit-cycle oscillation. Since it is not known exactly what the fundamental frequency of the limit cycle will be, the range goes from 0 to 1.9 times the undamped natural frequency of the system.

Figure 2.8 shows contour plots of the metric E as a function of dither amplitude D_T and frequency ratio R_T for four different belt velocities, using the Stribeck friction model. The isoclines represent identical levels of reduction achieved by dither for pairs of dither parameters $R_T - D_T$. The numerical studies show that, for a constant frequency ratio, the performance increases (E decreases) as D_T is increased. On the other hand, for a constant dither amplitude, the performance increases as the frequency ratio is decreased. For sufficiently high dither frequency ratio, when $R_T > 5$, small reduction ratios less than 20% exhibit approximately linear relationships between dither amplitude and frequency ratio. Moreover the 5% reduction ratio seems to correlate very well with the threshold dither parameter obtained using the method of averaging. Note that α_T^* for a particular belt velocity v_0 will correspond to a straight line in the $R_T - D_T$ parameter space

$$D_T = \alpha_T^* \, R_T \tag{2.28}$$

The 5% isocline in the Figure 2.8 plots coincides almost exactly with the boundary predicted by (2.26). For α_T less than α_T^*, the performance gets worse as

expected. Moreover, the isoclines become less straight as the performance worsens. For example, when $E = 0.5$, the contours are fairly distorted.

Recall that the averaging results require $1/R_T$ to be a small quantity. As stated above, for $R_T > 5$, there is fairly good agreement between the stability boundaries obtained from the averaging method and the 5% performance ratio from numerical integration. The lower edge of the stability boundary of Figure 2.6 shows that there is an approximately linear relationship between α_T^* and v_0. In light of (2.26), this means that the slope of the 5% isocline should increase as v_0 increases. This is supported by the progression of plots in Figure 2.8.

Figure 2.9 presents contour plots of the metric E as a function of dither amplitude D_T and frequency ratio R_T for four different belt velocities, using the decreasing friction model. For the parameter values chosen and for the belt velocities shown in the four plots, the undithered system is unstable. For sufficiently high dither frequency ratios, when $R_T > 5$, the isoclines for small dither amplitude reduction ratios (lower than 20%) exhibit approximately linear relationships between dither amplitude and frequency ratio. The 5% reduction ratio also seems to correlate well with the stability criterion derived from the method of averaging.

While the averaging methods are relatively easy to obtain, they cannot provide any information about the performance of the dither technique aside from the stability or instability of the system. The numerical studies reveal a strong correlation between the 5% performance ratio and the averaging method's stability bound. Away from this boundary, the numerical study reveals the conditions under which different degrees of "partial cancellations" are achieved.

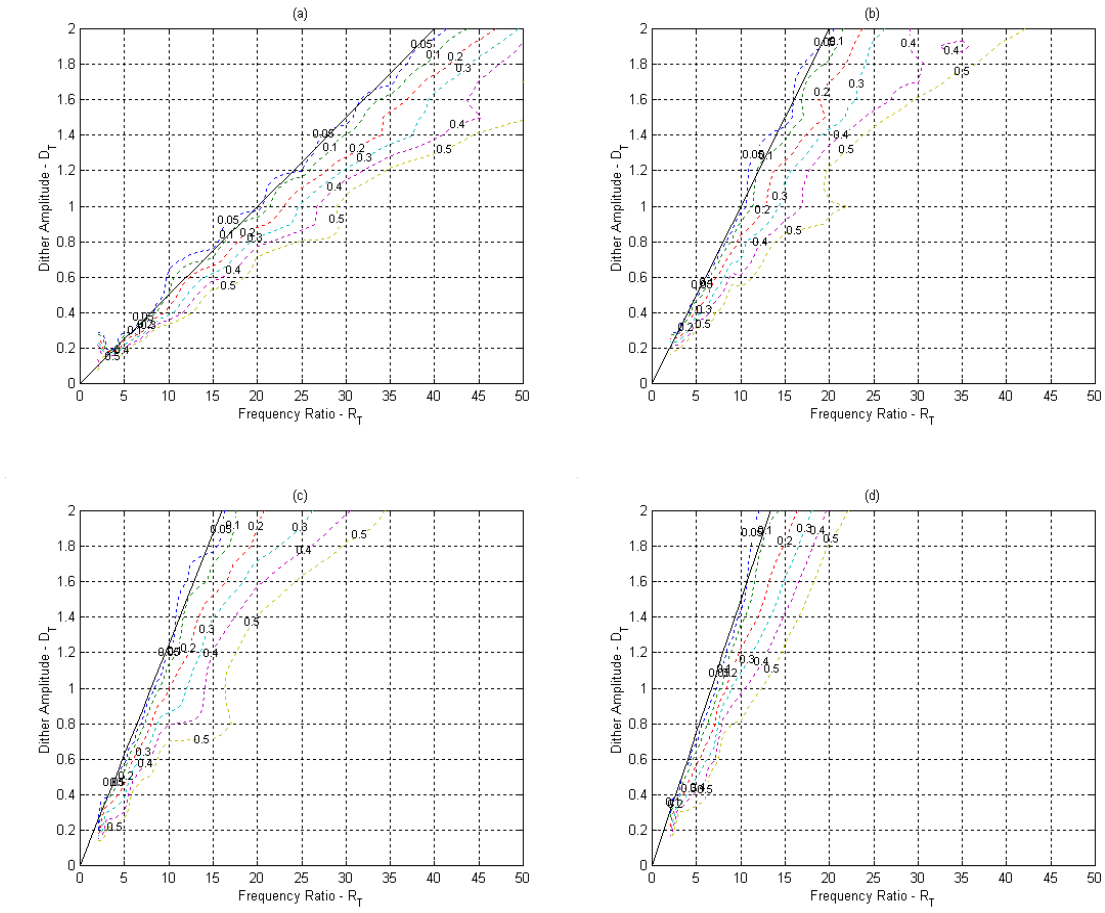

Figure 2.8: Efficiency metric using the Stribeck friction model for four values of belt velocity v_0. (…) Efficiency metric isoclines; (-) Stability boundary using the method of averaging. Parameters: ω_0=1, ζ=0.005, F=1, v_m=0.2, μ_s=0.4, μ_m=0.2857, and (a) v_0=0.05, (b) v_0=0.1, (c) v_0=0.125, (d) v_0=0.15.

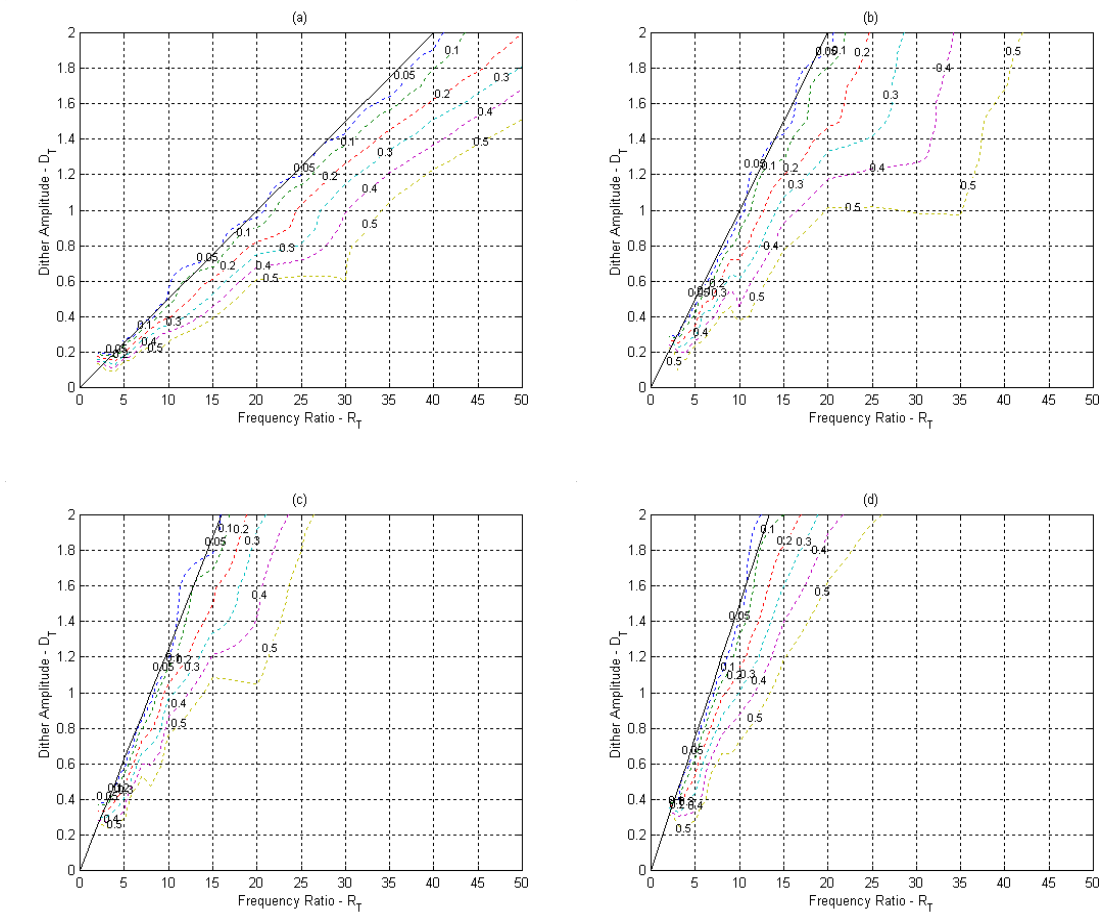

Figure 2.9: Efficiency metric using the decreasing friction model for four values of belt velocity v0. (…) Efficiency metric isoclines; (-) Stability boundary using the method of averaging. Parameters: ω_0=1, ζ=0.005, F=1, v_m=0.2, μ_s=0.4, μ_m=0.2857, and (a) v_0=0.05, (b) v_0=0.1, (c) v_0=0.125, (d) v_0=0.15.

Destabilizing Effect of Dither in the Case of the Decreasing Friction Law

When the undithered system is stable, the metric E of the previous method is not useful. In the case shown in Figure 2.7, however, it is seen that it is possible in some situations for dither to destabilize an initially stable system. To explore this further, numerical simulations are conducted holding the belt velocity and the dither frequency ratio constant, and observing the response as D_T is increased. For a system with the same

parameter values as those used in Figure 2.7, Figure 2.10 shows 6 different values of D_T when the belt velocity is $v_0 = 1$ and $R_T = 10$. The top and middle rows show the displacement and velocity response to zero initial conditions, respectively. Note that at $D_T = \alpha_T = 0$, case (a) in Figure 2.7 shows that the undithered system is stable. Thus the system should settle into a steady-sliding condition after the transient vibration dies out. The averaging method predicts that the system should become unstable for $\alpha_T = 0.43$, i.e. $D_T = \alpha_T R_T = 4.3$. The system should return to a stable state for $\alpha_T > 0.98$, which corresponds to $D_T > 9.8$. Figure 2.10 validates this qualitative behavior. However, the system becomes unstable at a lower dither amplitude, i.e. for $D_T \geq 3$. Nevertheless there is agreement with the averaging results for the return to stability prediction, as the system is stabilized for dither amplitudes $D_T \geq 10$.

The bottom row of plots in Figure 2.10 shows the Poincaré plots as D_T changes. The Poincaré section is chosen to coincide with the time instants where the dither force has maximum positive slope; $R_T \tau_n = 2n\pi$ for $n = 0, 1, 2, \ldots$ During "stable" response, the Poincaré plot spirals down to a period-1 response. When the dither signal destabilizes the system, the Poincaré plot shows a closed-orbit, closely resembling a period-10 response. It appears that the dither signal is successful in smoothing the nonlinearity, so that the low-frequency response is at or near ω_0, even though the limit-cycle oscillation occurs typically at a lower frequency. In the case of an unstable response, this sustained low-frequency response component is joined to a second component at the dither frequency.

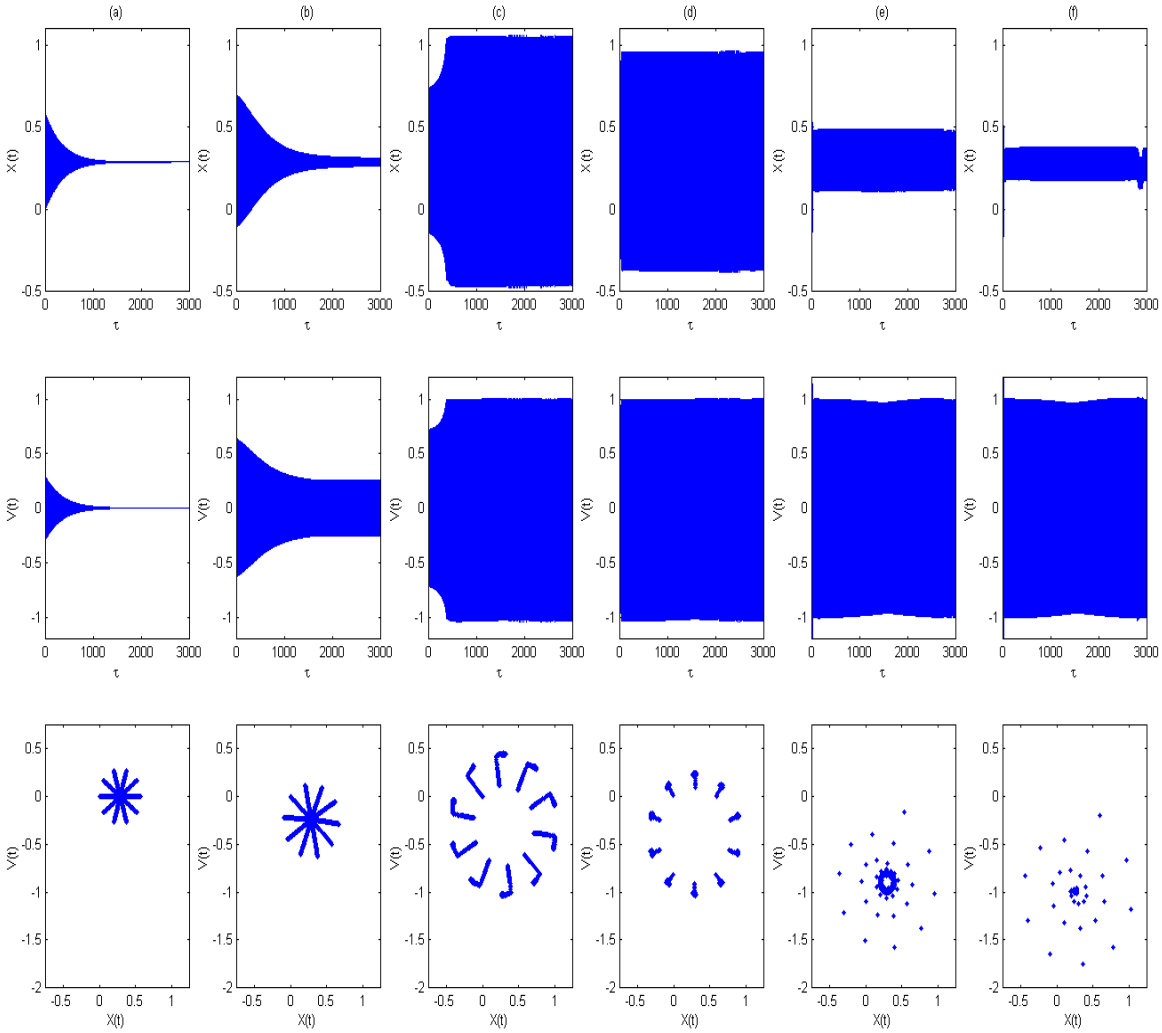

Figure 2.10: System responses with the decreasing friction model, displacements x(τ) (top row), velocities v(τ) (middle row), and Poincaré maps (bottom row) for six values of tangential dither amplitude D_T. Parameters: ω_0=1, ζ=0.005, F=1, v_0=1.0, v_m=0.2, μ_s=0.4, μ_m=0.2857, R_T=10, and (a) D_T=0, (b) D_T=2.5, (c) D_T=3, (d) D_T=4, (e) D_T=9, (f) D_T=10.

For the same system studied in Figure 2.10, Figure 2.11 shows a progression of responses for a belt velocity of $v_0 = 1.5$ and a dither frequency ratio of $R_T = 10$. From Figure 2.7, it is seen that the averaging technique predicts that the system will be unstable for $10 \le D_T \le 15$ (approximately). The numerical study shows the same qualitative trend,

but the instability occurs at a much smaller dither amplitude, $D_T = 7$. Again, the Poincaré plots show that the unstable response is period-10 at times; in some cases, the two dominant frequencies are not exactly commensurate, but show an approximate 10 to 1 ratio. In agreement with the averaging result, the system is stable again for dither amplitudes $D_T \geq 15$.

It should be mentioned that it is very difficult to pinpoint the exact value of D_T (or α_T) at which the stability of the system switches. As the boundary is approached, the duration of the transients become longer and longer. Therefore, an exhaustive numerical study was not conducted on the potential destabilizing effects of dither. However, it is clear from the numerical simulations that it is indeed possible to destabilize a system by increasing the amplitude of the dither force. This somewhat surprising result can be explained if one considers the friction model shown in Figure 2. The decreasing friction law has a negative derivative with respect to all $v_r \neq 0$, however the gradient becomes more and more shallow as the slip velocity gets larger in magnitude. If the mass is in a state of steady sliding and the belt speed is high enough, the system would be expected to be stable for small perturbations. However if the dither signal disturbs the mass enough so that the magnitude of the slip velocity gets smaller over significant time durations, friction might overcome the positive damping due to viscous damping and drive the system unstable. In the case of the Stribeck friction model, the episodes of negative frictional damping are balanced against episodes of positive damping whenever dither disturbs the steady-sliding state.

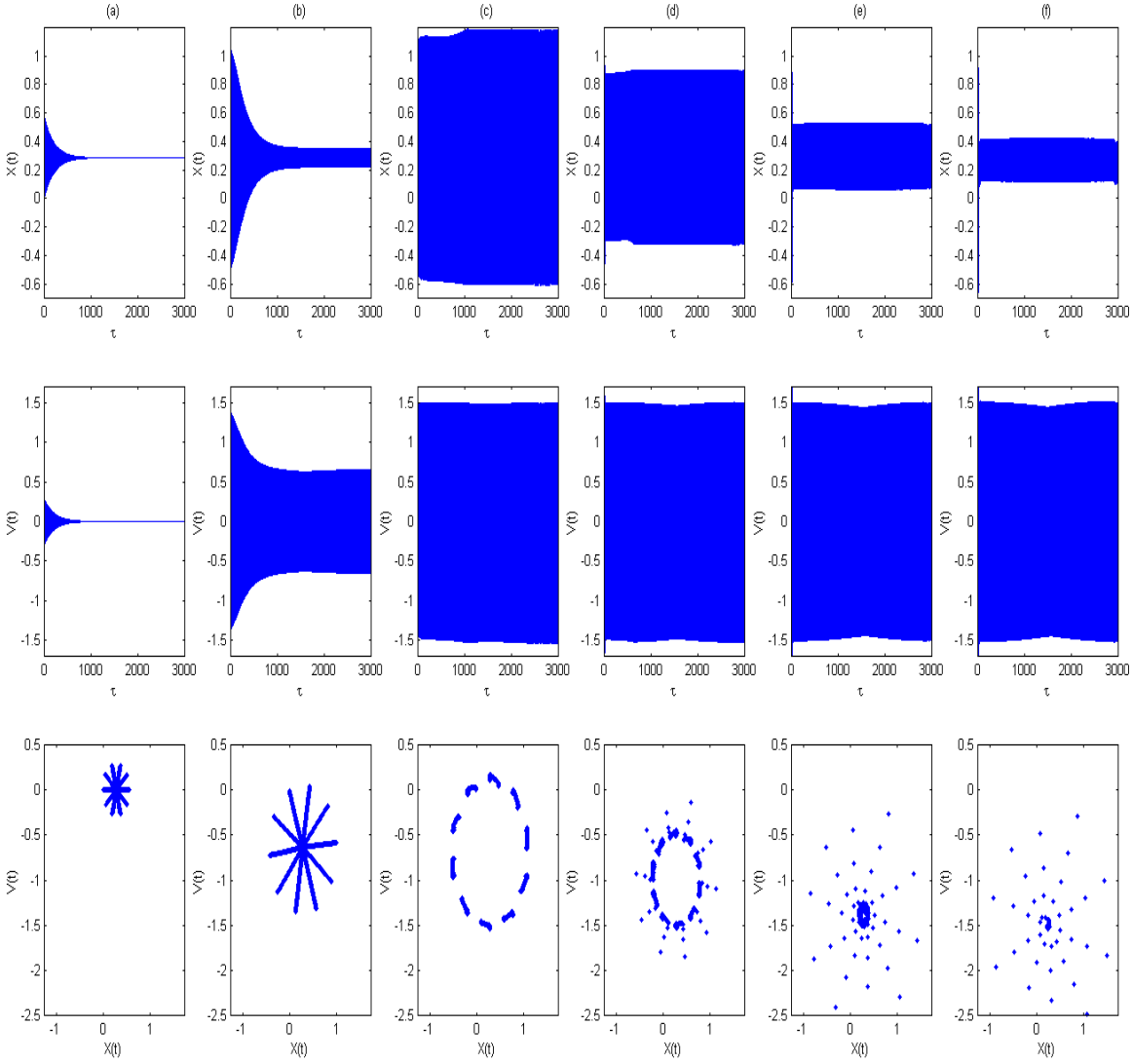

Figure 2.11: System responses with the decreasing friction model, displacements x(τ) (top row), velocities v(τ) (middle row), and Poincaré maps (bottom row) for six values of tangential dither amplitude D_T. Parameters: ω_0=1, ζ=0.005, F=1, v_0=1.0, v_m=0.2, μ_s=0.4, μ_m=0.2857, R_T=10, and (a) D_T=0, (b) D_T=6.5, (c) D_T=7, (d) D_T=10, (e) D_T=14, (f) D_T=15.

CONCLUSION

It is found that unstable, self-excited oscillations in the system having the Stribeck friction model can be stabilized by applying tangential dither of sufficient amplitude. Amplitude-frequency combinations that cause the steady-state dithered response to decrease to 5% of the undithered response show a very repeatable correlation with the stability boundary predicted by the averaging technique.

The behavior of the system with a decreasing friction law differs from that of the system with the Stribeck friction model in one important respect. While dither is found to always be a stabilizing influence in the case of the Stribeck friction model, the system with the decreasing friction model can be either stabilized or destabilized by dither. Both the averaging technique and numerical simulations show that a system undergoing stable, steady sliding can be destabilized by applying dither of intermediate strength. When the undithered system is unstable, it is always possible to find a tangential dither signal that stabilizes the system. In this case, the stability threshold predicted by the averaging technique again correlates well with the 5% performance level found using numerical integration.

CHAPTER 3

SDOF WITH TANGENTIAL DITHER OF VARIOUS WAVEFORMS

This chapter explores the effect on system stability of different waveforms for tangential dither excitation. There are several reasons for this investigation. The first is that prior research performed using the Georgia Tech brake experiment examined a variety of waveforms (for normal dither). For example, in Dzirasa [48], dither cancellation was implemented in a "burst mode." In order to reduce the power consumption, the waveform was comprised of an "on-segment" followed by an "off-segment." The on segment consisted of a prescribed number of cycles of a particular frequency. The frequency and number of cycles, the relative duration of the on-segment to the off segment as well as the period of the combined signal, were all varied to determine favorable squeal cancellation. One of the surprising findings of the waveform study was that when the duration of the on-segment was reduced below that of the off-segment, dither was unable to control the brake squeal, regardless of the frequency of the dither on-segment.

Another motivation of this study is that dither signal characteristics have been mentioned in other applications. Most notably, the book of Gelb and Vander Velde [33]. For example, the book discusses the influence of bias in a sinusoidal input, the simultaneous use of two sinusoids (dual input), the use of Gaussian random inputs. Oldenburger and Nakada [31] compared triangular and sinusoidal waveforms in terms of stabilization of limit cycles. It should be emphasized that, due to the nonlinearities present in the system, the results for a single sinusoid cannot be directly applied to the

case of general-periodic or random-input dither. Instead, each waveform must be examined individually to obtain accurate predictions of performance.

This chapter compares three different periodic waveforms when used as tangential dither signals in the SDOF system studied previously in Chapter 2: a sinusoid, a triangular waveform, and a square waveform. Each signal has zero-mean but differs in the ratio of RMS to peak value. Also, since Chapter 2 revealed different qualitative behavior for the Stribeck and decreasing friction laws, both of these friction laws are explored in this chapter. Thus, six different cases are analyzed and compared corresponding to the two different friction laws and the three different dither signals. For each of the three cases, the goal is to explore how combinations of dither amplitude and dither frequency (or dither period) influence the effectiveness of dither control strategies.

Because of the large number of different cases and parameters, it is important to have a relatively simple analytical technique so that widescale numerical simulation studies are not necessary. Here, the averaging technique of Chapter 2 is extended to general, periodic waveforms. The results are then specialized for particular waveforms and friction laws. The results from different waveforms are compared against themselves and against numerical simulation results to assess their relative performance.

MODEL DEVELOPMENT

The model used in this chapter is very similar to the one already described in Chapter 2. Here, the model is briefly stated, with the key differences highlighted. Figure 3.1 shows that the SDOF system is subjected to a tangential dither force which is denoted $A_T g(\omega_T t)$, where A_T is the amplitude and $g(.)$ is a unit-amplitude, zero-mean, periodic

waveform. The fundamental frequency of the periodic signal is given by ω_T, which is typically very large compared to the natural frequency and/or the squeal frequency of the system. In other words, the period of the periodic waveform is assumed to be $2\pi/\omega_T$. The normal force N is assumed to be constant in this chapter.

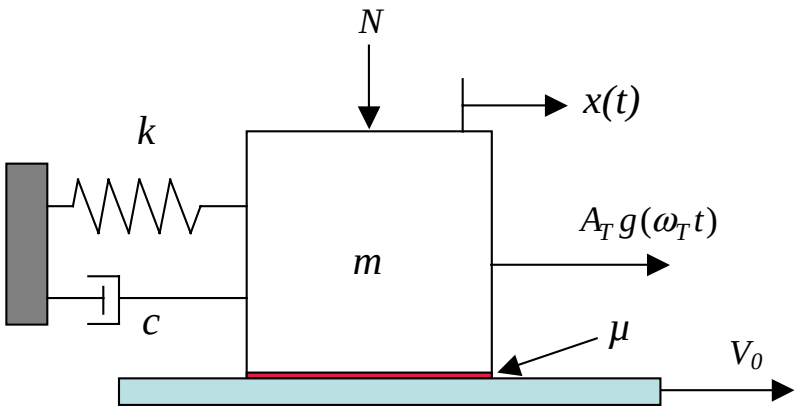

Figure 3.1: SDOF model

The non-dimensional equation of motion of the SDOF system is given by

$$\frac{d^2x}{d\tau^2} + 2\zeta\frac{dx}{d\tau} + x = f\left(\frac{dx}{d\tau}\right) + D_T g\left(R_T\tau\right) \tag{3.1}$$

where $\omega_0^2 = k/m$ is the system's natural frequency, $\tau = \omega_0 t$ is non-dimensional time, $\zeta = c/2\omega_0 m$ is the damping ratio, and the tangential dither frequency and amplitude ratios are denoted by $R_T = \omega_T/\omega_0$ and $D_T = A_T/k$, respectively. Note that x and D_T have units of length.

The scaled friction force f is defined as

$$f\left(\frac{dx}{d\tau}\right)=\mu(v_r)F \tag{3.2}$$

where $F=N/k$ is a scaled normal force, $v_r=v_0-dx/d\tau$ is the relative velocity or "slip velocity" of the mass, and v_0 is a scaled belt velocity, $v_0=V_0/\omega_0$. The friction models used in this chapter are the Stribeck and decreasing friction law, given previously in equations (2.7) and (2.8), respectively.

MATHEMATICAL FORM OF THE DITHER WAVEFORMS

In practice, the form and complexity of a dither waveform are limited only by the fidelity of the power electronics and the dynamics of the actuator. However, to limit the scope of this study, several assumptions are made regarding the dither signal $g(x)$:

1. $g(x)$ has zero-mean.
2. $g(x)$ is periodic with period 2π ; i.e., $g(x\pm n2\pi)=g(x)$, $n=0,1,2,...$
3. $g(x)$ has unit amplitude; i.e., $\max(g)=+1$, $\min(g)=-1$
4. $g(x)$ is *antiperiodic* from $[0,\pi]$ versus $[\pi,2\pi]$; i.e., $g(x\pm\pi)=-g(x)$
5. $g(x)$ is odd; i.e., $g(-x)=-g(x)$
6. $g(x)$ is of one sign over $[0,\pi]$ and is assumed to be positive

Along with the function itself, the averaging technique requires an integral of the dither signal

$$G(x)=\int g(x)dx+C \tag{3.3}$$

where the constant of integration is chosen so that $G(x)$ has zero mean.

After deriving the averaged results for the system subject to a generic signal g that meets the 6 assumptions above, the results are specialized to three waveforms: sinusoidal, triangular, and square. Two cycles of the signals and their respective zero-mean integrals are shown in Figure 3.2.

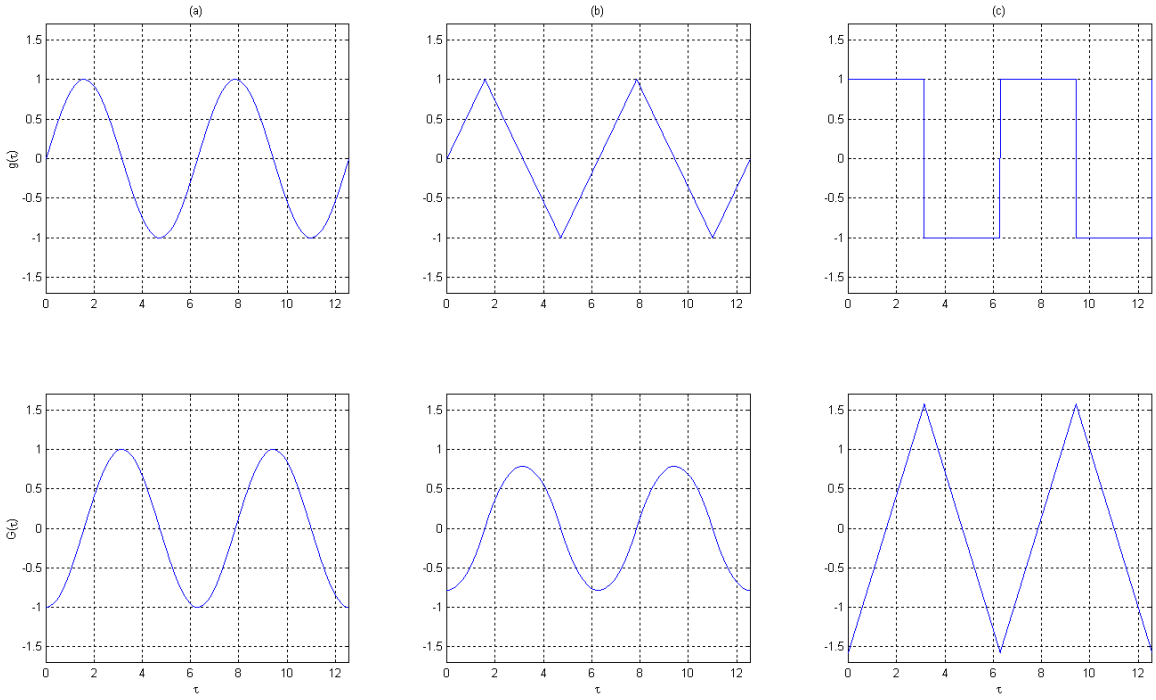

Figure 3.2: Two cycles of dither waveforms g(τ) (top row), and zero-mean integral G(τ) (bottom row). Parameters: (a) sinusoidal, (b) triangular, and (c) square.

Before proceeding, it is necessary to give the precise mathematical form for the three waveforms under consideration. Although Fourier series can be used for this purpose, it is easier to use piecewise-defined expressions as follows.

Sinusoidal Waveform

$$g(x)=\sin(x) \tag{3.4a}$$

$$G(x)=\int \sin(x)dx+C=-\cos(x) \tag{3.4b}$$

Triangular Waveform

$$g(x)=triang(x)=\begin{cases}\frac{2}{\pi}x & for\ 0\le x\le\frac{\pi}{2}\\ 2-\frac{2}{\pi}x & for\ \frac{\pi}{2}\le x\le\frac{3\pi}{2}\\ -4+\frac{2}{\pi}x & for\ \frac{3\pi}{2}\le x\le 2\pi\end{cases} \tag{3.5a}$$

$$G(x)=\int triang(x)dx+C=\begin{cases}-\frac{\pi}{4}+\frac{1}{\pi}x^2 & for\ 0\le x\le\frac{\pi}{2}\\ \frac{\pi}{4}-\frac{1}{\pi}(x-\pi)^2 & for\ \frac{\pi}{2}\le x\le\frac{3\pi}{2}\\ -\frac{\pi}{4}+\frac{1}{\pi}(x-2\pi)^2 & for\ \frac{3\pi}{2}\le x\le 2\pi\end{cases} \tag{3.5b}$$

Square Waveform

$$g(x)=sqr(x)=\begin{cases}1 & for\ 0\le x\le\pi\\ -1 & for\ \pi<x\le 2\pi\end{cases} \tag{3.6a}$$

$$G(x)=\int sqr(x)dx+C=\begin{cases}-\frac{\pi}{2}+x & for\ 0\le x\le\pi\\ \frac{3\pi}{2}-x & for\ \pi<x\le 2\pi\end{cases} \tag{3.6b}$$

Note that the constants of integration have been determined such that the signals $G(x)$ have a zero average over one fundamental period.

METHOD OF AVERAGING

In this section, the averaging technique presented in Chapter 2 is generalized to consider a periodic dither signal satisfying assumptions 1 through 6. As in Chapter 2, the solution to (3.1) is decomposed into a fast component, φ, and a slow component, Z,

$$x(\tau) = Z(\tau) + \frac{1}{R_T}\varphi(\tau, R_T\tau) \tag{3.7}$$

Note that, for $R_T >> 1$, the fast component is $O\left(R_T^{-1}\right)$. Also note that φ depends on two time scales. The following shorthand notation for the derivatives is used:

$$\dot{x} = \frac{\partial x}{\partial \tau} \qquad \text{and} \qquad x' = \frac{\partial x}{\partial (R_T\tau)} \tag{3.8}$$

Therefore, the derivatives are given by:

$$\begin{aligned} \frac{dx}{d\tau} &= \dot{Z} + R_T^{-1}\dot{\varphi} + \varphi' \\ \frac{d^2x}{d\tau^2} &= \ddot{Z} + R_T^{-1}\ddot{\varphi} + 2\dot{\varphi}' + R_T\varphi'' \end{aligned} \tag{3.9}$$

Substitution of (3.9) in to (3.6), and grouping the terms according to orders of R_T yields

$$\begin{aligned} &\left\{\ddot{Z} + 2\zeta\dot{Z} + Z + 2\zeta\varphi' + 2\dot{\varphi}' - \mu\left(v_0 - \left(\dot{Z} + R_T^{-1}\dot{\varphi} + \varphi'\right)\right)F\right\} \\ &\quad + R_T(\varphi'') + R_T^{-1}\left(\ddot{\varphi} + 2\zeta\dot{\varphi} + \varphi\right) = D_T g(R_T\tau) \end{aligned} \tag{3.10}$$

The dither amplitude is assumed to be of order R_T, thus D_T can be expressed as

$$D_T = \alpha_T R_T \quad with\ \alpha_T = O(1) \tag{3.11}$$

Equating terms of order $O(R_T)$ in equation (3.10) yields the relation

$$\varphi'' - \alpha_T g(R_T\tau) = \mathrm{O}\left(R_T^{-1}\right) \tag{3.12}$$

Equation (3.12) can be solved for the fast component of the solution

$$\varphi(\tau, R_T\tau) = \alpha_T \int G(R_T\tau)\, d(R_T\tau) + \mathrm{O}\left(R_T^{-1}\right) \tag{3.13}$$

From the terms of $O(1)$ in equation (3.10), the next equation to be solved is

$$\ddot{Z} + 2\zeta\dot{Z} + Z + \mu\left(\left(\dot{Z} + R_T^{-1}\dot{\varphi} + \varphi'\right) - v_0\right)F + 2\zeta\varphi' + 2\dot{\varphi}' = \mathrm{O}\left(R_T^{-1}\right) \tag{3.14}$$

Using equation (3.13) and its partial derivatives, this yields

$$\ddot{Z} + 2\zeta\dot{Z} + Z = -2\zeta G(R_T\tau) - \mu\left(\left(\dot{Z} + \alpha_T G(R_T\tau)\right) - v_0\right)F = \mathrm{O}\left(R_T^{-1}\right) \tag{3.15}$$

As before, the fast-time-average operator is introduced, which time-averages over one period of the fast excitation, considering the slow time τ to be fixed:

$$\left\langle f(\tau, R_T\tau)\right\rangle \equiv \frac{1}{2\pi}\int_0^{2\pi} f(\tau, R_T\tau)\, d(R_T\tau) \tag{3.16}$$

The fast solution is assumed to be periodic in the fast time $R_T\tau$, such that the fast time average of $\varphi(\tau, R_T\tau)$ is zero

$$\left\langle \varphi(\tau, R_T\tau)\right\rangle = \frac{1}{2\pi}\int_0^{2\pi} \varphi(\tau, R_T\tau)\, d(R_T\tau) = 0 \tag{3.17}$$

Note that equation (3.17) validates the omission of integration constants from (3.13).

Applying the averaging operator to equation (3.15) produces the governing equation for the slow dynamics in terms of the effective friction characteristic, $\bar{\mu}$

$$\ddot{Z} + 2\zeta\dot{Z} + Z + \bar{\mu}\left(\dot{Z} - v_0\right)F = 0 \tag{3. 18}$$

Using v_r to denote the slow component of the slip velocity, $\bar{\mu}$ can be expressed as

$$\bar{\mu}\left(v_r\right) = \left\langle \mu\left(v_r + \alpha_T G\left(R_T\tau\right)\right)\right\rangle \tag{3.19}$$

Equation (3.19) applies to any zero-mean dither signal having sufficiently short period and any friction law. In the following section, the effective friction characteristics for the two friction laws under consideration are worked out in detail.

Effective Friction Characteristic for Stribeck Friction Law

The effective friction characteristic for the Stribeck friction law can be obtained analytically, using equations (2.7) and (3.16) into (3.19)

$$\begin{aligned}\bar{\mu}\left(v_r\right) = \frac{1}{2\pi}\int_0^{2\pi} &\alpha_0 sign\left(v_r + \alpha_T G\left(R_T\tau\right)\right) + \alpha_1\left(v_r + \alpha_T G\left(R_T\tau\right)\right) \\ &+ \alpha_3\left(v_r + \alpha_T G\left(R_T\tau\right)\right)^3 d\left(R_T\tau\right)\end{aligned} \tag{3.20a}$$

where

$$\alpha_0 = \mu_s \qquad \alpha_1 = -\frac{3}{2}\frac{\left(\mu_s - \mu_m\right)}{v_m} \qquad \alpha_3 = \frac{1}{2}\frac{\left(\mu_s - \mu_m\right)}{v_m^3} \tag{3.20b}$$

Rearrangements of (3.20) lead to

$$\begin{aligned}\bar{\mu}(v_r) &= \alpha_0 \left\langle sign\left(v_r + \alpha_T G(R_T\tau)\right)\right\rangle \\ &+ \alpha_1 \left(v_r + \alpha_T \left\langle G(R_T\tau)\right\rangle\right) + \alpha_3 \left\langle \left(v_r + \alpha_T G(R_T\tau)\right)^3 \right\rangle\end{aligned} \tag{3.21}$$

Expanding the cubic term and organizing by powers of the dither fast average lead to

$$\begin{aligned}\bar{\mu}(v_r) &= \alpha_0 \left\langle sign\left(v_r + \alpha_T G(R_T\tau)\right)\right\rangle + \left(\alpha_1\alpha_T + 3\alpha_3 v_r^2 \alpha_T\right)\left\langle G(R_T\tau)\right\rangle \\ &+ \alpha_1 v_r + \alpha_3 v_r^3 + 3\alpha_3 v_r \alpha_T^2 \left\langle G(R_T\tau)^2 \right\rangle + \alpha_3\alpha_T^3 \left\langle G(R_T\tau)^3 \right\rangle\end{aligned} \tag{3.22}$$

Note that, in addition to having zero average, the signals $G(R_T\tau)$ are antiperiodic signals from 0 to π versus π to 2π; this condition leads to the following property

$$\left\langle G(x)^n \right\rangle = 0 \quad for\ n = 1,3,5,... \tag{3.23}$$

Using (3.23) in equation (3.22) yields

$$\bar{\mu}(v_r) = \alpha_0 \left\langle sign\left(v_r + \alpha_T G(R_T\tau)\right)\right\rangle + \left(\alpha_1 + 3\alpha_3\alpha_T^2 \left\langle G(R_T\tau)^2 \right\rangle\right) v_r + \alpha_3 v_r^3 \tag{3.24}$$

Note that if $|v_r| > \alpha_T G_{\max}$ then $\left(v_r + \alpha_T G(R_T\tau)\right)$ has constant sign for all $R_T\tau$, whereas if $|v_r| \le \alpha_T G_{\max}$ then

$$v_r + \alpha_T G(R_T\tau) \begin{cases} \ge 0 & for\ R_T\tau \in [R_T\tau_1, R_T\tau_2] \\ \le 0 & for\ R_T\tau \in [0, R_T\tau_1] \cup [R_T\tau_1, 2\pi] \end{cases} \tag{3.25}$$

where $R_T\tau_1$ and $R_T\tau_2$ are the solutions of $v_r + \alpha_T G(R_T\tau) = 0$, in the interval $[0, 2\pi]$. Note that $R_T\tau_2 = 2\pi - R_T\tau_1$ because the signals $G(R_T\tau)$ are odd (assumption 5).

Therefore the signum term in (3.24) is given by

$$sign\left(v_r+\alpha_T G\left(R_T\tau\right)\right)=\begin{cases}+1 & for\ R_T\tau\in\left[R_T\tau_1,R_T\tau_2\right]\\ -1 & for\ R_T\tau\in\left[0,R_T\tau_1\right]\cup\left[R_T\tau_2,2\pi\right]\end{cases} \tag{3.26}$$

The fast time average of the signum function is thus given by

$$\left\langle sign\left(v_r+\alpha_T G\left(R_T\tau\right)\right)\right\rangle=\begin{cases}1-\dfrac{2}{\pi}R_T\tau_1 & \left|v_r\right|\le\alpha_T G_{\max}\\ sign\left(v_r\right) & \left|v_r\right|\ge\alpha_T G_{\max}\end{cases} \tag{3.27}$$

The effective friction characteristic for the Stribeck friction law for any of the three waveforms under consideration is given by

$$\bar{\mu}\left(v_r\right)=\begin{cases}\alpha_0\left(1-\dfrac{2}{\pi}R_T\tau_1\right)+\left(\alpha_1+3\alpha_3\alpha_T^2\left\langle G\left(R_T\tau\right)^2\right\rangle\right)v_r+\alpha_3 v_r^3 & for\left|v_r\right|\le\alpha_T G_{\max}\\ \mu\left(v_r\right)+3\alpha_3\alpha_T^2\left\langle G\left(R_T\tau\right)^2\right\rangle v_r & for\left|v_r\right|\ge\alpha_T G_{\max}\end{cases} \tag{3.28}$$

Sinusoidal Dither Waveform

In the case of sinusoidal dither, $G_{\max}=1$, $R_T\tau_1=\arccos\left(\dfrac{v_r}{\alpha_T}\right)$, and $\left\langle G\left(R_T\tau\right)^2\right\rangle=\dfrac{1}{2}$. Using these relations combined with (3.4b), equation (3.28) reduces to the exact form given by Thomsen [41],

$$\bar{\mu}\left(v_r\right)=\begin{cases}\alpha_0\left(1-\dfrac{2}{\pi}\arccos\left(\dfrac{\left|v_r\right|}{\alpha_T}\right)\right)sign\left(v_r\right)\\ \qquad\qquad+\left(\alpha_1+\dfrac{3}{2}\alpha_3\alpha_T^2\right)v_r+\alpha_3 v_r^3 & for\left|v_r\right|\le\alpha_T\\ \mu\left(v_r\right)+\dfrac{3}{2}\alpha_3\alpha_T^2 v_r & for\left|v_r\right|\ge\alpha_T\end{cases} \tag{3.29}$$

Triangular Dither Waveform

In the case of triangular dither, $G_{\max} = \frac{\pi}{4}$, $R_T\tau_1 = \sqrt{\frac{\pi^2}{4} - \frac{\pi|v_r|}{\alpha_T}}$, and $\left\langle G\left(R_T\tau\right)^2 \right\rangle = \frac{\pi^2}{30}$. Using these relations combined with (3.5b), equation (3.28) reduces to

$$\bar{\mu}(v_r) = \begin{cases} \alpha_0\left(1 - \sqrt{1 - \frac{4}{\pi}\frac{|v_r|}{\alpha_T}}\right) sign(v_r) & \\ \qquad + \left(\alpha_1 + \frac{\pi^2}{10}\alpha_3\alpha_T^2\right)v_r + \alpha_3 v_r^3 & for\,|v_r| \le \frac{\pi}{4}\alpha_T \\ \mu(v_r) + \frac{\pi^2}{10}\alpha_3\alpha_T^2 v_r & for\,|v_r| \ge \frac{\pi}{4}\alpha_T \end{cases} \tag{3.30}$$

Square Dither Waveform

In the case of square dither, $G_{\max} = \frac{\pi}{2}$, $R_T\tau_1 = \frac{\pi}{2} - \frac{v_r}{\alpha_T}$, and $\left\langle G\left(R_T\tau\right)^2 \right\rangle = \frac{\pi^2}{12}$. Using these relations combined with (3.6b), equation (3.28) reduces to

$$\bar{\mu}(v_r) = \begin{cases} \left(\frac{2}{\pi}\frac{\alpha_0}{\alpha_T} + \alpha_1 + \frac{\pi^2}{4}\alpha_3\alpha_T^2\right)v_r + \alpha_3 v_r^3 & for\,|v_r| \le \frac{\pi}{2}\alpha_T \\ \mu(v_r) + \frac{\pi^2}{4}\alpha_3\alpha_T^2 v_r & for\,|v_r| \ge \frac{\pi}{2}\alpha_T \end{cases} \tag{3.31}$$

Effective Friction Characteristic for Decreasing Friction Law

The effective friction characteristic for the decreasing friction law can be obtained analytically, substituting equations (2.8) and (3.16) into (3.19)

$$\bar{\mu}(v_r) = \frac{1}{2\pi}\int_0^{2\pi} \alpha_0 sign(u) + \alpha_1 \exp\left(-\frac{|u|}{v_m}\right) sign(u)\; d(R_T\tau) \tag{3.32a}$$

where

$$\alpha_0 = \mu_m \qquad \alpha_1 = \mu_s - \mu_m \qquad u = v_r + \alpha_T G(R_T\tau) \tag{3.32b}$$

Rearrangements of (3.32) lead to

$$\bar{\mu}(v_r) = \alpha_0 \langle sign(u)\rangle + \alpha_1 \left\langle \exp\left(-\frac{|u|}{v_m}\right) sign(u)\right\rangle \tag{3.33}$$

Note that if $|v_r| > \alpha_T G_{\max}$ then u has the same sign as v_r for all $R_T\tau$, then

$$\langle sign(u)\rangle = sign(v_r) \tag{3.34a}$$

$$\begin{aligned}\left\langle \exp\left(-\frac{|v_r + \alpha_T G(R_T\tau)|}{v_m}\right) sign(u)\right\rangle \\ = \exp\left(-\frac{|v_r|}{v_m}\right)\left\langle \exp\left(-sign(v_r)\frac{\alpha_T}{v_m} G(R_T\tau)\right)\right\rangle sign(v_r)\end{aligned} \tag{3.34b}$$

On the other hand, if $|v_r| \le \alpha_T G_{\max}$ then the signum function in (3.33) is determined by equation (3.26), because it is dependent on the dither waveform only, then

$$\left\langle sign(u)\right\rangle = \left(1-\frac{2}{\pi}R_T\tau_1\right)sign(v_r) \tag{3.35a}$$

$$\begin{aligned}\left\langle \exp\left(-\frac{|u|}{v_m}\right)sign(u)\right\rangle &= \frac{1}{2\pi}\int_0^{2\pi}\exp\left(-\frac{u}{v_m}sign(u)\right)sign(u)\; d\left(R_T\tau\right)\\ &= \frac{1}{2\pi}\left[-\int_0^{R_T\tau_1}\exp\left(\frac{u}{v_m}\right)d\left(R_T\tau\right)+\int_{R_T\tau_1}^{R_T\tau_2}\exp\left(-\frac{u}{v_m}\right)d\left(R_T\tau\right)\right.\\ &\qquad \left.-\int_{R_T\tau_2}^{2\pi}\exp\left(\frac{u}{v_m}\right)d\left(R_T\tau\right)\right]\end{aligned} \tag{3.35b}$$

The effective friction characteristic for the decreasing friction law for any of the three waveforms under consideration is given by

$$\bar{\mu}(v_r) = sign(v_r)\left[\alpha_0\left(1-\frac{2}{\pi}R_T\tau_1\right)\right.$$
$$-\frac{\alpha_1}{2\pi}\int_0^{R_T\tau_1}\exp\left(\frac{v_r+\alpha_T G(R_T\tau)}{v_m}\right)d(R_T\tau)$$
$$+\frac{\alpha_1}{2\pi}\int_{R_T\tau_1}^{R_T\tau_2}\exp\left(-\frac{v_r+\alpha_T G(R_T\tau)}{v_m}\right)d(R_T\tau) \qquad for\,|v_r| \le \alpha_T G_{\max} \qquad (3.36a)$$
$$\left.-\frac{\alpha_1}{2\pi}\int_{R_T\tau_2}^{2\pi}\exp\left(\frac{v_r+\alpha_T G(R_T\tau)}{v_m}\right)d(R_T\tau)\right]$$

$$\bar{\mu}(v_r) = sign(v_r)\left[\alpha_0+\frac{\alpha_1}{2\pi}\exp\left(-\frac{|v_r|}{v_m}\right)\right.$$
$$\left.\times\int_0^{2\pi}\exp\left(-sign(v_r)\frac{\alpha_T}{v_m}G(R_T\tau)\right)d(R_T\tau)\right] \qquad for\,|v_r| \ge \alpha_T G_{\max} \qquad (3.36b)$$

Sinusoidal Dither Waveform

Dither with sinusoidal waveforms requires the calculation of integrals of the type $I = \int \exp\left(a + b\cos(x)\right)dx$. Only integral (3.36b) has an analytical solution, for the case $|v_r| \ge \alpha_T$. When $|v_r| \le \alpha_T$, no closed-form integration is possible for (3.36a), thus the effective friction characteristic in this case must be evaluated numerically.

The effective friction characteristic in the case of sinusoidal waveforms, when $|v_r| \ge \alpha_T$, can be expressed as

$$\bar{\mu}(v_r) = sign(v_r)\left\{\alpha_0 + \alpha_1 I_0\left(\frac{\alpha_T}{v_m}\right)\exp\left(-\frac{|v_r|}{v_m}\right)\right\} \quad for\,|v_r| \ge \alpha_T \qquad (3.37)$$

where $I_0(.)$ is the modified Bessel function of order zero. The detailed derivation is given in Appendix A.

Triangular Dither Waveform

The effective friction characteristic in the case of triangular waveforms can be expressed as

$$\bar{\mu}(v_r)=\left\{\alpha_0\left(1-\sqrt{1-\frac{4|v_r|}{\pi\alpha_T}}\right)+\frac{\alpha_1}{2}\sqrt{\frac{v_m}{\alpha_T}}\exp\left(-\frac{|v_r|}{v_m}-\gamma\right)\right.$$
$$\times\left(erf\left(\sqrt{\gamma}\right)-erf\left(\sqrt{\gamma-\frac{|v_r|}{v_m}}\right)+erfi\left(\sqrt{\gamma}\right)\right) \qquad for\,|v_r|\le\frac{\pi}{4}\alpha_T \quad (3.38a)$$
$$\left.-\frac{\alpha_1}{2}\sqrt{\frac{v_m}{\alpha_T}}\exp\left(\frac{|v_r|}{v_m}-\gamma\right)erfi\left(\sqrt{\gamma-\frac{|v_r|}{v_m}}\right)\right\}sign(v_r)$$

$$\bar{\mu}(v_r)=sign(v_r)\left\{\alpha_0+\frac{\alpha_1}{2}\exp\left(-\frac{|v_r|}{v_m}\right)\sqrt{\frac{v_m}{\alpha_T}}\right.$$
$$\left.\times\left[\exp(\gamma)erf\left(\sqrt{\gamma}\right)+\exp(-\gamma)erfi\left(\sqrt{\gamma}\right)\right]\right\} \qquad for\,|v_r|\ge\frac{\pi}{4}\alpha_T \quad (3.38b)$$

where $\gamma=\frac{\pi\alpha_T}{4v_m}$, where $erf(.)$ is the error function, defined as $erf(x)\equiv\frac{2}{\sqrt{\pi}}\int_0^x e^{-t^2}dt$, and $erfi(.)$ is the imaginary error function, defined as $erfi(x)\equiv\frac{2}{\sqrt{\pi}}\int_0^x e^{t^2}dt$. The detailed derivation is given in Appendix B.

Square Dither Waveform

The effective friction characteristic in the case of square waveforms can be expressed as

$$\bar{\mu}(v_r) = \frac{2\alpha_0}{\pi\alpha_T} v_r + \frac{2\alpha_1}{\pi}\frac{v_m}{\alpha_T}\exp\left(-\frac{\pi\alpha_T}{2v_m}\right)\sinh\left(\frac{v_r}{v_m}\right) \qquad for\,|v_r| \le \frac{\pi}{2}\alpha_T \quad (3.39a)$$

$$\bar{\mu}(v_r) = sign(v_r)\left\{\alpha_0 + \frac{2\alpha_1 v_m}{\pi\alpha_T}\exp\left(-\frac{|v_r|}{v_m}\right)\sinh\left(\frac{\pi\alpha_T}{2v_m}\right)\right\} \quad for\,|v_r| \ge \frac{\pi}{2}\alpha_T \quad (3.39b)$$

The detailed derivation is given in Appendix C.

Figures 3.3 shows the effective friction characteristic versus v_r/v_m for the Stribeck friction model for 5 different values of dither amplitude. Parts (a), (b), and (c) of the figure correspond to the sinusoidal, triangular, and square dither waveforms, respectively. Several interesting things may be discerned from these figures. First, it is seen that, in each case, dither acts to smooth the friction discontinuity in the vicinity of the zero-slip point, i.e. $|v_r| \le \alpha_T G_{\max}$. As the amplitude of the dither waveform is increased, the discontinuity is smoothed over a wider range of slip velocities. Secondly, it is seen that the slope of effective friction law is dependent both on the amplitude and type of dither waveform. Recall from Chapter 2 that the instability of the averaged system is dictated by the slope of the effective friction characteristic, in particular, by the extent of the negative-sloping region. It is seen that the effective friction law exhibits a negative slope in the approximate range of $\alpha_T G_{\max} \le v_r \le v_m$. Thus, the higher $G_{\max}$ is, the smaller the slip-velocity range for negative slope. For the three dither signals under consideration, $G_{\max} = 1,\ \frac{\pi}{4},\ and\ \frac{\pi}{2}$ respectively, for the case of sinusoidal, triangular, and square dither waveforms.

Figure 3.4 shows the corresponding effective friction characteristics for the decreasing friction law. Note that the effective characteristic for the decreasing friction

model with sinusoidal dither has been obtained via a numerical evaluation of equation (3.36a).

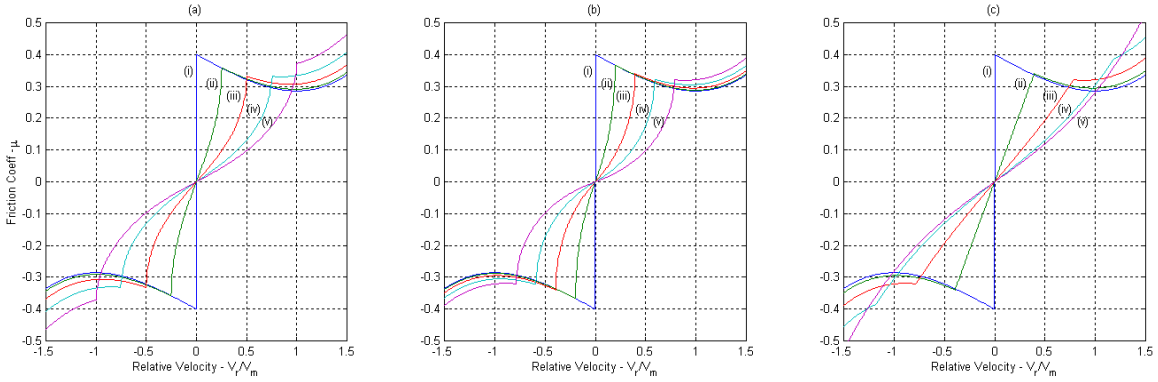

Figure 3.3: Effective Stribeck friction model for three waveforms (a) sinusoidal, (b) triangular, (c) square, for five values of tangential dither amplitude α_T. Parameters: μ_s=0.4, μ_m=0.2857, and (i) α_T/v_m=0, (ii) α_T/v_m=0.25, (iii) α_T/v_m=0.5, (iv) α_T/v_m=0.75, (v) α_T/v_m=1.

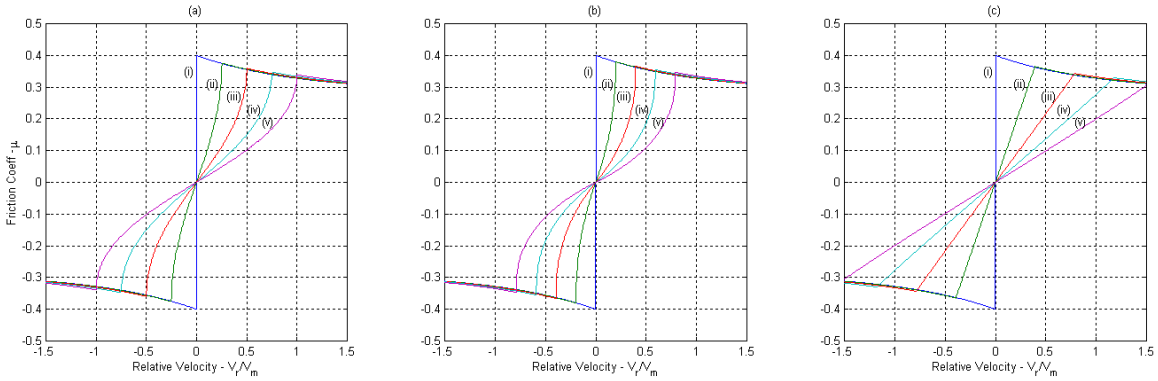

Figure 3.4: Effective decreasing friction model for three waveforms (a) sinusoidal, (b) triangular, (c) square, for five values of tangential dither amplitude α_T. Parameters: μ_s=0.4, μ_m=0.2857, and (i) α_T/v_m=0, (ii) α_T/v_m=0.25, (iii) α_T/v_m=0.5, (iv) α_T/v_m=0.75, (v) α_T/v_m=1.

Stability Boundaries

It may be noted that, except for the form of $\bar{\mu}$, the slow dynamics are given by (3.18), which is exactly the same as in equation (2.21). Thus instability is indicated by (2.26):

$$\frac{dh(\dot{z})}{d\dot{z}} = 2\zeta + \bar{\mu}'(v_0)F < 0 \tag{3.40}$$

This relation is now specialized for particular friction laws and for particular dither waveforms.

Stribeck Friction Law

The stability boundary for the Stribeck friction law can be obtained analytically using equation (3.40) and the first derivative of the effective friction characteristic, given by equations (3.29), (3.30) and (3.31), for sinusoidal, triangular and square waveforms, respectively.

The first derivative of the effective friction characteristic in the case of sinusoidal waveforms can be obtained using equations (3.29)

$$\bar{\mu}'(v_r) = \frac{2\alpha_0}{\pi\sqrt{\alpha_T^2 - v_r^2}} + \alpha_1 + \frac{3}{2}\alpha_3\alpha_T^2 + 3\alpha_3 v_r^2 \quad for\,|v_r| \le \alpha_T \tag{3.41a}$$

$$\bar{\mu}'(v_r) = \mu'(v_r) + \frac{3}{2}\alpha_3\alpha_T^2 \quad for\,|v_r| \ge \alpha_T \tag{3.41b}$$

where $\mu'(v_r) = 3\alpha_3\left(v_r^2 - v_m^2\right)$.

From (3.41a), it can be shown that $\bar{\mu}'(v_0) \geq 0$ for $|v_0| \leq \alpha_T$, thus the system is always stable in that belt velocity range. For higher belt velocity, i.e. in the range $|v_0| \geq \alpha_T$, the criterion for instability, using (3.40), in the case of sinusoidal waveforms can be written as

$$2\zeta + 3\alpha_3 F\left[v_0^2 - v_m^2 + \frac{1}{2}\alpha_T^2\right] < 0 \quad for\, |v_0| \geq \alpha_T \tag{3.42}$$

Therefore, the system will be unstable if

$$\alpha_T \leq v_0 \leq v_m\sqrt{1-\frac{1}{2}\left(\frac{\alpha_T}{v_m}\right)^2 - \frac{4v_m\zeta}{3F(\mu_s - \mu_m)}} \tag{3.43}$$

In other words, the system with sinusoidal dither will be stable at any belt velocity if $\alpha_T \geq \alpha_T^L$, where

$$\alpha_T^L = v_m\sqrt{\frac{2}{3}}\sqrt{1-\frac{4v_m\zeta}{3F(\mu_s - \mu_m)}} \tag{3.44}$$

The first derivative of the effective friction characteristic in the case of triangular waveforms can be obtained using equations (3.30)

$$\bar{\mu}'(v_r) = \frac{2\alpha_0}{\sqrt{\alpha_T\pi}\sqrt{\pi\alpha_T - 4|v_r|}} + \alpha_1 + \frac{\pi^2}{16}\alpha_3\alpha_T^2 + 3\alpha_3 v_r^2 \quad for\, |v_r| \leq \frac{\pi}{4}\alpha_T \tag{3.45a}$$

$$\bar{\mu}'(v_r) = \mu'(v_r) + \frac{\pi^2}{16}\alpha_3\alpha_T^2 \quad for\, |v_r| \geq \frac{\pi}{4}\alpha_T \tag{3.45b}$$

where $\mu'(v_r) = 3\alpha_3\left(v_r^2 - v_m^2\right)$.

Due to the fact that $\alpha_1 < 0$, it is difficult to determine the sign of (3.45a) for all values of v_r. Nevertheless, for the parameter values chosen, it can be shown that $\bar{\mu}'(v_0) \geq 0$ for $|v_0| \leq \frac{\pi}{4}\alpha_T$, thus the system is always stable in that belt velocity range. For higher belt velocity, i.e. in the range $|v_0| \geq \frac{\pi}{4}\alpha_T$, the criterion for instability, using (3.40), in the case of triangular waveforms can be written as

$$2\zeta + 3\alpha_3 F\left[v_0^2 - v_m^2 + \frac{\pi^2}{48}\alpha_T^2\right] < 0 \quad for\,|v_0| \geq \frac{\pi}{4}\alpha_T \tag{3.46}$$

Therefore, the system will be unstable if

$$\frac{\pi}{4}\alpha_T \leq v_0 \leq v_m\sqrt{1 - \frac{\pi^2}{48}\left(\frac{\alpha_T}{v_m}\right)^2 - \frac{4v_m\zeta}{3F(\mu_s - \mu_m)}} \tag{3.47}$$

In other words, the system with triangular dither will be stable at any belt velocity if $\alpha_T \geq \alpha_T^L$, where

$$\alpha_T^L = \frac{2}{\pi}v_m\sqrt{3 - \frac{4v_m\zeta}{F(\mu_s - \mu_m)}} \tag{3.48}$$

The first derivative of the effective friction characteristic in the case of square waveforms can be obtained using equations (3.31)

$$\bar{\mu}'(v_r) = \frac{2}{\pi}\frac{\alpha_0}{\alpha_T} + \alpha_1 + \frac{\pi^2}{4}\alpha_3\alpha_T^2 + 3\alpha_3 v_r^2 \quad for\,|v_r| \le \frac{\pi}{2}\alpha_T \tag{3.49a}$$

$$\bar{\mu}'(v_r) = \mu'(v_r) + \frac{\pi^2}{4}\alpha_3\alpha_T^2 \quad for\,|v_r| \ge \frac{\pi}{2}\alpha_T \tag{3.49b}$$

where $\mu'(v_r) = 3\alpha_3\left(v_r^2 - v_m^2\right)$.

Due to the fact that $\alpha_1 < 0$, it is difficult to determine the sign of (3.49a) for all values of v_r. Nevertheless, for the parameter values chosen, it can be shown that $\bar{\mu}'(v_0) \ge 0$ for $|v_0| \le \frac{\pi}{2}\alpha_T$, thus the system is always stable in that belt velocity range. For higher belt velocity, i.e. in the range $|v_0| \ge \frac{\pi}{2}\alpha_T$, the criterion for instability, using (3.40), in the case of triangular waveforms can be written as

$$2\zeta + 3\alpha_3 F\left[v_r^2 - v_m^2 + \frac{\pi^2}{12}\alpha_T^2\right] < 0 \quad for\,|v_r| \ge \frac{\pi}{2}\alpha_T \tag{3.50}$$

Therefore, the system will be unstable if

$$\frac{\pi}{2}\alpha_T \le v_0 \le v_m\sqrt{1 - \frac{\pi^2}{12}\left(\frac{\alpha_T}{v_m}\right)^2 - \frac{4v_m\zeta}{3F(\mu_s - \mu_m)}} \tag{3.51}$$

In other words, the system with square dither will be stable at any belt velocity if $\alpha_T \ge \alpha_T^L$, where

$$\alpha_T^L = \frac{v_m}{\pi}\sqrt{3 - \frac{4v_m\zeta}{F(\mu_s - \mu_m)}} \tag{3.52}$$

Setting $\alpha_T = 0$ in equations (3.43), (3.47) and (3.51), it can be deduced that the undithered system is stable for all belt velocities greater than $v_2^S \equiv v_m\sqrt{1 - \frac{4v_m\zeta}{3F(\mu_s - \mu_m)}}$. For belt velocities less than v_2^S, the undithered system experiences sustained oscillations. It may be noted that, for light damping, $v_2^S \simeq v_m$. Thus, when the belt velocity is higher than v_m, the undithered system is stable, a fact that might have been anticipated by the shape of the Stribeck friction law.

The upper bounds on v_0 in equations (3.43), (3.47) and (3.51) show that the upper bounds of the unstable regions decrease monotonically with α_T. Moreover the lower bounds on v_0 in equations (3.43), (3.47) and (3.51) show that the lower bounds of the unstable regions increase linearly with α_T. This means that, if the undithered system experiences sustained oscillations, there exists a threshold level of dither, denoted by α_T^*, where $\alpha_T^* \le \alpha_T^L$, that is able to quench the limit-cycle oscillations. Also, from the lower bounds in equations (3.43), (3.47) and (3.51), one can deduce that the square waveform is better than the sinusoidal waveform, which is better than the triangular waveform.

For belt velocities less than $v_1^S \equiv \alpha_T^L G_{\max}$, the threshold value α_T^* grows linearly with v_0. As the belt velocity increases from v_1^S to v_2^S, α_T^* decreases with v_0. Due to the downward sloping upper boundary of the unstable region, one can conclude that it is

impossible for the system to become destabilized by an increase in the amplitude of the dither signal.

For a particular spring-mass-damper system, equations (3.43), (3.47) and (3.51) can be used to compute the stability boundaries and generate stability maps for the Stribeck friction model in the $\alpha_T - v_0$ plane for sinusoidal, triangular and square dither signals, respectively. Figure 3.5 shows the stability map of the dithered system having the Stribeck friction model. Parameter combinations in the unstable region correspond to points where equation (3.40) is satisfied.

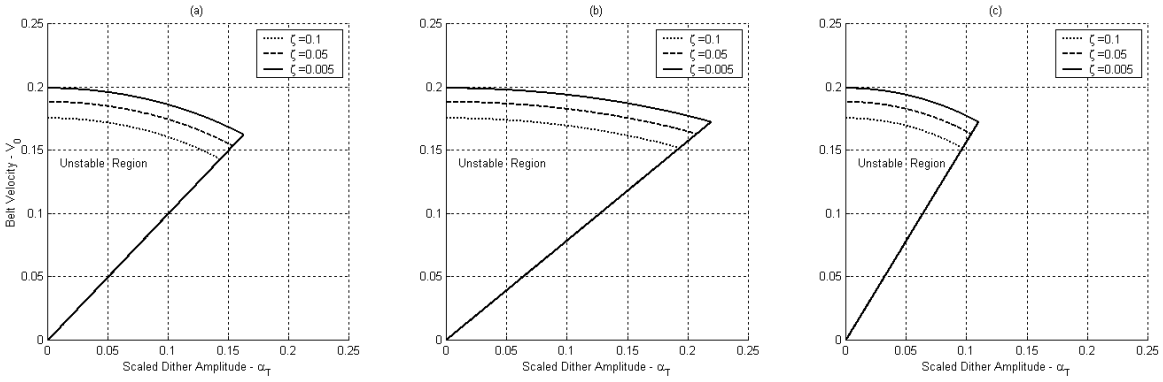

Figure 3.5: Stability map for the Stribeck friction model for three waveforms (a) sinusoidal, (b) triangular, (c) square. Parameters: ζ={0.1, 0.05, 0.005}, F=1, v_m=0.2, μ_s=0.4, and μ_m=0.2857.

Decreasing Friction Law

The stability boundary for the decreasing friction law can be obtained analytically using equation (3.40) and the first derivative of the effective friction characteristic, given by equations (3.38) and (3.39), for triangular and square waveforms, respectively. Note that the case of sinusoidal waveforms will also require a numerical evaluation.

The first derivative of the effective friction characteristic in the case of triangular waveforms can be obtained using equation (3.38)

$$\begin{aligned}\bar{\mu}'(v_r) = {} & \frac{2\alpha_0}{\pi\alpha_T}\left(1-\frac{4|v_r|}{\pi\alpha_T}\right)^{-\frac{1}{2}} + \frac{\alpha_1}{\sqrt{\pi v_m \alpha_T}}\left[1+\exp(-2\gamma)\right] \\ & -\frac{\alpha_1}{2\sqrt{v_m\alpha_T}}\exp\left(\frac{|v_r|}{v_m}-\gamma\right)\times erfi\left(\sqrt{\gamma-\frac{|v_r|}{v_m}}\right) \\ & +\frac{\alpha_1}{2\sqrt{v_m\alpha_T}}\exp\left(-\frac{|v_r|}{v_m}-\gamma\right)\times erf\left(\sqrt{\gamma-\frac{|v_r|}{v_m}}\right) \\ & -\frac{\alpha_1}{2\sqrt{v_m\alpha_T}}\exp\left(-\frac{|v_r|}{v_m}-\gamma\right)\times\left[erf\left(\sqrt{\gamma}\right)+erfi\left(\sqrt{\gamma}\right)\right]\end{aligned} \qquad for\ |v_r| \le \frac{\pi}{4}\alpha_T \quad (3.53a)$$

$$\bar{\mu}'(v_r) = -\frac{\alpha_1\delta}{2v_m}\sqrt{\frac{v_m}{\alpha_T}}\exp\left(-\frac{|v_r|}{v_m}\right) \qquad for\ |v_r| \ge \frac{\pi}{4}\alpha_T \quad (3.53b)$$

where $\gamma = \frac{\pi\alpha_T}{4v_m}$ and $\delta \equiv \exp\left(\frac{\pi\alpha_T}{4v_m}\right)erf\left(\sqrt{\frac{\pi\alpha_T}{4v_m}}\right)+\exp\left(-\frac{\pi\alpha_T}{4v_m}\right)erfi\left(\sqrt{\frac{\pi\alpha_T}{4v_m}}\right)$.

Equation (3.53a) shows that $\bar{\mu}'(v_0) \ge 0$ for $|v_0| \le \frac{\pi}{4}\alpha_T$ (for the chosen parameter values), thus the system is always stable in that belt velocity range. For higher belt velocity, i.e. in the range $|v_0| \ge \frac{\pi}{4}\alpha_T$, the criterion for instability, using (3.40), in the case of triangular waveforms can be written as

$$2\zeta + F\left[-\frac{\alpha_1\delta}{2v_m}\sqrt{\frac{v_m}{\alpha_T}}\exp\left(-\frac{|v_0|}{v_m}\right)\right] < 0 \quad for\ |v_0| \ge \frac{\pi}{4}\alpha_T \quad (3.54)$$

Therefore, the system will be unstable if

$$\frac{\pi}{4}\alpha_T \le v_0 \le -v_m \ln\left(\frac{4\zeta\sqrt{\alpha_T v_m}}{(\mu_s-\mu_m)\delta F}\right) \tag{3.55}$$

In other words, the system with triangular dither will be stable at any belt velocity if $\alpha_T \ge \alpha_T^L$, where α_T^L is the solution of the following

$$\ln\left(\frac{4\zeta v_m}{(\mu_s-\mu_m)\delta F}\sqrt{\frac{\alpha_T^L}{v_m}}\right)+\frac{\pi}{4}\frac{\alpha_T^L}{v_m}=0 \tag{3.56}$$

The first derivative of the effective friction characteristic in the case of square waveforms can be obtained using equations (3.39)

$$\bar{\mu}'(v_r)=\frac{2\alpha_0}{\pi\alpha_T}+\frac{2\alpha_1}{\pi\alpha_T}\exp\left(-\frac{\pi\alpha_T}{2v_m}\right)\cosh\left(\frac{v_r}{v_m}\right) \quad for\ |v_r| \le \frac{\pi}{2}\alpha_T \tag{3.57a}$$

$$\bar{\mu}'(v_r)=-\frac{2\alpha_1}{\pi\alpha_T}\sinh\left(\frac{\pi\alpha_T}{2v_m}\right)\exp\left(-\frac{|v_r|}{v_m}\right) \quad for\ |v_r| \ge \frac{\pi}{2}\alpha_T \tag{3.57b}$$

Equation (3.57a) shows that $\bar{\mu}'(v_0) \ge 0$ for $|v_0| \le \frac{\pi}{2}\alpha_T$ (for the chosen parameter values), thus the system is always stable in that belt velocity range. For higher belt velocity, i.e. in the range $|v_0| \ge \frac{\pi}{2}\alpha_T$, the criterion for instability, using (3.40), in the case of square waveforms can be written as

$$2\zeta + F\left[-\frac{2\alpha_1}{\pi\alpha_T}\sinh\left(\frac{\pi\alpha_T}{2v_m}\right)\exp\left(-\frac{|v_0|}{v_m}\right)\right] < 0 \quad for\ |v_0| \ge \frac{\pi}{2}\alpha_T \tag{3.58}$$

Therefore, the system will be unstable if

$$\frac{\pi}{2}\alpha_T \le v_0 \le -v_m \ln\left(\frac{\zeta\pi\alpha_T}{F(\mu_s-\mu_m)\sinh(\pi\alpha_T/2v_m)}\right) \tag{3.59}$$

In other words, the system with square dither will be stable at any belt velocity if $\alpha_T \ge \alpha_T^L$, where α_T^L is the solution of the following

$$\ln\left(\frac{\zeta\pi\alpha_T^L}{F(\mu_s-\mu_m)\sinh(\pi\alpha_T^L/2v_m)}\right)+\frac{\pi}{2}\frac{\alpha_T^L}{v_m}=0 \tag{3.60}$$

Using equations (3.55) and (3.59), it can be deduced that the undithered system is stable for all belt speeds greater than $v_2^D \equiv -v_m \ln\left(\frac{2v_m\zeta}{F(\mu_s-\mu_m)}\right)$. For belts speeds less than v_2^D, the undithered system experiences sustained oscillations.

The lower bounds on v_0 in equations (3.55) and (3.59) show that the lower bounds of the unstable regions increase monotonically with α_T. This means that, if the undithered system experiences sustained oscillations, there exists a threshold level of dither, denoted by α_T^*, where $\alpha_T^* \le \alpha_T^L$, that is able to quench the limit-cycle oscillations. For belt speeds less than v_2^D, the threshold value α_T^* grows linearly with v_0.

Unlike in the case of Stribeck friction, the upper bounds on v_0 in equations (3.55) and (3.59) show that the upper bounds of the unstable regions *increase* monotonically with α_T. Due to the upward sloping upper boundary of the unstable region, it is now possible to destabilize a stable, undithered system by injecting dither in the system. For example, at a belt velocity such that $v_0 > v_2^D$, the undithered system is stable, but

triangular dither amplitudes in the range given by (3.58), i.e. with $\alpha_T^{Triang,1} < \alpha_T < \alpha_T^{Triang,2}$ where $\alpha_T^{Triang,2} = \frac{4}{\pi} v_0$ and $\alpha_T^{Triang,1}$ is the solution of the following equation

$$\frac{\sqrt{\gamma}}{\exp(\gamma) erf\left(\sqrt{\gamma}\right) + \exp(-\gamma) erfi\left(\sqrt{\gamma}\right)} = \frac{F(\mu_s - \mu_m)\sqrt{\pi}}{8\zeta v_m} \exp\left(-\frac{v_0}{v_m}\right) \tag{3.61}$$

where $\gamma = \frac{\pi \alpha_T}{4 v_m}$, and square dither amplitudes in the range given by (3.59), i.e. with $\alpha_T^{Square,1} < \alpha_T < \alpha_T^{Square,2}$ where $\alpha_T^{Square,2} = \frac{2}{\pi} v_0$ and $\alpha_T^{Square,1}$ is the solution of the following equation

$$\frac{\pi \alpha_T / 2 v_m}{\sinh(\pi \alpha_T / 2 v_m)} = \frac{F(\mu_s - \mu_m)}{2 v_m \zeta} \exp\left(-\frac{v_0}{v_m}\right) \tag{3.62}$$

are predicted to destabilize the system.

For a particular spring-mass-damper system, equations (3.55) and (3.59) can be used to compute the stability boundaries and generate stability maps for the decreasing friction model in the $\alpha_T - v_0$ plane for triangular and square dither signals, respectively. A stability map for sinusoidal dithers requires a numerical evaluation of (3.37) in order to exploit inequality (3.40). Figure 3.6 shows the stability map of the dithered system having the decreasing friction model. Parameter combinations in the unstable region correspond to points where equation (3.40) is satisfied. Note that the band shown in the Figure 3.6 extends far beyond the area displayed for very light damping; however it gradually becomes more and more narrow as the belt speed is increased.

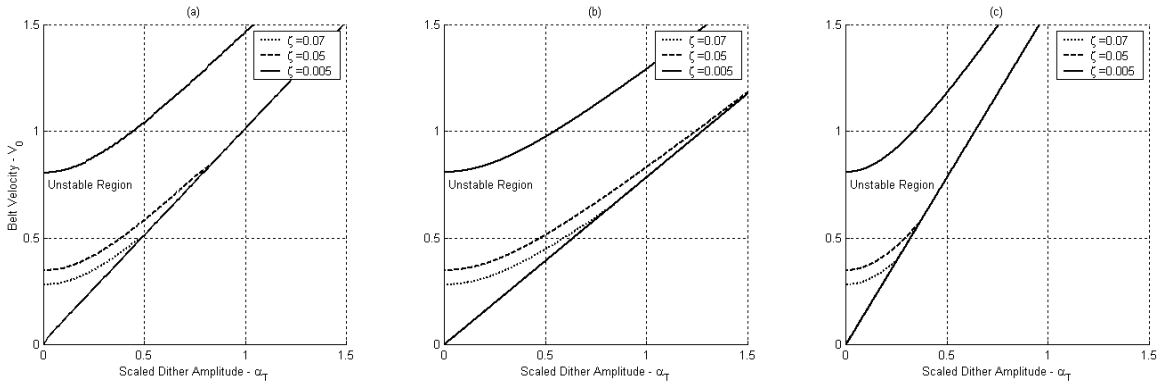

Figure 3.6: Stability map for the decreasing friction model for three waveforms (a) sinusoidal, (b) triangular, (c) square. Parameters: ζ={0.07, 0.05, 0.005}, F=1, v_m=0.2, μ_s=0.4, and μ_m=0.2857.

NUMERICAL SIMULATION STUDY

Typical system responses are first presented, and in order to assess the validity and accuracy of the predictions of the averaging technique, an extensive numerical study was conducted, similar to that conducted in Chapter 2.

Two different situations are considered below. In the typical situation, the undithered system is unstable, and dither is used to eliminate the self-excited oscillations. The effectiveness of dither in this type of application is considered in the first section. In the second section, numerical integration is used to explore the opposite situation, where dither causes a stable system to become unstable.

Typical System Response

Without dither, the SDOF system described above is well known to be prone to sustained stick-slip oscillations, as discussed in Chapter 2. The undithered system settles

into a stable limit cycle after a short transient at a fundamental frequency that is close to, yet smaller than, the natural frequency ($\approx 0.666\ \omega_0$ with the Stribeck friction law).

Figure 3.7 shows typical numerical simulation results using the Stribeck friction model and $R_T = 10$. The dashed lines denote the results for the system with no dither and the solid lines show the results for the dithered system for three different values of tangential dither amplitudes D_T, and having a sinusoidal waveform, i.e. $g(x) = \sin(x)$. Figures 3.8 and 3.9 show typical numerical simulation results using the same system parameters as for Figure 3.7, except that dither signals have triangular and square waveforms of different amplitudes, respectively.

For small amplitudes of dither (cases (a) and (b) in Figures 3.7, 3.8 and 3.9), the responses exhibit partial control, i.e. the magnitude of the signal in the vicinity of the self-excited oscillation has been reduced, but it is not yet completely eliminated. Furthermore although the durations of sticking have been decreased a great deal, the system still experiences a stable and sustained stick-slip oscillation, but at a fundamental frequency that is slightly higher than that of the undithered system ($\approx 0.746\ \omega_0$). When the tangential dither force amplitude is increased from $D_T = 0.4$ to $D_T = 0.5$ for sinusoidal dither, from $D_T = 0.5$ to $D_T = 0.7$ for triangular dither, and from $D_T = 0.3$ to $D_T = 0.4$ for square dither, depicted in case (c) in Figures 3.7, 3.8 and 3.9, respectively, the system is fully controlled by dither. In other words, the self-excited free-response oscillations are replaced with a forced response at the frequency of the dither input.

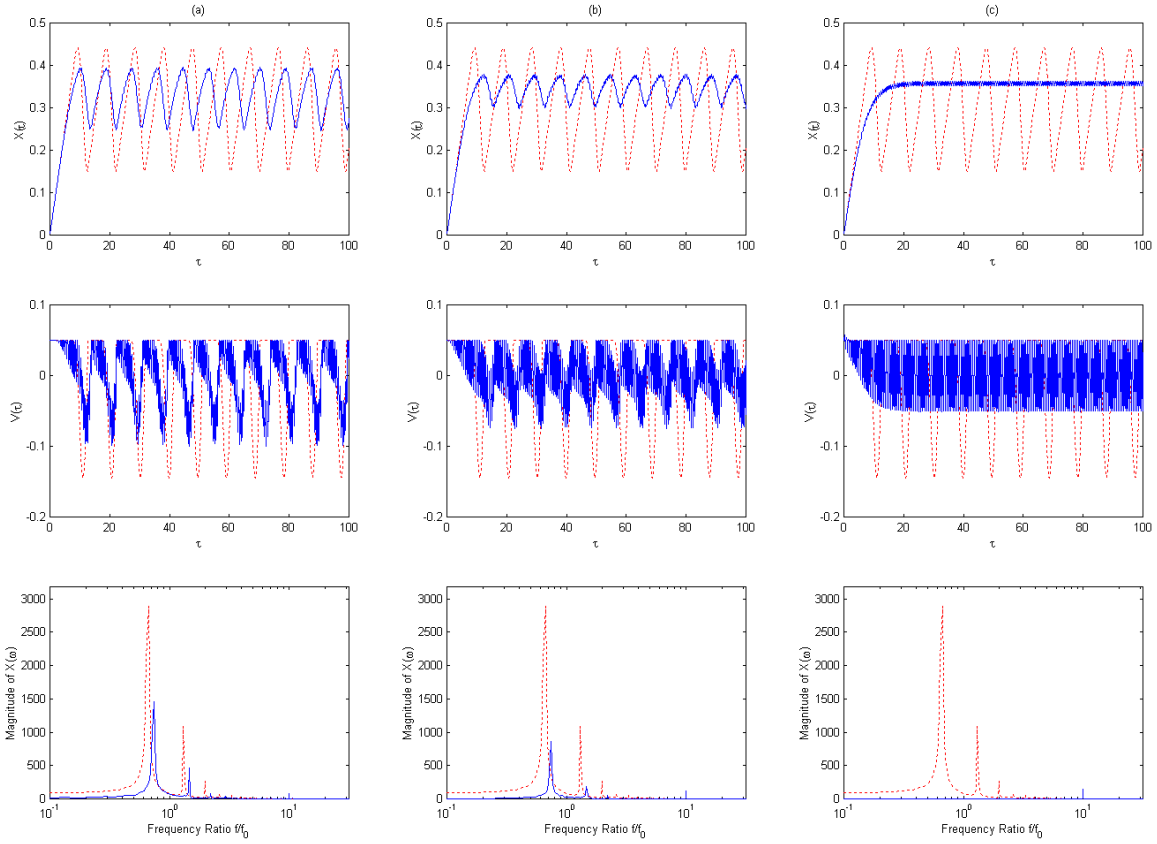

Figure 3.7: System responses with the Stribeck friction model, displacements x(τ) (top row), velocities v(τ) (middle row), and magnitude of X(ω) (bottom row) for three values of sinusoidal tangential dither amplitude D_T. (…) Reference case without dither excitation; (-) Dithered system. Parameters: ω_0=1, ζ=0.005, F=1, v_0=0.05, v_m=0.2, μ_s=0.4, μ_m=0.2857, R_T=10, and (a) D_T=0.3, (b) D_T=0.4, (c) D_T=0.5.

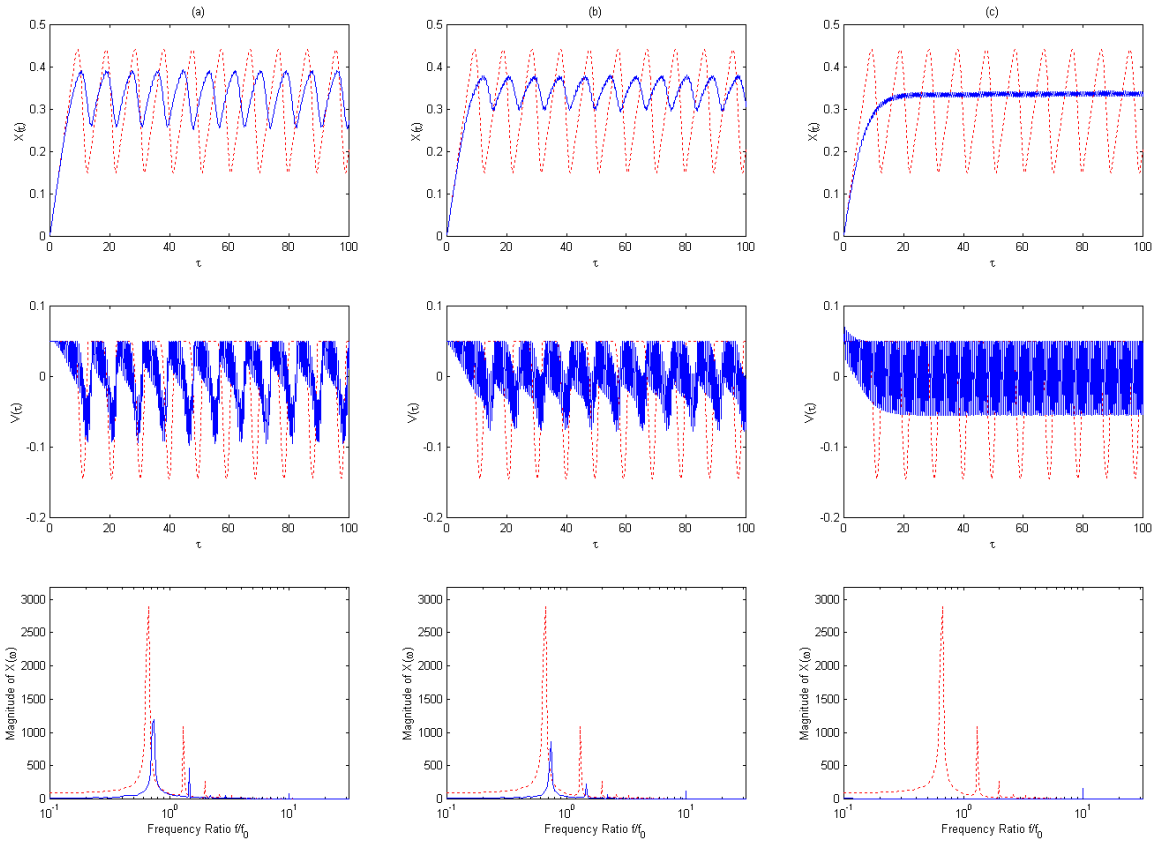

Figure 3.8: System responses with the Stribeck friction model, displacements x(τ) (top row), velocities v(τ) (middle row), and magnitude of X(ω) (bottom row) for three values of triangular tangential dither amplitude D_T. (…) Reference case without dither excitation; (-) Dithered system. Parameters: ω_0=1, ζ=0.005, F=1, v_0=0.05, v_m=0.2, μ_s=0.4, μ_m=0.2857, R_T=10, and (a) D_T=0.4, (b) D_T=0.5, (c) D_T=0.7.

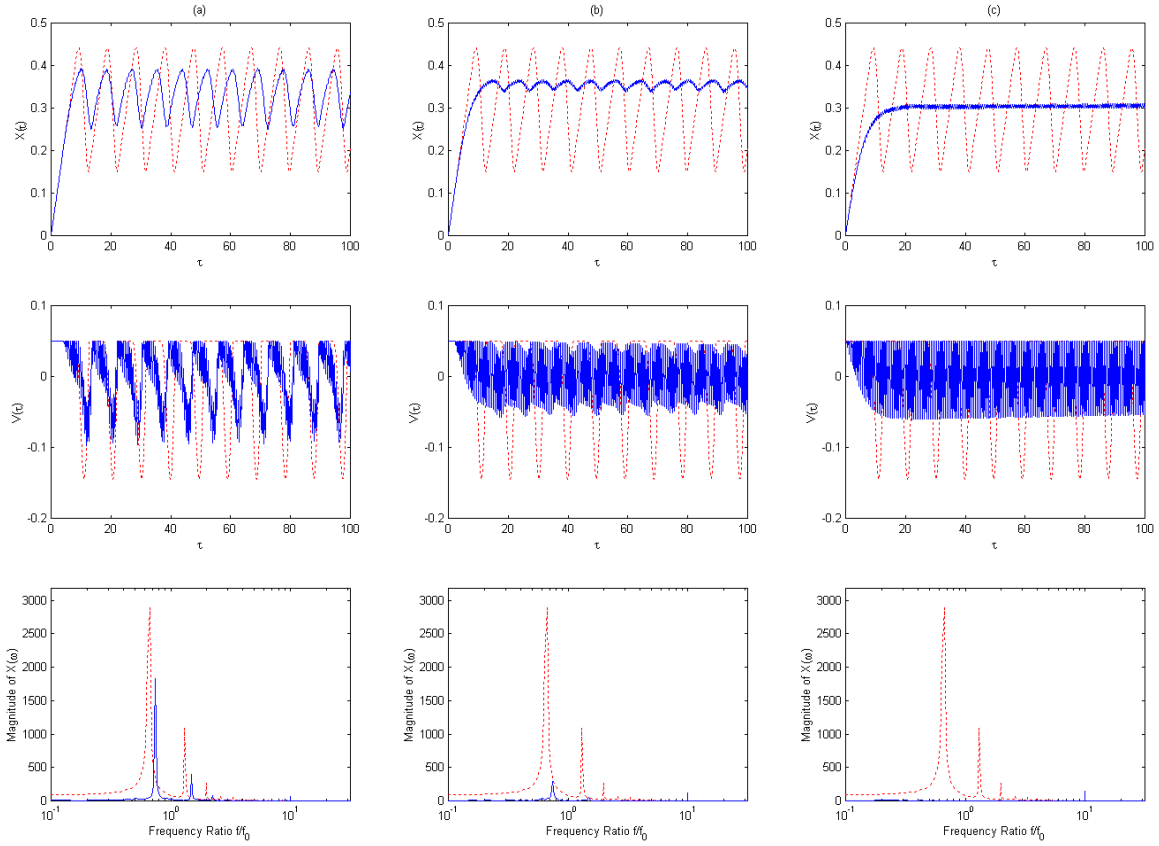

Figure 3.9: System responses with the Stribeck friction model, displacements x(τ) (top row), velocities v(τ) (middle row), and magnitude of X(ω) (bottom row) for three values of square tangential dither amplitude D_T. (…) Reference case without dither excitation; (-) Dithered system. Parameters: ω_0=1, ζ=0.005, F=1, v_0=0.05, v_m=0.2, μ_s=0.4, μ_m=0.2857, R_T=10, and (a) D_T=0.2, (b) D_T=0.3, (c) D_T=0.4.

The essential feature of using different dither waveforms is that dither achieves different level of control for a given value of dither amplitude D_T for different waveforms. Consistent with the results of the averaging technique, sinusoidal waveforms achieve a higher level of control than triangular waveforms, but a lower level of control than square waveforms, for a given dither amplitude.

Stabilizing Effect of Dither

In order to quantify the effectiveness of the dither cancellation technique, the numerical metric that expresses the relative improvement of the dithered system to the undithered system, denoted by E was developed in Chapter 2.

Figure 3.10 shows contour plots of the metric E as a function of dither amplitude and frequency ratio D_T for three different belt velocities, using the Stribeck friction model. The isoclines represent identical levels of reduction achieved by dither for pairs of dither parameters $R_T - D_T$. The numerical studies show that, for a constant frequency ratio, the performance increases (E decreases) as D_T is increased. On the other hand, for a constant dither amplitude, the performance increases as the frequency ratio is decreased. For sufficiently high dither frequency ratio, when $R_T > 5$, small reduction ratios (less than 20%) exhibit approximately linear relationships between dither amplitude and frequency ratio. Moreover the 5% reduction ratio seems to correlate very well with the threshold dither parameter obtained using the method of averaging. Note that α_T^* for a particular belt velocity v_0 will correspond to a straight line in the $R_T - D_T$ parameter space

$$D_T = \alpha_T^* \, R_T \tag{3.63}$$

The 5% isocline in the Figure 3.10 plots coincides almost exactly with the boundary predicted by (3.40). For α_T less than α_T^*, the performance gets worse as expected. Moreover, the isoclines become less straight as the performance worsens. For example, when $E = 0.5$, the contours are fairly distorted.

Recall that the averaging results require $1/R_T$ to be a small quantity. As stated above, for $R_T > 5$, there is fairly good agreement between the stability boundaries obtained from the averaging method and the 5% performance ratio from numerical integration. The lower edges of the stability boundaries in Figure 3.10, given by inequalities (3.43), (3.47) and (3.51), show that there is a linear relationship between α_T^* and v_0. In light of (3.63), this means that the slope of the 5% isocline should increase as v_0 increases. This is supported by the progression of plots in Figure 3.10.

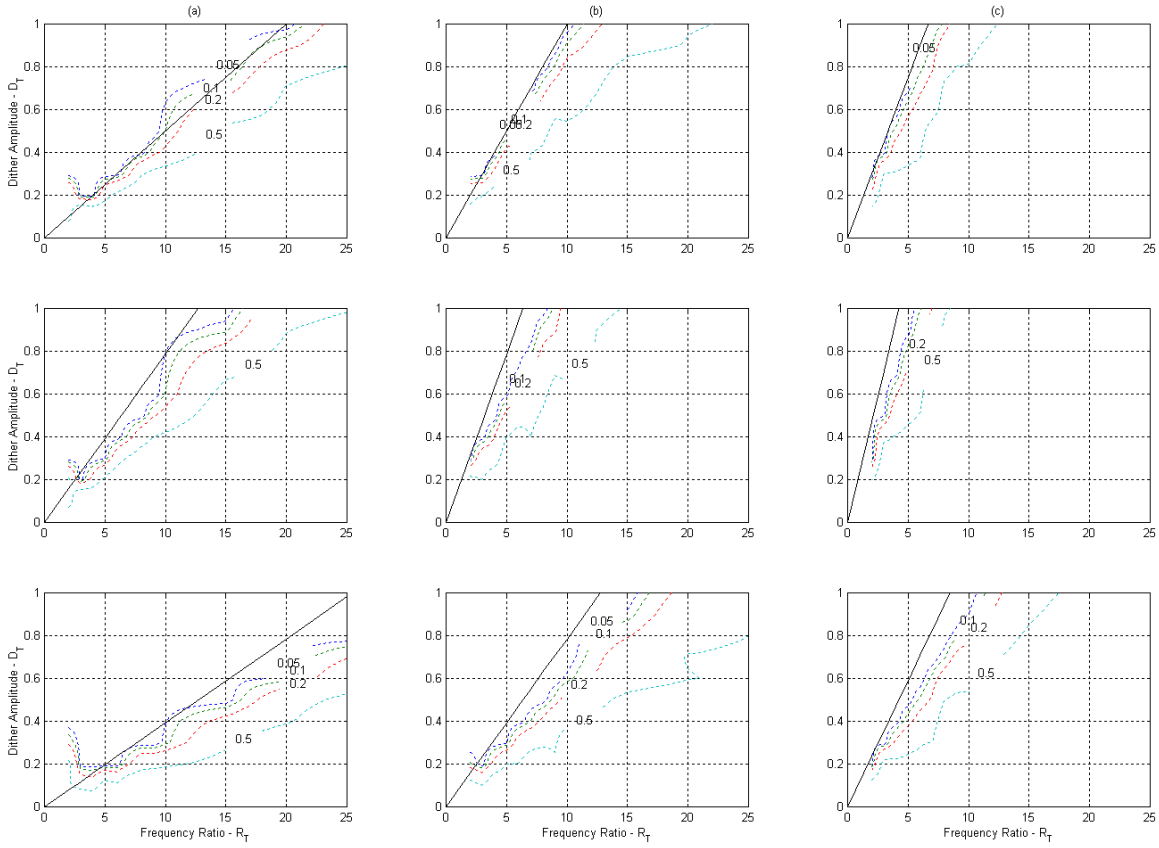

Figure 3.10: Efficiency metric using the Stribeck friction model for three waveforms: sinusoidal (top row), triangular (middle row), and square (bottom row), for three values of belt velocity v_0. (…) Efficiency metric isoclines; (-) Stability boundary using the method of averaging. Parameters: ω_0=1, ζ=0.005, F=1, v_m=0.2, μ_s=0.4, μ_m=0.2857, and (a) v_0=0.05, (b) v_0=0.1, (c) v_0=0.15.

Figure 3.11 presents contour plots of the metric E as a function of dither amplitude D_T and frequency ratio R_T for three different belt velocities, using the decreasing friction model. For the parameter values chosen and for the belt velocities shown in the 9 plots, the undithered system is unstable. For sufficiently high dither frequency ratios, when $R_T > 5$, the isoclines for small dither amplitude reduction ratios (lower than 20%) exhibit approximately linear relationships between dither amplitude and frequency ratio. The 5% reduction ratio also seems to correlate well with the stability criterion derived from the method of averaging.

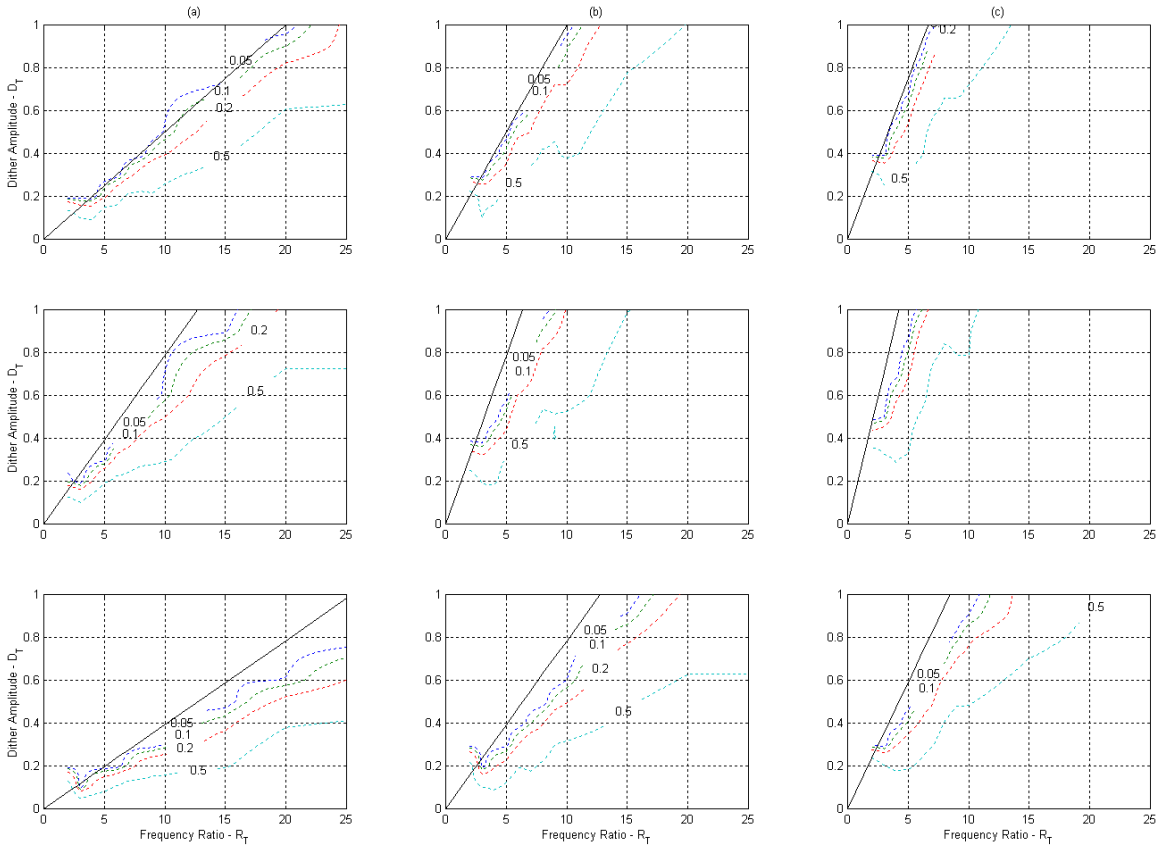

Figure 3.11: Efficiency metric using the decreasing friction model for three waveforms: sinusoidal (top row), triangular (middle row), and square (bottom row), for three values of belt velocity v_0. (…) Efficiency metric isoclines; (-) Stability boundary using the method of averaging. Parameters: ω_0=1, ζ=0.005, F=1, v_m=0.2, μ_s=0.4, μ_m=0.2857, and (a) v_0=0.05, (b) v_0=0.1, (c) v_0=0.15.

While the averaging methods are relatively easy to obtain, they cannot provide any information about the performance of the dither technique aside from the stability or instability of the system. The numerical studies reveal a strong correlation between the 5% performance ratio and the averaging method's stability bound. Away from this boundary, the numerical study reveals the conditions under which different degrees of "partial cancellations" are achieved.

Destabilizing Effect of Dither in the Case of the Decreasing Friction Law

As described in a previous section, it is possible to destabilize a stable undithered system with the decreasing friction law by injecting dither in the system. To explore this further, numerical simulations are conducted holding the belt velocity and the dither frequency ratio constant, and observing the response as D_T is increased. For a particular spring-mass-damper system, Figures 3.12 and 3.13 show 6 different values of D_T when the belt velocity is $v_0 = 1$ and $R_T = 10$, for dither with triangular and square waveforms, respectively.

The top and middle rows show the displacement and velocity response to zero initial conditions, respectively. Note that at $D_T = \alpha_T = 0$, cases (a) in Figures 3.12 and 3.13 show that the undithered system is stable. Thus the system should settle into a steady-sliding condition after the transient vibration dies out.

Using equation (3.61), the averaging method predicts that triangular dither should make the system unstable for $\alpha_T = 0.54$, i.e. $D_T = \alpha_T R_T = 5.4$. The system should return to a stable state for $\alpha_T > 1.27$, which corresponds to $D_T > 12.7$. Figure 3.12 validates this qualitative behavior. However, the system becomes unstable at a lower dither amplitude, i.e. for $D_T \geq 4$. Nevertheless there is agreement with the averaging results for the return to stability prediction, as the system is stabilized for dither amplitudes $D_T \geq 13$.

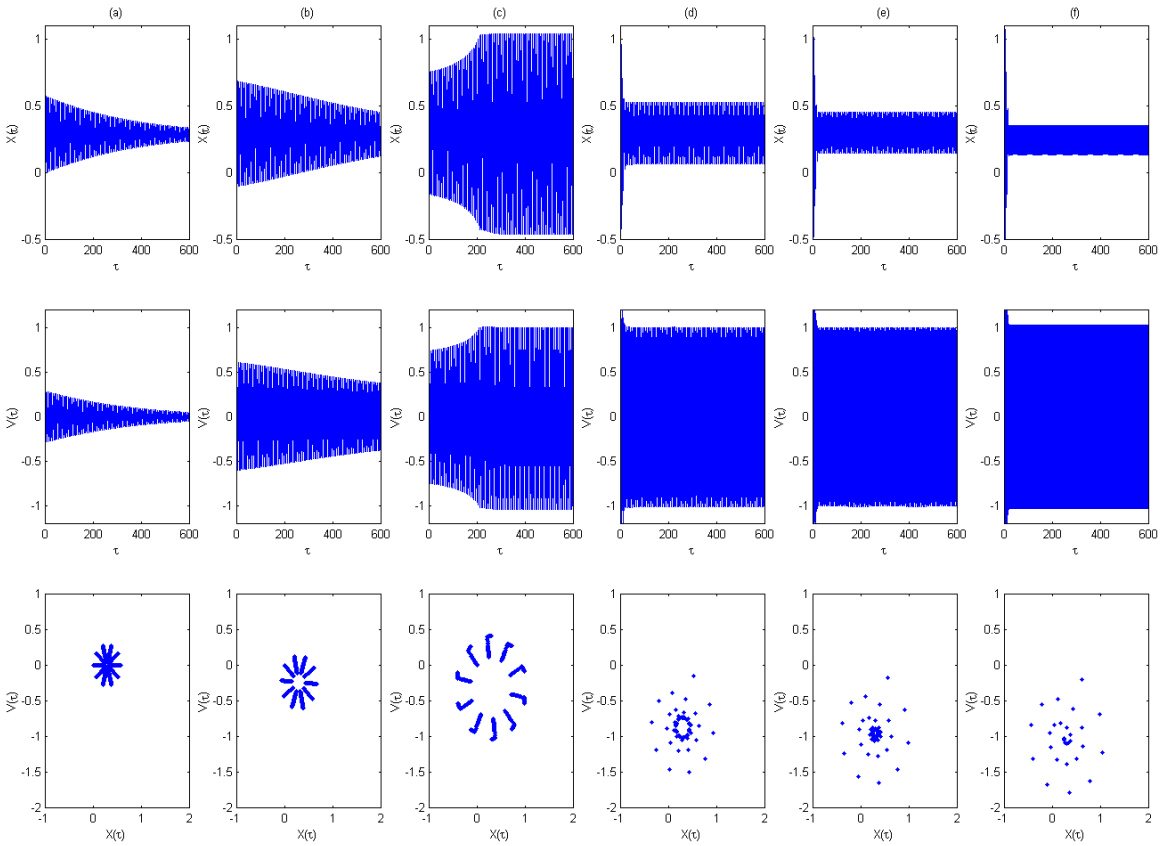

Figure 3.12: System responses with the decreasing friction model, displacements x(τ) (top row), velocities v(τ) (middle row), and Poincaré maps (bottom row) for six values of tangential dither amplitude D_T with triangular waveforms. Parameters: ω_0=1, ζ=0.005, F=1, v_0=1.0, v_m=0.2, μ_s=0.4, μ_m=0.2857, R_T=10, and (a) D_T=0, (b) D_T=3, (c) D_T=4, (d) D_T=11, (e) D_T=12, (f) D_T=13.

The bottom row of plots in Figure 3.12 shows the Poincaré plots as D_T changes. The Poincaré section is chosen to coincide with the time instants: $R_T\tau_n = 2n\pi$ for $n = 0,\ 1,\ 2,\ \ldots$ During "stable" response, the Poincaré plot spirals down to a period-1 response. When the dither signal destabilizes the system, the Poincaré plot shows a closed-orbit, closely resembling a period-10 response. It appears that the dither signal is successful in smoothing the nonlinearity, so that the low-frequency response is at or near ω_0, even though the limit-cycle oscillation occurs typically at a lower frequency. In the

case of an unstable response, this sustained low-frequency response component is joined to a second component at the dither frequency.

For the same system studied in Figure 3.12, but for square dither waveforms, Figure 3.13 shows a progression of responses for a belt velocity of $v_0 = 1.0$ and a dither frequency ratio of $R_T = 10$. Using equation (3.62), the averaging method predicts that square dither should make the system unstable for $3.3 \le D_T \le 6.3$. The numerical study shows the same qualitative trend, but the instability occurs at a much smaller dither amplitude, $D_T = 2.5$. Again, the Poincaré plots show that the unstable response is period-10 at times; in some cases, the two dominant frequencies are not exactly commensurate, but show an approximate 10 to 1 ratio. In agreement with the averaging result, the system is stable again for dither amplitudes $D_T \ge 6.5$.

As mentioned in Chapter 2, it is very difficult to pinpoint the exact value of D_T (or α_T) at which the stability of the system switches. Therefore, an exhaustive numerical study was not conducted on the potential destabilizing effects of dither. It is clear from the numerical simulations that it is indeed possible to destabilize a system by injecting sinusoidal dither, as shown in Chapter 2, but it is also true in the case of triangular and square dither signals. However, just as the square dither was more effective in canceling self-excited oscillations, it is unfortunately more effective in its destabilizing tendencies. For example, at $v_0 = 1.0$, the triangular dither destabilizes the system at $D_T \ge 4$; the sinusoidal dither destabilizes the system at $D_T \ge 3$; and the square dither destabilizes the system at $D_T \ge 2.5$.

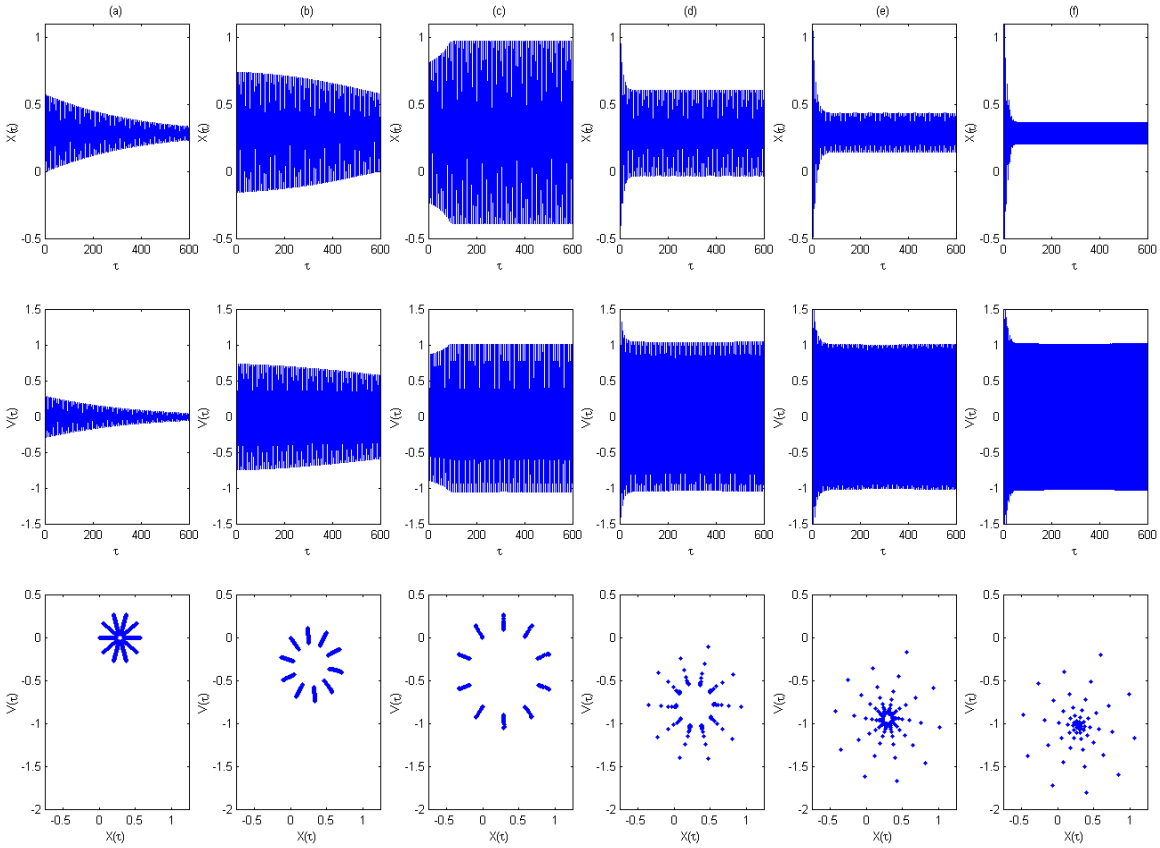

Figure 3.13: System responses with the decreasing friction model, displacements x(τ) (top row), velocities v(τ) (middle row), and Poincaré maps (bottom row) for six values of tangential dither amplitude D_T with square waveforms. Parameters: ω_0=1, ζ=0.005, F=1, v_0=1.0, v_m=0.2, μ_s=0.4, μ_m=0.2857, R_T=10, and (a) D_T=0, (b) D_T=2, (c) D_T=2.5, (d) D_T=5, (e) D_T=6, (f) D_T=6.5.

CONCLUSION

In Chapter 2, it was found that self-excited oscillations in the system having the Stribeck friction or the decreasing friction model could be stabilized by applying sinusoidal tangential dither of sufficient amplitude. This result is extended to tangential dither signals with triangular and square waveforms.

The effect of various waveforms on stability has been quantified and can be predicted using the averaging technique. The averaging technique shows that sinusoidal

waveforms requires a higher dither force than square waveforms, but a lower force than triangular waveforms in order to achieve stability of an undithered unstable system, at any belt velocity.

Amplitude-frequency combinations of dither with triangular and square waveforms that cause the steady-state dithered response to decrease to 5% of the undithered response show a very repeatable correlation with the stability boundary predicted by the averaging technique, as found in Chapter 2 for sinusoidal dither signals. Numerical simulations show that, for a given dither force amplitude, triangular waveforms achieve a lower level of control than sinusoidal waveforms, and square waveforms achieve a higher level of control than sinusoidal waveforms.

As found in Chapter 2, the system with the decreasing friction model, unlike with the Stribeck friction model, can also be destabilized by dither. Both the averaging technique and numerical simulations show that an undithered stable system can be destabilized by applying dither with triangular and square waveforms of intermediate strength, as found in Chapter 2 for sinusoidal dither signals. For a given belt velocity, the range of dither amplitudes that destabilizes the system is broad and within high amplitude levels for the triangular waveforms, and is narrow and within low amplitude levels for the square waveforms. The range of destabilizing dither amplitudes for sinusoidal waveforms lies between that of the triangular and the square waveforms.

CHAPTER 4

SDOF WITH NORMAL DITHER

This chapter explores the effect of normal dither excitation on system stability. Although there are many similarities between normal and tangential dither, the normal dither case is much more difficult to analyze. Furthermore, it is shown that normal dither is not as effective as tangential dither.

In this Chapter, the equations of motion for the vibration of a mass on a moving belt problem described in Chapter 2 are restated. A numerical procedure is employed to study the stability of the system with normal dither.

MODEL DEVELOPMENT

In this section, the governing equations for a single-degree-of-freedom (SDOF) frictional system are restated for convenience. The section also restates the two friction models, used in Chapter 2, that will be employed in this study.

Equation of Motion

The SDOF model consists of a mass pressed into contact with a rigid moving surface, restrained by a linear spring and a viscous damper, as shown in Figure 4.1. The normal force, i.e. the force normal to the friction interface, consists of a constant load N, which models the applied braking force, plus an oscillatory force representing normal dither. The figure shows a normal dither force of amplitude A_N and frequency ω_N, which is typically very large compared to the natural frequency and/or the squeal

frequency of the system. Initially, only sinusoidal dither is considered. The belt is assumed to move at the constant speed V_0.

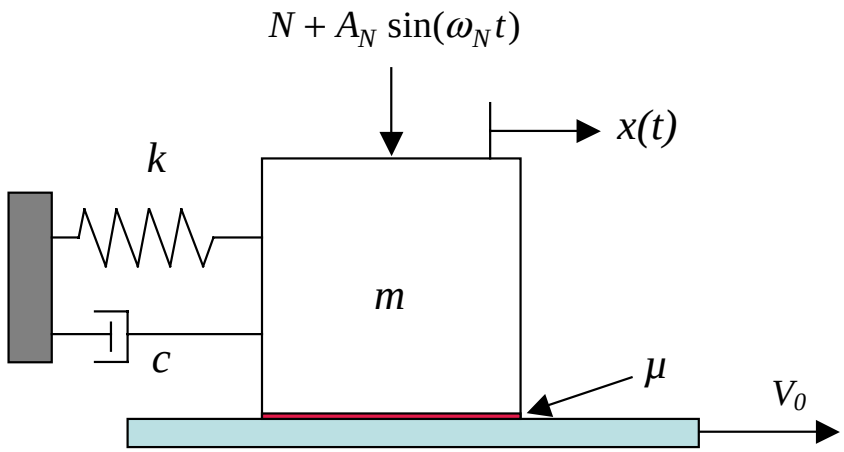

Figure 4.1: SDOF model

The non-dimensional equation of motion of the SDOF system is given by

$$\frac{d^2x}{d\tau^2} + 2\zeta\frac{dx}{d\tau} + x = f\left(\frac{dx}{d\tau}\right) \tag{4.1}$$

where $\omega_0^2 = k/m$ is the system's natural frequency, $\tau = \omega_0 t$ is non-dimensional time, $\zeta = c/2\omega_0 m$ is the damping ratio. Note that x has unit of length.

The scaled friction force f is defined as

$$f\left(\frac{dx}{d\tau}\right) = \mu(v_r) \times (F + D_N \sin(R_N \tau)) \tag{4.2}$$

where $F = N/k$ is a scaled normal force, $v_r = v_0 - dx/d\tau$ is the relative velocity or "slip velocity" of the mass, $v_0 = V_0/\omega_0$ is a scaled belt velocity, and the normal dither frequency and amplitude ratios are denoted by $R_N = \omega_N/\omega_0$ and $D_N = A_N/k$,

respectively. Note that the normal dither force D_N cannot be higher than F, as normal dither cannot create a negative friction force. Two friction models are considered in this study.

Dynamics of Stick-Slip Transitions

While equations (4.1) and (4.2) govern the dynamics of the mass during slip, a more-convenient form are used during sticking episodes. Since the belt moves with constant velocity during sticking, the sticking dynamics can be written as

$$\frac{d^2x}{d\tau^2} = 0 \quad \text{and} \quad \frac{dx}{d\tau} = v_0 \tag{4.3}$$

When the slip velocity is zero, the friction coefficient is undefined, thus it becomes an unknown. The resulting static friction force, called the sticktion force, needs to be determined. The unknown sticktion force, denoted by f_s, prevents slip from taking place between the mass and the belt, and can be found by substituting (4.3) into (4.1)

$$f_s = 2\zeta v_0 + x(\tau) \tag{4.4}$$

When the maximum allowable sticktion force is exceeded, the friction is not able to sustain the sticking phase, and therefore the system transitions back to a slipping phase. During sticking, the mass will begin to slip again if

$$|f_s| \geq \mu_s \times |F + D_N \sin(R_N \tau)| \tag{4.5}$$

where μ_s is the magnitude of the friction coefficient at $v_r = 0$. During slipping, the mass will stick again when

$$\frac{dx}{d\tau} = v_0 \quad \text{and} \quad |f_s| \le \mu_s \times |F + D_N \sin(R_N \tau)| \tag{4.6}$$

Thus conditions (4.5) and (4.6) are used to alternate between sticking dynamics and slip dynamics.

Friction Models

The two friction models that are used for this study are given by equations (2.7) and (2.8), and are restated in this section for convenience.

Stribeck Friction Law

$$\mu(v_r) = \begin{cases} \mu_s sign(v_r) - \frac{3}{2}(\mu_s - \mu_m)\left(\frac{v_r}{v_m} - \frac{1}{3}\left(\frac{v_r}{v_m}\right)^3\right) & for\ v_r \neq 0 \\ \tilde{\mu}_s & for\ v_r = 0 \end{cases} \tag{4.7}$$

where μ_s is the static coefficient of friction that applies when $v_r = 0$, and μ_m is the minimum coefficient of friction, which occurs at slip velocity v_m. As discussed previously, if the interface sticks and $v_r = 0$ for a finite time, the friction force f_s must be determined by equilibrium considerations; this is indicated in equation (4.7) by $\tilde{\mu}_s$, which can be thought of an unknown scaling factor between f_s and the normal load. Note that the friction coefficient $\mu(v_r)$ can be positive or negative, depending on the instantaneous slip velocity v_r.

Decreasing Friction Law

A second friction law that is considered in this study is characterized by a friction coefficient that smoothly decreases with slip velocity, given by

$$\mu(v_r) = \begin{cases} \left[\mu_m + (\mu_s - \mu_m)\exp\left(-\frac{|v_r|}{v_m}\right)\right] sign(v_r) & for\ v_r \neq 0 \\ \tilde{\mu}_s & for\ v_r = 0 \end{cases} \tag{4.8}$$

As with the Stribeck model, μ_s is the static friction coefficient, and μ_m can be interpreted as the dynamic friction coefficient. Figure 4.2 depicts the described friction models, for the case of $\mu_s = 0.4$ and $\mu_m = 0.2587$.

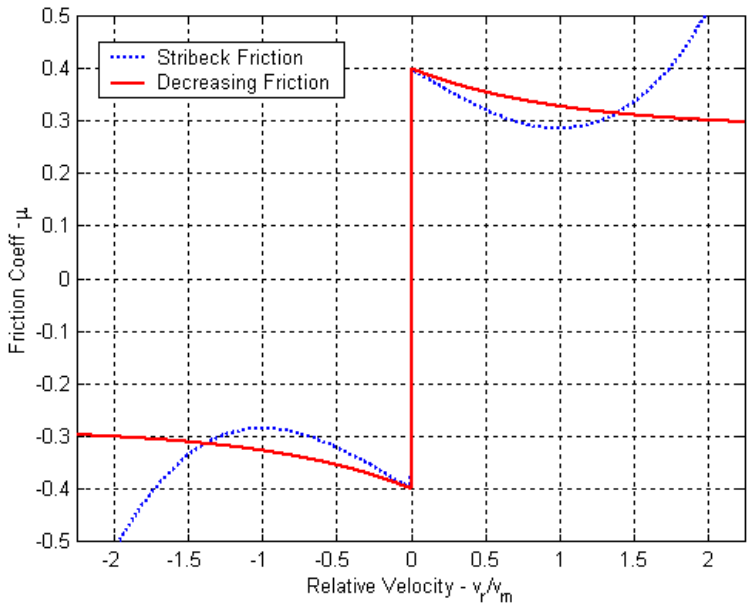

Figure 4.2: Comparison of Stribeck and decreasing friction laws. Parameters: μ_s=0.4, μ_m=0.2857.

Typical System Response

Without dither, the SDOF system described above is well known to be prone to sustained stick-slip oscillations, as discussed in Chapter 2. With dither, the system exhibits responses very similar to the one shown in Chapter 2. The essential difference is that normal dither cannot achieve the same level of control as tangential because the normal dither amplitude D_N is limited to a maximum value of F. The other major difference is that the modulated tangential force is dependent on the stick/slip state of the interface.

Figures 4.3 and 4.4 show typical numerical simulation results using the Stribeck friction model with $R_N = 10$ and decreasing friction model with $R_N = 7$, respectively. The dashed lines denote the results for the system with no dither and the solid lines show the results for the dithered system for three different values of normal dither amplitudes D_N.

Figure 4.3 exemplifies the inability of normal dither with frequency ratio $R_N = 10$ to suppress self-sustained oscillations in a system with Stribeck friction. The dither amplitude is increased from $D_N = 0.3$ in case (a), to $D_N = 0.6$ in case (b), and to $D_N = 0.9$ in case (c), but none of these cases leads to complete suppression of the self-sustained oscillations. The best case is case (c) where normal dither of amplitude $D_N = 0.9$ manages to cancel approximately 50% of the stick-slip oscillations.

Figure 4.4 shows a case where normal dither is able to cancel self-sustained oscillations in a system with the decreasing friction law. For small amplitudes of dither (cases (a) and (b) in Figure 4.4), the responses exhibit partial control, i.e. the magnitude

of the signal's spectrum in the vicinity of the self-excited oscillation has been reduced, but yet not completely eliminated. When the normal dither force amplitude is increased from $D_N = 0.6$ to $D_N = 0.9$ with a frequency ratio $R_N = 7$, as depicted in case (c) in Figure 4.4, the system is fully controlled by dither, i.e. the self-excited free-response oscillations are replaced with a forced response at the frequency of the dither input.

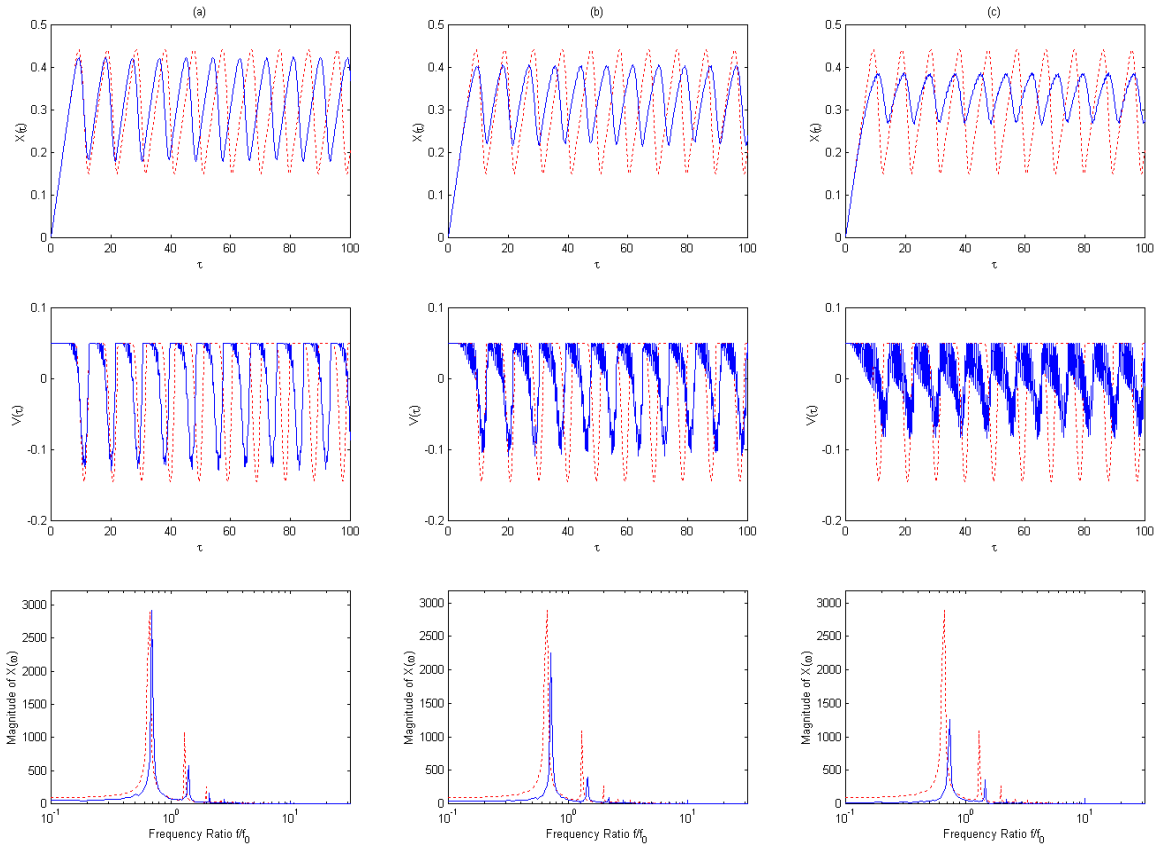

Figure 4.3: System responses with the Stribeck friction model, displacements $x(\tau)$ (top row), velocities $v(\tau)$ (middle row), and magnitude of $X(\omega)$ (bottom row) for three values of normal dither amplitude D_N. (…) Reference case without dither excitation; (-) Dithered system. Parameters: ω_0=1, ζ=0.005, F=1, v_0=0.05, v_m=0.2, μ_s=0.4, μ_m=0.2857, R_N=10, and (a) D_N=0.3, (b) D_N=0.6, (c) D_N=0.9.

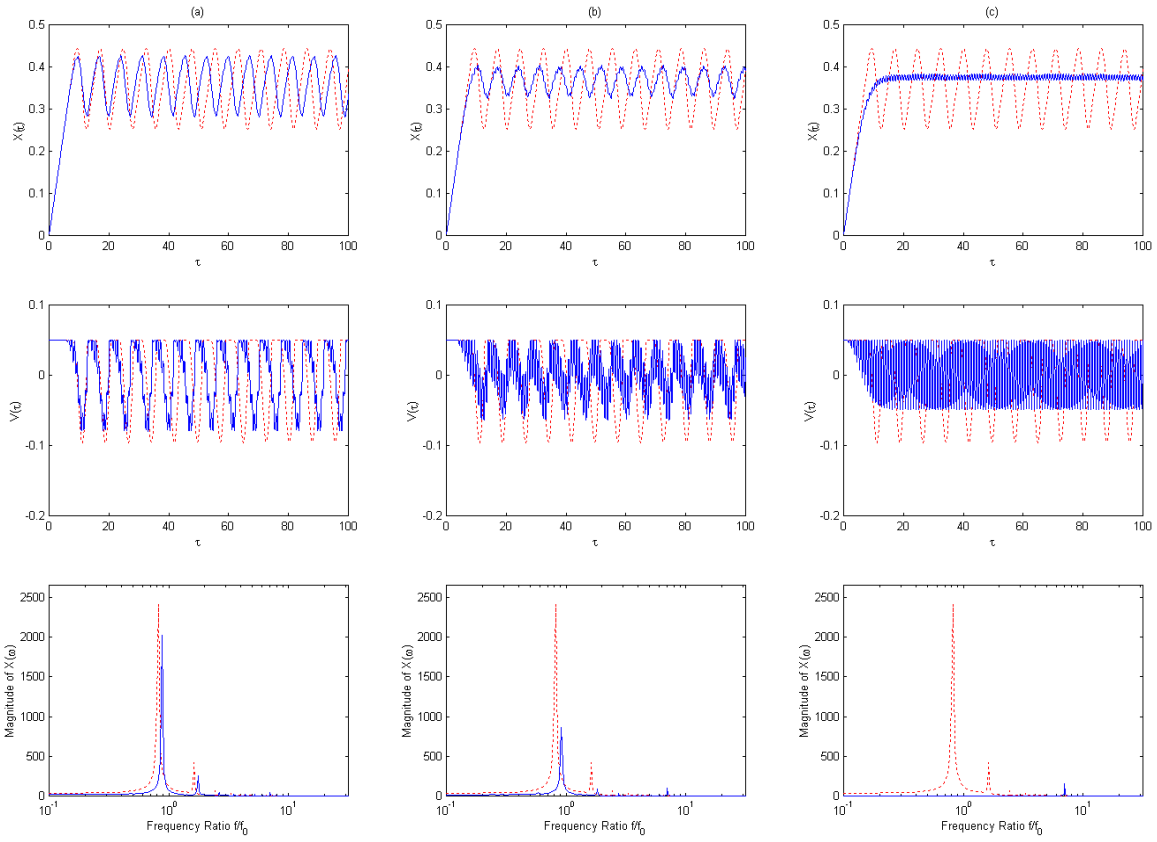

Figure 4.4: System responses with the decreasing friction model, displacements $x(\tau)$ (top row), velocities $v(\tau)$ (middle row), and magnitude of $X(\omega)$ (bottom row) for three values of normal dither amplitude D_N. (…) Reference case without dither excitation; (-) Dithered system. Parameters: ω_0=1, ζ=0.005, F=1, v_0=0.05, v_m=0.2, μ_s=0.4, μ_m=0.2857, R_N=7, and (a) D_N=0.3, (b) D_N=0.6, (c) D_N=0.9.

METHOD OF AVERAGING

As in Chapter 2, an approximate solution is sought using the method of averaging. Then, an effective friction characteristic is obtained from which stability can be predicted.

Effective Friction Characteristic

For convenience, the equation of motion can be restated as

$$\frac{d^2x}{d\tau^2}+2\zeta\frac{dx}{d\tau}+x-\mu\left(v_0-\frac{dx}{d\tau}\right)\times\left(F+D_N\sin(R_N\tau)\right)=0 \tag{4.9}$$

As before, the solution is decomposed into a "fast" component, φ, and a "slow" component, Z, and written as

$$x(\tau)=Z(\tau)+\frac{1}{R_N}\varphi(\tau,R_N\tau) \tag{4.10}$$

Note that, for $R_N >> 1$, the fast component is $O\left(R_N^{-1}\right)$. Also note that φ depends on two time scales. The following shorthand notation for the derivatives is used:

$$\dot{x}=\frac{\partial x}{\partial\tau} \qquad \text{and} \qquad x'=\frac{\partial x}{\partial\left(R_N\tau\right)} \tag{4.11}$$

Therefore, the derivatives are given by:

$$\begin{aligned}\frac{dx}{d\tau}&=\dot{Z}+R_N^{-1}\dot{\varphi}+\varphi'\\ \frac{d^2x}{d\tau^2}&=\ddot{Z}+R_N^{-1}\ddot{\varphi}+2\dot{\varphi}'+R_N\varphi''\end{aligned} \tag{4.12}$$

Substitution of (4.12) in to (4.9), and grouping the terms according to orders of R_N yields

$$\begin{aligned}\left\{\ddot{Z}+2\zeta\dot{Z}+Z+2\zeta\varphi'+2\dot{\varphi}'-\mu\left(v_0-\left(\dot{Z}+R_N^{-1}\dot{\varphi}+\varphi'\right)\right)\times\left(F+D_N\sin(R_N\tau)\right)\right\}\\ +R_N\left(\varphi''\right)+R_N^{-1}\left(\ddot{\varphi}+2\zeta\dot{\varphi}+\varphi\right)=0\end{aligned} \tag{4.13}$$

Note that, unlike the tangential dither case, the $O\left(R_N\right)$ terms do not yield a solution that is consistent with the observed behavior of Figures 4.3 and 4.4. In particular, if D_N and F are $O(1)$ then the $O\left(R_N\right)$ term is simply $\varphi''=0$, whose solution is not oscillatory. In fact if φ is restricted to be zero on average over one period, then $\varphi=0$. In order to

proceed with this analysis, the normal dither force D_N is temporarily allowed to be higher than the normal load F. Although this violates one of the assumptions, it facilitates a solution. The reasonableness of this approach and the predictions from this analysis are further discussed below.

If the dither amplitude is assumed to be of order R_N, then D_N can be expressed as

$$D_N = \alpha_N R_N \quad with\ \alpha_N = O(1) \tag{4.14}$$

Equating terms of order $O(R_N)$ in equation (4.13), and noting that $R_N^{-1}\dot{\varphi} << 1$, yields the relation

$$\varphi'' - \alpha_N \mu\left(\left(v_0 - \dot{Z}\right) - \varphi'\right)\sin(R_N \tau) = O\left(R_N^{-1}\right) \tag{4.15}$$

Equation (4.15) cannot be solved exactly. If $\alpha_N = \varepsilon << 1$, then $\varphi'' << 1$ and thus φ' will not change very much. Consequently, if φ' is initially small, it will remain small. Therefore an approximate solution for (4.15) can be obtained when $\varphi' = O(\varepsilon)$. Assume a solution of the form

$$\varphi' = \varepsilon\varphi_1' + \varepsilon^2\varphi_2' + O\left(\varepsilon^3\right) \tag{4.16}$$

Assuming that $\left(v_0 - \dot{Z}\right) \neq 0$, then a Taylor series can be used to approximate the nonlinearity in (4.15) as follows

$$\mu\left(\left(v_0 - \dot{Z}\right) - \varphi'\right) \simeq \mu\left(v_0 - \dot{Z}\right) - \varphi'\mu'\left(v_0 - \dot{Z}\right) + O\left(\varepsilon^2\right) \tag{4.17}$$

Substituting (4.16) and (4.17) into (4.15) yields

$$\left(\varepsilon\varphi_1'' + \varepsilon^2\varphi_2''\right) - \alpha_N\left(\mu\left(v_0 - \dot{Z}\right) - \left(\varepsilon\varphi_1' + \varepsilon^2\varphi_2'\right)\mu'\left(v_0 - \dot{Z}\right)\right)\sin(R_N\tau) = 0 \qquad (4.18)$$

Equating terms of order $O(\varepsilon)$ in equation (4.18)

$$\varepsilon\varphi_1'' - \alpha_N\mu\left(v_0 - \dot{Z}\right)\sin(R_N\tau) = 0 \qquad (4.19)$$

Thus $\varepsilon\varphi_1'$ is given by

$$\varepsilon\varphi_1' = -\alpha_N\mu\left(v_0 - \dot{Z}\right)\cos(R_N\tau) \qquad (4.20)$$

Equating terms of order $O(\varepsilon^2)$ in equation (4.18) and using (4.20) yields

$$\varepsilon^2\varphi_2'' - \alpha_N^2\mu\left(v_0 - \dot{Z}\right)\mu'\left(v_0 - \dot{Z}\right)\cos(R_N\tau)\sin(R_N\tau) = 0 \qquad (4.21)$$

Thus $\varepsilon^2\varphi_2'$ is given by

$$\varepsilon^2\varphi_2' = -\frac{\alpha_N^2}{4}\mu\left(v_0 - \dot{Z}\right)\mu'\left(v_0 - \dot{Z}\right)\cos(2R_N\tau) \qquad (4.22)$$

Therefore an approximate solution for (4.15) can be written as

$$\varphi' = -\alpha_N\mu\left(v_0 - \dot{Z}\right)\left\{\cos(R_N\tau) + \frac{\alpha_N}{4}\mu'\left(v_0 - \dot{Z}\right)\cos(2R_N\tau)\right\} + O\left(\alpha_N^3\right) \qquad (4.23)$$

From the terms of $O(1)$ in equation (4.13), the next equation to be solved is

$$\ddot{Z} + 2\zeta\dot{Z} + Z = \mu\left(v_0 - \dot{Z} - \varphi'\right)F - 2\zeta\varphi' - 2\dot{\varphi}' \qquad (4.24)$$

The averaging technique can be used to solve equation (4.24). The fast-time-average operator is introduced, which time-averages over one period of the fast excitation, considering the slow time τ to be fixed. As before,

$$\left\langle f\left(\tau, R_N\tau\right)\right\rangle \equiv \frac{1}{2\pi}\int_0^{2\pi} f\left(\tau, R_N\tau\right) d\left(R_N\tau\right) \tag{4.25}$$

The fast solution is assumed to be periodic in the fast time $R_N\tau$, such that the fast time average of $\varphi\left(\tau, R_N\tau\right)$ is zero

$$\left\langle \varphi\left(\tau, R_N\tau\right)\right\rangle = \frac{1}{2\pi}\int_0^{2\pi} \varphi\left(\tau, R_N\tau\right) d\left(R_N\tau\right) = 0 \tag{4.26}$$

Applying the averaging operator to equation (4.24) produces the governing equation for the slow dynamics

$$\ddot{Z} + 2\zeta\dot{Z} + Z = \bar{\mu}\left(v_0 - \dot{Z}\right)F \tag{4.27}$$

The effective friction characteristic $\bar{\mu}$ can be thought of as a "smoothed" version of the discontinuous friction law. Using $v_r = v_0 - \dot{Z}$ to denote the slow component of the slip velocity, $\bar{\mu}$ can be expressed as

$$\bar{\mu}\left(v_r\right) = \left\langle \mu\left(v_r - \varphi'\left(\tau, R_N\tau, v_r\right)\right)\right\rangle \tag{4.28}$$

Note that this analysis will be physically meaningful only if the normal dither force D_N is lower than the normal load F. Thus the equation (4.28) is taken to hold for

$$\alpha_N < \frac{F}{R_N} \tag{4.29}$$

It is also important to realize that equation (4.28) has been derived in the limit of R_N going to infinity, which is inconsistent with (4.14) where $\alpha_N = O(1)$. Still, as

demonstrated below, the results of this section are shown to be quite useful, both as means of interpreting numerical results and as a predictive tool.

Numerical Procedure

Equation (4.15) is highly nonlinear and cannot be solved exactly. Instead, equation (4.1) is time-simulated using the procedure previously described. From the computed response, a numerical procedure can be employed to obtain an approximation of the effective friction characteristic. The effective friction coefficient is computed by time-averaging, in the sense of (4.25), the ratio of instantaneous tangential force over instantaneous normal force over one period of the fast excitation.

At a particular time instant τ_i, the effective friction coefficient can be defined as

$$\bar{\mu}_i \equiv \left\langle \left. \frac{f\left(x, dx/d\tau, \tau\right)}{F + D_N \sin\left(R_N \tau\right)} \right|_{\tau=\tau_i} \right\rangle = \frac{R_N}{2\pi} \int_{\tau_i - \pi/R_N}^{\tau_i + \pi/R_N} \frac{f\left(x, dx/d\tau, \tau\right)}{F + D_N \sin\left(R_N \tau\right)} \, d\tau \tag{4.30}$$

where $f\left(x, dx/d\tau, \tau\right)$ is the friction force, regardless of the system stick/slip state.

In a similar fashion, the average slip velocity near $\tau = \tau_i$ can be obtained by time-averaging the instantaneous slip velocity over one period of the fast excitation.

$$\bar{v}_{r,i} \equiv \left\langle v_r\left(\tau\right)\big|_{\tau=\tau_i} \right\rangle = \frac{R_N}{2\pi} \int_{\tau_i - \pi/R_N}^{\tau_i + \pi/R_N} \left(v_0 - \frac{dx}{d\tau} \right) d\tau \tag{4.31}$$

Thus the numerical effective friction characteristic can be visualized by plotting $\bar{\mu}_i$ versus $\bar{v}_{r,i}$ at each time τ_i in a time simulation.

The numerical effective friction characteristics can be plotted along with the result from the method of averaging and with the friction law itself. Figures 4.5 and 4.6

show such a plot for four different values of $\alpha_N = D_N / R_N$, for the Stribeck friction model and for the decreasing friction model, respectively. Note that the friction characteristic in Figures 4.5 and 4.6 has been calculated over one period of the fundamental frequency when the self-excited oscillations have been canceled and the system is in its steady state. Also for the sake of clarity, the graphs show only those results for times $\tau = \tau_i$ for which sticking did not occur over the interval $[\tau_i - \pi/R_N ,\ \tau_i + \pi/R_N]$.

A comparison of equations (4.23) and (2.16) shows that there is a strong similarity between the fast solution of the normally and tangentially dithered friction systems. In particular, if terms of order α_N^2 are dropped and (4.23) is integrated, the fast response is found to be $\varphi = -\alpha_N \mu \left(v_0 - \dot{Z}\right)\sin(R_N \tau)$, which corresponds the fast solution found in the tangential dither case, i.e. equation (2.16) where $\alpha_T = \alpha_N \mu \left(v_0 - \dot{Z}\right)$.

The approximate solution derived from the method of averaging differs from the numerical computation in the convexity of the curve in low slip velocities region. However, there is strong agreement between the effective friction laws in the negative-sloping region. In other words, although effective friction characteristics obtained numerically and from the method of averaging differ in the low slip velocities region, they strongly agree in the prediction of where the friction coefficient slope changes sign. Therefore, the effective friction law from the method of averaging accurately predicts the change in stability in the limit of small dither amplitude, i.e. α_N is order $O(\varepsilon)$. Recall that the assumption of small α_N was made to approximate the solution in the method of averaging. Therefore, the location of the friction coefficient slope change in sign using

the method of averaging gets closer and closer to the numerical prediction as D_N gets smaller, or as R_N gets larger. This may be seen in Figures 4.5 and 4.6 by the fact that the stability predictions (slope change) by method of averaging are more accurate in cases (a) than (d).

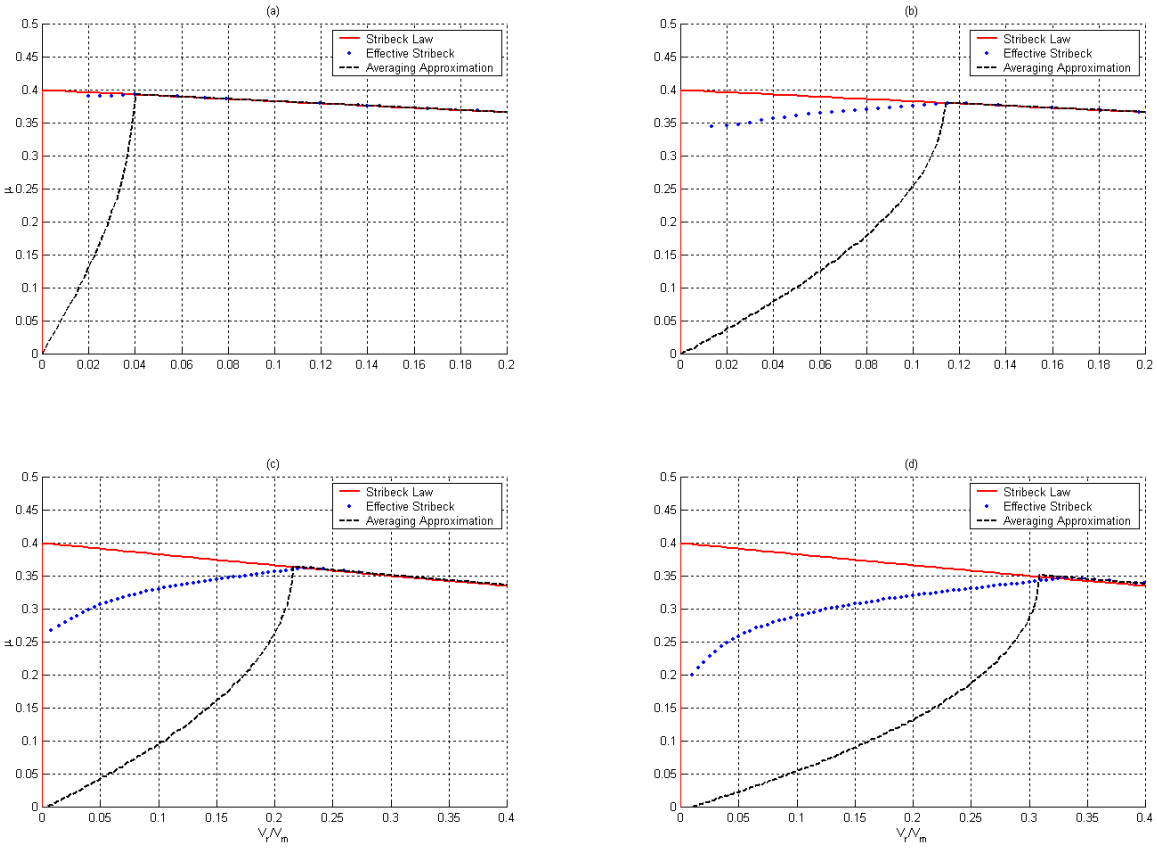

Figure 4.5: Effective Stribeck friction characteristic (•), Stribeck friction law (▬), and averaging approximation (…). Parameters: ω_0=1, ζ=0.005, F=1, μ_s=0.4, μ_m=0.2857, v_m=0.2, F=1, R_N=5, and (a) D_N=0.1, (b) D_N=0.3, (c) D_N=0.6, (d) D_N=0.9.

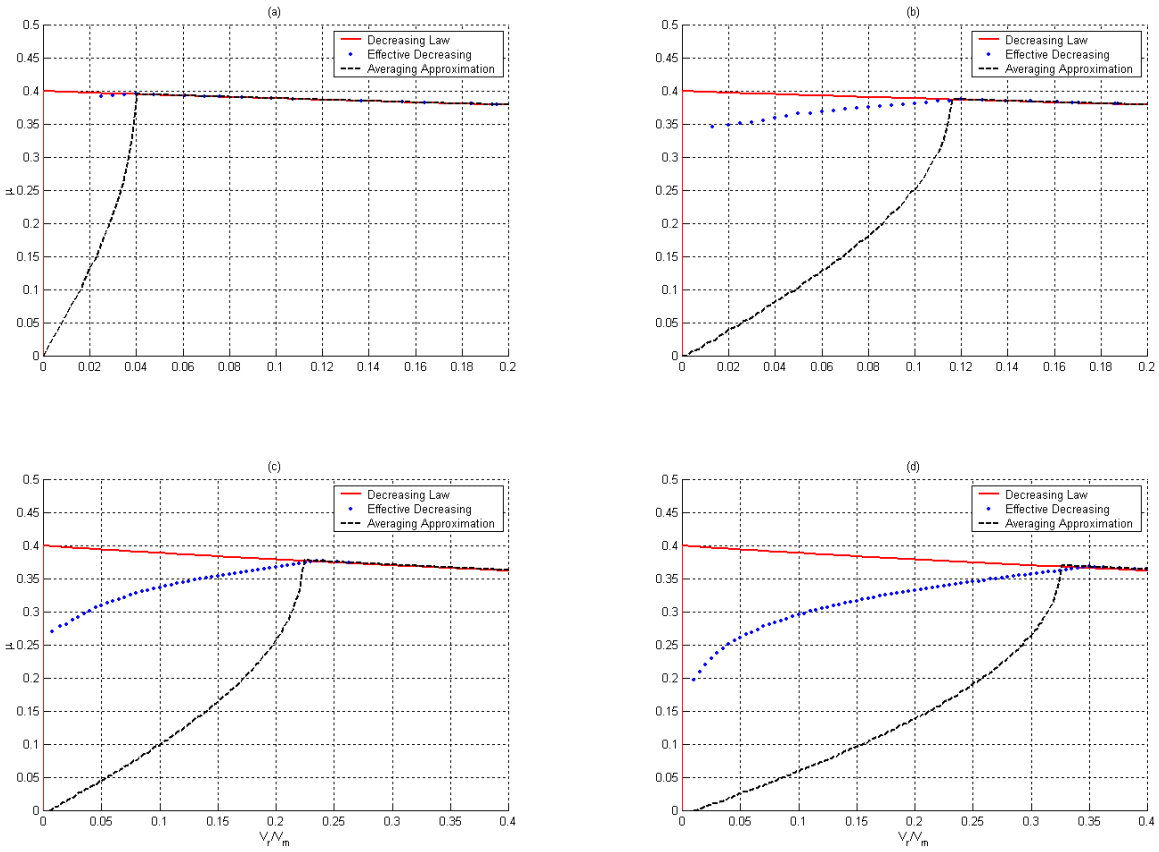

Figure 4.6: Effective decreasing friction characteristic (•), decreasing friction law (▬), and averaging approximation (…). Parameters: ω_0=1, ζ=0.005, F=1, μ_s=0.4, μ_m=0.2857, v_m=0.2, F=1, R_N=5, and (a) D_N=0.1, (b) D_N=0.3, (c) D_N=0.6, (d) D_N=0.9.

Stability Boundaries

The stability criterion is exactly the same as that used in Chapter 2:

$$2\zeta + \bar{\mu}'(v_0)F < 0 \tag{4.32}$$

In this Chapter, the derivative of the effective friction characteristic must be approximated numerically in order to use (4.32).

Stribeck Friction Law

The stability boundary for the Stribeck friction law was obtained analytically in Chapter 3, given by equations (3.51), (3.55) and (3.59) for sinusoidal, triangular and square waveforms, respectively. Based on the results of a previous section, this criterion can be extended to a system with normal dither, by replacing α_T in equations (3.51), (3.55) and (3.59) by $\mu(v_0)\alpha_N$. Note that this extension is valid in the limit of small dither amplitudes, where the $\cos(2R_N\tau)$ term in (4.23) can safely be neglected.

Replacing α_T in (3.51) with $\mu(v_0)\alpha_N$, the system with sinusoidal normal dither will be unstable if

$$\mu(v_0)\alpha_N \le v_0 \le v_m\sqrt{1-\frac{1}{2}\left(\frac{\mu(v_0)\alpha_N}{v_m}\right)^2-\frac{4v_m\zeta}{3F(\mu_s-\mu_m)}} \tag{4.33}$$

In other words, the system with normal dither with sinusoidal waveforms will be stable at any belt velocity if $\alpha_N \ge \alpha_N^L$, where

$$\alpha_N^L = \frac{v_m}{\mu(v_0)}\sqrt{\frac{2}{3}}\sqrt{1-\frac{4v_m\zeta}{3F(\mu_s-\mu_m)}} \tag{4.34}$$

The case of tangential dither with triangular waveforms, given by equation (3.55), can be adapted to normal dither. It follows that the system will be unstable if

$$\frac{\pi}{4}\mu(v_0)\alpha_N \le v_0 \le v_m\sqrt{1-\frac{\pi^2}{48}\left(\frac{\mu(v_0)\alpha_N}{v_m}\right)^2-\frac{4v_m\zeta}{3F(\mu_s-\mu_m)}} \tag{4.35}$$

In other words, the system with normal dither with triangular waveforms will be stable at any belt velocity if $\alpha_N \ge \alpha_N^L$, where

$$\alpha_N^L = \frac{v_m}{\mu(v_0)}\frac{2}{\pi}\sqrt{3-\frac{4v_m\zeta}{F(\mu_s-\mu_m)}} \tag{4.36}$$

The case of tangential dither with square waveforms, given by equation (3.59), can be adapted to normal dither. It follows that the system will be unstable if

$$\frac{\pi}{2}\mu(v_0)\alpha_N \le v_0 \le v_m\sqrt{1-\frac{\pi^2}{12}\left(\frac{\mu(v_0)\alpha_N}{v_m}\right)^2-\frac{4v_m\zeta}{3F(\mu_s-\mu_m)}} \tag{4.37}$$

In other words, the system with normal dither with square waveforms will be stable at any belt velocity if $\alpha_N \ge \alpha_N^L$, where

$$\alpha_N^L = \frac{v_m}{\mu(v_0)\pi}\sqrt{3-\frac{4v_m\zeta}{F(\mu_s-\mu_m)}} \tag{4.38}$$

For a particular spring-mass-damper system, equations (4.33), (4.35) and (4.37) can be used to compute the stability boundaries and generate stability maps for the Stribeck friction model in the $\alpha_N - v_0$ plane for sinusoidal, triangular and square dither signals, respectively. Figure 4.7 shows the stability map of the dithered system having the Stribeck friction model. Parameter combinations in the unstable region correspond to points where equation (4.32) is satisfied.

The main difference between normal and tangential dither can be seen in comparing Figure 4.7 and Figure 3.5. The lower boundary of the unstable region is slightly more curved in the normal dither case. Also, the required amplitude to stabilize the system is much greater for normal dither than for tangential dither.

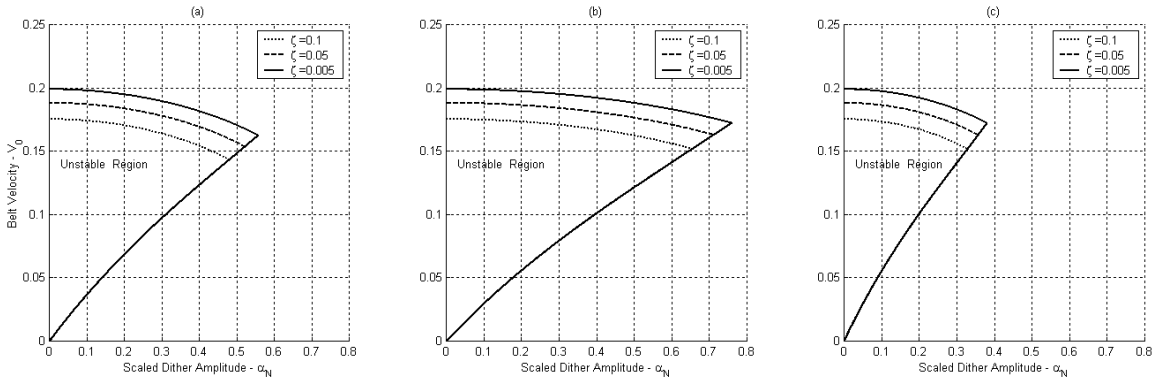

Figure 4.7: Stability map for the Stribeck friction model for three waveforms (a) sinusoidal, (b) triangular, (c) square. Parameters: ζ={0.1, 0.05, 0.005}, F=1, v_m=0.2, μ_s=0.4, and μ_m=0.2857.

Decreasing Friction Law

The stability boundary for the decreasing friction law was obtained analytically in Chapter 3, given by equations (3.63) and (3.67) for triangular and square waveforms, respectively. The case of sinusoidal waveforms requires a numerical evaluation. Based on the results of the previous section, this criterion can be extended to a system with normal dither, by replacing α_T in equations (3.63) and (3.67) by $\mu(v_0)\alpha_N$.

The case of tangential dither with triangular waveforms, given by equation (3.63), can be adapted to normal dither. It follows that the system will be unstable if

$$\frac{\pi}{4}\mu(v_0)\alpha_N \le v_0 \le -v_m \ln\left(\frac{4\zeta\sqrt{\mu(v_0)\alpha_N v_m}}{(\mu_s-\mu_m)\delta F}\right) \tag{4.39}$$

where $\delta \equiv \exp\left(\frac{\pi\alpha_N}{4v_m}\mu(v_0)\right) erf\left(\sqrt{\frac{\pi\alpha_N}{4v_m}\mu(v_0)}\right) + \exp\left(-\frac{\pi\alpha_N}{4v_m}\mu(v_0)\right) erfi\left(\sqrt{\frac{\pi\alpha_N}{4v_m}\mu(v_0)}\right)$.

In other words, the system with normal dither with triangular waveforms will be stable at any belt velocity if $\alpha_N \geq \alpha_N^L$, where α_N^L is the solution of the following

$$\ln\left(\frac{4\zeta v_m}{(\mu_s-\mu_m)\delta F}\sqrt{\frac{\mu(v_0)\alpha_N^L}{v_m}}\right)+\frac{\pi}{4}\frac{\mu(v_0)\alpha_N^L}{v_m}=0 \tag{4.40}$$

The case of tangential dither with square waveforms, given by equation (3.67), can be adapted to normal dither. It follows that the system will be unstable if

$$\frac{\pi}{2}\mu(v_0)\alpha_N \leq v_0 \leq -v_m \ln\left(\frac{\mu(v_0)\zeta\pi\alpha_N}{(\mu_s-\mu_m)F\sinh\left(\mu(v_0)\pi\alpha_N/2v_m\right)}\right) \tag{4.41}$$

In other words, the system with normal dither with square waveforms will be stable at any belt velocity if $\alpha_N \geq \alpha_N^L$, where α_N^L is the solution of the following

$$\ln\left(\frac{\mu(v_0)\zeta\pi\alpha_N^L}{(\mu_s-\mu_m)F\sinh\left(\mu(v_0)\pi\alpha_N^L/2v_m\right)}\right)+\frac{\pi}{2}\mu(v_0)\frac{\alpha_N^L}{v_m}=0 \tag{4.42}$$

For a particular spring-mass-damper system, equations (4.39) and (4.41) can be used to compute the stability boundaries and generate stability maps for the decreasing friction model in the $\alpha_N - v_0$ plane for triangular and square normal dither signals. The stability boundaries for sinusoidal normal dither signals are evaluated numerically. Figure 4.8 shows the stability map of the dithered system having the decreasing friction model. Parameter combinations in the unstable region correspond to points where equation (4.32) is satisfied.

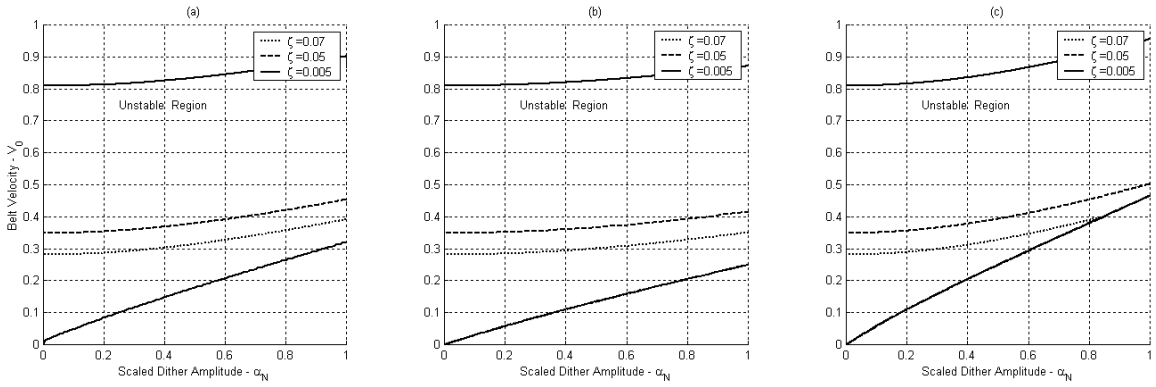

Figure 4.8: Stability map for the decreasing friction model for three waveforms (a) sinusoidal, (b) triangular, (c) square. Parameters: ζ={0.07, 0.05, 0.005}, F=1, v_m=0.2, μ_s=0.4, and μ_m=0.2857.

NUMERICAL RESULTS

In order to assess the validity and accuracy of the predictions of the averaging technique, an extensive numerical study was conducted, similar to the one conducted in Chapter 2.

Two different situations are considered below. In the typical situation, the undithered system is unstable, and dither is used to eliminate the self-excited oscillations. The effectiveness of dither in this type of application is considered in the first section. In the second section, numerical integration is used to explore the opposite situation, where dither causes a stable system to become unstable.

Stabilizing Effect of Dither

In order to quantify the effectiveness of the dither cancellation technique, a metric of performance was calculated for a variety of signal and system parameters. The

performance metric, denoted by E, is the same as that used in Chapter 2 and stated in (2.27).

Figure 4.9 shows contour plots of the metric E as a function of dither amplitude and frequency ratio D_N for a belt velocity $v_0 = 0.05$, using the Stribeck friction model. The isoclines represent identical levels of reduction achieved by dither for pairs of dither parameters $R_N - D_N$. The numerical studies show that, for a constant frequency ratio, the performance increases (E decreases) as D_N is increased. On the other hand, for a constant dither amplitude, the performance increases as the frequency ratio is decreased. For sufficiently high dither frequency ratio, when $R_N > 3$, small reduction ratios (less than 40%) exhibit approximately linear relationships between dither amplitude and frequency ratio. Moreover the 5% reduction ratio seems to correlate very well with the threshold dither parameter obtained using the method of averaging. Note that α_N^* for a particular belt velocity v_0 will correspond to a straight line in the $R_N - D_N$ parameter space

$$D_N = \alpha_N^* \, R_N \tag{4.36}$$

The 5% isocline in the Figure 4.9 plots coincides almost exactly with the boundary predicted by (4.32). For α_N less than α_N^*, the performance gets worse as expected. Moreover, the isoclines become less straight as the performance worsens. For example, when $E = 0.5$, the contour is fairly distorted.

Recall that the averaging results require $1/R_N$ to be a small quantity. As stated above, for $R_N > 3$, there is fairly good agreement between the stability boundaries

obtained from the averaging method and the 5% performance ratio from numerical integration. The lower edge of the stability boundary of case (a) in Figure 4.7 shows that there is an approximately linear relationship between α_N^* and the belt velocity v_0.

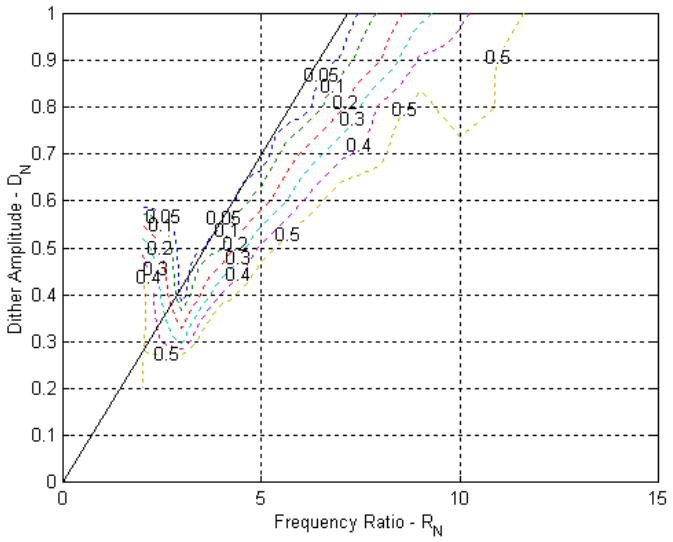

Figure 4.9: Isocline E=5% using the Stribeck friction model. (…) Efficiency metric isocline; (-) Stability boundary using the method of averaging. Parameters: ω_0=1, ζ=0.005, F=1, v_m=0.2, μ_s=0.4, μ_m=0.2857, and v_0=0.05.

Figure 4.10 presents contour plots of the metric E as a function of dither amplitude D_N and frequency ratio R_N, using the decreasing friction model. For the parameter values chosen and for the belt velocity shown, the undithered system is unstable. For sufficiently high dither frequency ratios, when $R_N > 3$, the isoclines for small dither amplitude reduction ratios (lower than 40%) exhibit approximately linear relationships between dither amplitude and frequency ratio. The 5% reduction ratio also seems to correlate well with the stability criterion derived from the method of averaging.

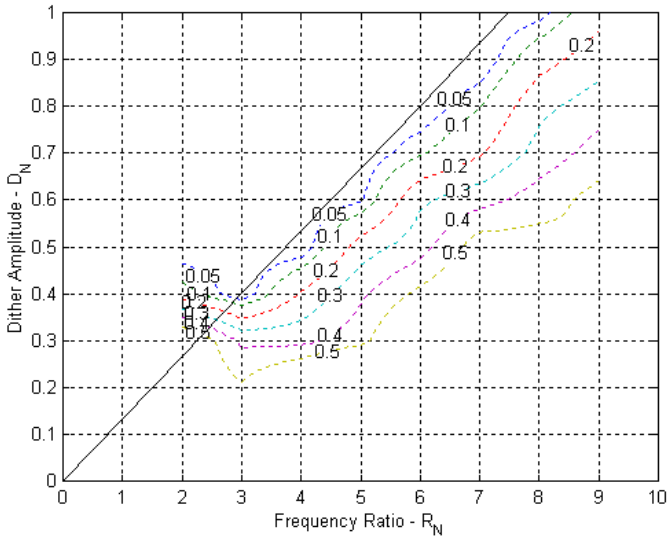

Figure 4.10: Isocline E=5% using the decreasing friction model. (…) Efficiency metric isocline; (-) Stability boundary using the method of averaging. Parameters: ω_0=1, ζ=0.005, F=1, v_m=0.2, μ_s=0.4, μ_m=0.2857, and v_0=0.05.

While the averaging methods are relatively easy to obtain, they cannot provide any information about the performance of the dither technique aside from the stability or instability of the system. The numerical studies reveal a strong correlation between the 5% performance ratio and the averaging method's stability bound. Away from this boundary, the numerical study reveals the conditions under which different degrees of "partial cancellations" are achieved.

Destabilizing Effect of Dither in the Case of the Decreasing Friction Law

As described in the section discussing stability with the decreasing friction law, it is possible to destabilize a stable undithered system by injecting normal dither. To explore this further, numerical simulations are conducted holding the belt velocity and the dither frequency ratio constant, and observing the response as D_N, and thus α_N, is increased. For a particular spring-mass-damper system, Figure 4.11 shows the response

for 6 different values of D_N for normal dither with square waveforms when the belt velocity is $v_0 = 0.075$ and frequency ratio $R_N = 5$. In order to maintain a positive normal force, we must ensure that $D_N < F$. For the system under examination in Figure 4.11 having $R_N = 5$ and $F = 1$, this requires that $\alpha_N < 1/5$.

The top and middle rows in Figure 4.11 show the displacement and velocity response to zero initial conditions, respectively. Note that at $D_N = \alpha_N = 0$, case (a) in Figure 4.11 shows that the undithered system is stable. Thus the system should settle into a quasi-steady equilibrium after the transient vibration dies out.

Using equation (4.41), the averaging method predicts that normal dither with square waveforms should make the system unstable for $\alpha_N = 0.115$, i.e. $D_N = \alpha_N R_N = 0.575$. The system should return to a stable state for $\alpha_N > 0.13$, which corresponds to $D_N > 0.65$. Figure 4.11 qualitatively validates this behavior. However, the system becomes unstable at a higher dither amplitude, i.e. for $D_N \geq 0.7$, and the system is stabilized for dither amplitudes approximately in the range $0.9 \leq D_N \leq 0.95$.

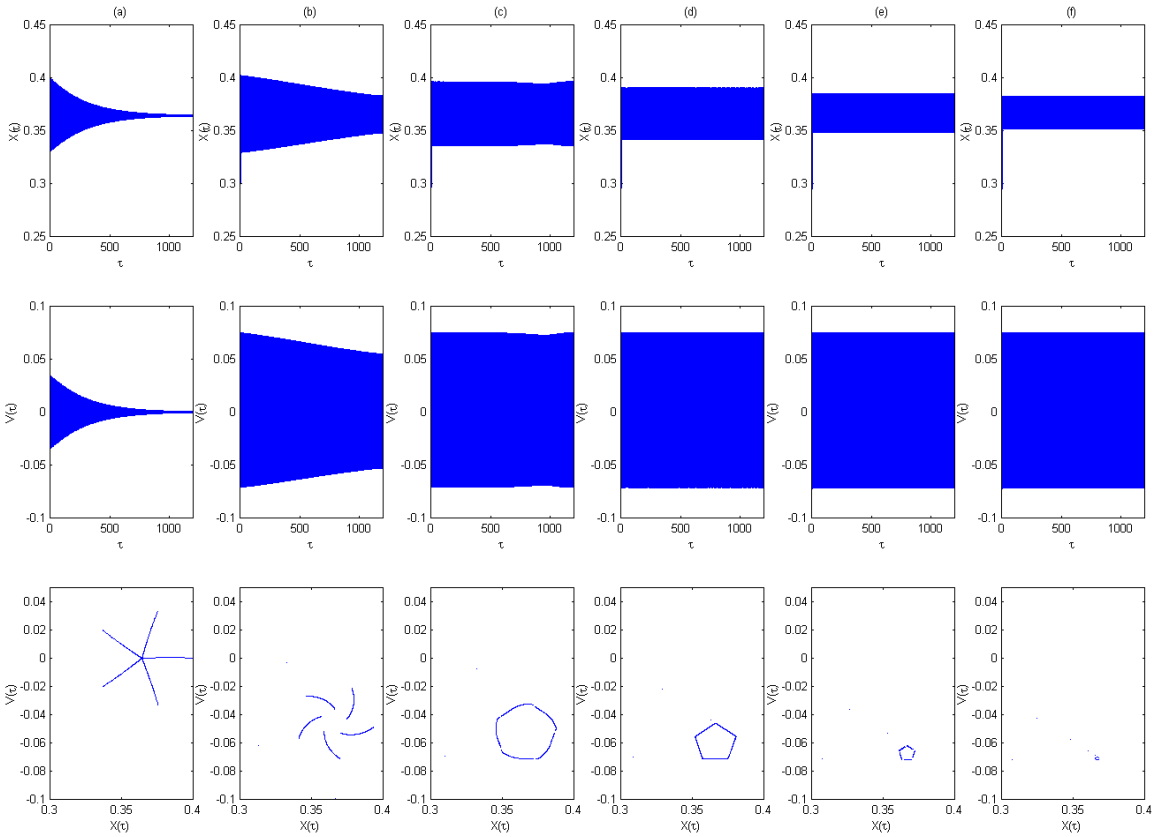

Figure 4.11: System responses with the decreasing friction model, displacements x(τ) (top row), velocities v(τ) (middle row), and Poincaré maps (bottom row) for six values of normal dither amplitude D_N with square waveforms. Parameters: ω_0=1, ζ=0.2, F=1, v_0=0.075, v_m=0.2, μ_s=0.4, μ_m=0.2857, R_N=5, and (a) D_N=0, (b) D_N=0.6, (c) D_N=0.7, (d) D_N=0.8, (e) D_N=0.9, (f) D_N=0.95.

The bottom row of plots in Figure 4.11 shows the Poincaré plots as D_N changes. The Poincaré section is chosen to coincide with the time instants $R_N\tau_n = 2n\pi$ for $n = 0,\ 1,\ 2,\ \ldots$ During "stable" response, the Poincaré plot spirals down to a period-1 response, like cases (a), (b) and (f). When the dither signal destabilizes the system, the Poincaré plot shows a closed-orbit, closely resembling a period-5 response. It appears that the dither signal is successful in smoothing the nonlinearity, so that the low-frequency response is at or near ω_0, even though the limit-cycle oscillation occurs typically at a lower frequency. In the case of an unstable response, this sustained low-

frequency response component is joined to a second component at the dither frequency and harmonics thereof.

As mentioned in Chapter 2, it is very difficult to pinpoint the exact value of D_N (or α_N) at which the stability of the system switches. Therefore, an exhaustive numerical study was not conducted on the potential destabilizing effects of dither. It is nonetheless clear from the numerical simulations that it is indeed possible to destabilize a system by injecting dither into a system. The dither can be tangential or normal in nature, and need not be sinusoidal.

Robustness to a Variety of Initial Conditions

A numerical study has been performed to assess the robustness of normal dither efficacy to a variety of initial conditions. The system has been time-integrated using a grid of initial conditions in the $x_0 - \dot{x}_0$ plane.

Although multiple solutions have not been encountered in this study, their existence in other parameter regions is still an open question.

CONCLUSION

It is found that unstable, self-excited oscillations in the system having the Stribeck friction and with the decreasing friction models can be stabilized by applying normal dither for some system parameters, but not in general.

The averaging technique developed in Chapter 2 for tangential dither has been extended to normal dither. A numerical procedure for computing effective friction characteristic when normal dither is injected in the system has been implemented. The

effective friction characteristics obtained with the extended averaging technique are in agreement with the ones obtained with the numerical procedure.

Amplitude-frequency combinations that cause the steady-state dithered response to decrease to 5% of the undithered response show a very repeatable correlation with the stability boundary predicted by the averaging technique.

As found in Chapter 2, the system with the decreasing friction model, unlike with the Stribeck friction model, can also be destabilized by dither. Both the averaging technique and numerical simulations show that an undithered stable system can be destabilized by applying dither for some system parameters. When the undithered system is unstable, unlike the case of tangential dither, it is not always possible to find a normal dither signal that stabilizes the system, since the dither amplitude is limited by the requirement that the total normal force be positive.

CHAPTER 5

CONTINUOUS PLATE MODEL

This chapter derives the governing equations of motions for the vibration of a stationary disc under a rotating friction load. The disc rotor is modeled by a thin, clamped-free annular plate. The plate model is described in terms of a finite modal summation. The frictional contact load is represented by a follower force. The stability of the combined system, with and without dither signals, is assessed using multiple-scale analysis.

For modeling purposes, the combined rotor-caliper model is shown in Figure 5.1. The brake rotor is modeled using thin plate theory and a modal procedure. In reality, an automotive brake rotor is not that thin; for example a typical h/a value would be 0.15. Also, brake rotors are usually not homogeneous due to the presence of cooling fins (channels) incorporated into the cast-iron part. Although the thin plate assumption may not be highly accurate, it provides an analytical framework that can lead to a deeper physical understanding of the squealing mechanism. In particular, through the inclusion of many modes, it is possible to study the stability mechanisms tied to modal coupling or *mode coalescence*. It also allows considering resonance type phenomena when a dither frequency is near a system natural frequency.

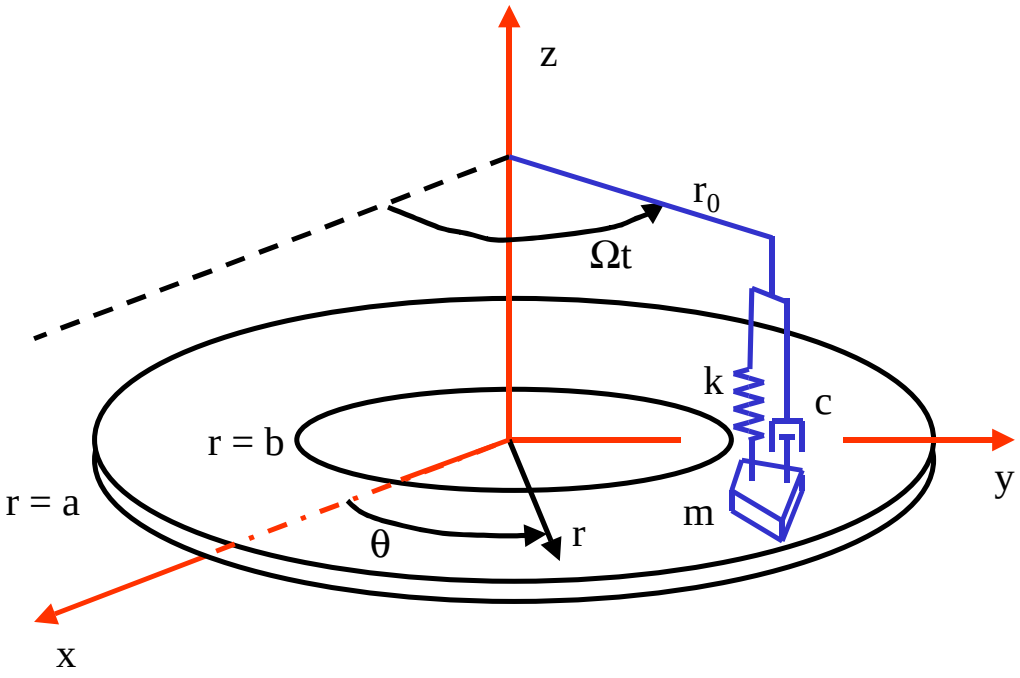

Figure 5.1: Annular plate with rotating spring-mass-damper system

Since the dither frequencies can be quite high, the model uses the exact modes of a clamped free annular plate, having an arbitrary number of nodal circles and nodal diameters. In contrast, mode-based models usually utilize the exact dependence on θ (in terms of azimuthal harmonics $\cos(n\theta)$ and $\sin(n\theta)$) but only use a cubic approximation for the radial dependence of each mode. Another requirement satisfied by this model is that it displays the correct qualitative trends in the natural frequencies as a function of thickness, inner and outer radii, number of nodal diameters and number of nodal circles. Although disc rotation is not explicitly included, previous researchers have shown that this effect is small in typical brake rotor applications [49].

EQUATIONS OF MOTION

The equation of transverse vibration of a stationary disc excited by a rotating spring-mass-damper (SMD) system with dry friction may be expressed

$$\rho h \frac{\partial^2 w(r,\theta,t)}{\partial t^2} + D^* \nabla^4 \frac{\partial w(r,\theta,t)}{\partial t} + D\nabla^4 w(r,\theta,t) = F(r,\theta,t) \tag{5.1}$$

where $D = \frac{Eh^3}{12\left(1-\upsilon^2\right)}$, E is the elastic modulus, h is the thickness, υ is Poisson's ratio, ρ is the mass density, and $F(r,\theta,t)$ is the force per unit area applied by the brake pad, or by other external means. D^* is a linear damping coefficient meant to account for light structural damping. In this Chapter, all cases considered use the following parameter values: $E = 1.95\times10^{11}\ Pa$, $\upsilon = 0.3$ and $\rho = 7700\ kg.m^{-3}$.

The term ∇^4 is the bi-harmonic operator, given in polar coordinates as

$$\nabla^4 = \left(\frac{\partial^2 w}{\partial r^2} + \frac{1}{r}\frac{\partial w}{\partial r} + \frac{1}{r^2}\frac{\partial^2 w}{\partial \theta^2} \right)^2 \tag{5.2}$$

As seen in Figure 5.1, it is assumed that the plate is clamped at its inner radius, $r = b$:

$$w(r=b,\theta,t) = 0 \tag{5.3a}$$

$$\frac{\partial w(r=b,\theta,t)}{\partial r} = 0 \tag{5.3b}$$

At the plate's outer radius, $r = a$, boundary conditions of zero moment and zero shear are applied:

$$M_r(r=a,\theta,t) = -D\left[\frac{\partial^2 w}{\partial r^2} + \upsilon\left(\frac{1}{r}\frac{\partial w}{\partial r} + \frac{1}{r^2}\frac{\partial^2 w}{\partial \theta^2}\right)\right] = 0 \tag{5.4a}$$

$$V_r(r=a,\theta,t) = -D\frac{\partial}{\partial r}\nabla^2 w - \frac{D}{r}(1-\upsilon)\frac{\partial^2}{\partial r \partial \theta}\left[\frac{1}{r}\frac{\partial w}{\partial \theta}\right] = 0 \tag{5.4b}$$

or

$$\frac{\partial}{\partial r}\left(\frac{\partial^2 w}{\partial r^2} + \frac{1}{r}\frac{\partial w}{\partial r} + \frac{1}{r^2}\frac{\partial^2 w}{\partial \theta^2}\right) + \frac{1-\upsilon}{r^2}\frac{\partial}{\partial \theta^2}\left(\frac{\partial w}{\partial r} - \frac{w}{r}\right) = 0 \tag{5.5}$$

SOLUTION OF THE HOMOGENEOUS EQUATION

The exact solution to the homogeneous annular plate equation was developed by Vogel and Skinner [50]. Once the eigenfunctions have been found, the displacement of any point of the plate can be expanded as

$$w(r,\theta,t) = \sum_{i=1}^{N_r}\sum_{j=0}^{N_\theta} R_{ij}(r)\left(\, q_{ij}^c(t)\cos(j\theta) + q_{ij}^s(t)\sin(j\theta)\right) \tag{5.6}$$

where $R_{ij}(r)$ contains the radial dependence of the eigenfunction, the index i designates the number of nodal circles, including the clamped location along the inner radius, the index j designates the number of nodal diameters, and $q_{i0}^s(t) \equiv 0$ for $i = 1,\ 2,\ ...$

The eigenfunctions are assumed to be normalized so that:

$$\int_b^a \int_0^{2\pi} \rho h\left(R_{ij}(r)\cos(j\theta)\right)^2 r\ dr\ d\theta = 1 \tag{5.7a}$$

$$\int_b^a \int_0^{2\pi} \rho h\left(R_{ij}(r)\sin(j\theta)\right)^2 r\ dr\ d\theta = 1 \tag{5.7b}$$

and

$$\int_b^a \int_0^{2\pi} \left(R_{ij}(r)\cos(j\theta)\right) D\nabla^4 \left(R_{ij}(r)\cos(j\theta)\right) r\ dr\ d\theta = \omega_{ij}^2 \tag{5.8a}$$

$$\int_b^a \int_0^{2\pi} \left(R_{ij}(r)\sin(j\theta)\right) D\nabla^4 \left(R_{ij}(r)\sin(j\theta)\right) r\ dr\ d\theta = \omega_{ij}^2 \tag{5.8b}$$

where ω_{ij} is the natural frequency of mode (i, j), i.e. having i nodal circles and j nodal diameters.

The orthogonality property of the eigenfunctions implies that:

$$\int_b^a \int_0^{2\pi} \rho h R_{ij}(r)\cos(j\theta) R_{pq}(r)\cos(q\theta)\ r\ dr\ d\theta = \delta_{ip}\delta_{jq} \tag{5.9a}$$

$$\int_b^a \int_0^{2\pi} \rho h R_{ij}(r)\cos(j\theta) R_{pq}(r)\sin(q\theta)\ r\ dr\ d\theta = 0 \quad \forall i, j, p, q \tag{5.9b}$$

$$\int_b^a \int_0^{2\pi} \left(R_{ij}(r)\cos(j\theta)\right) D\nabla^4 \left(R_{pq}(r)\cos(q\theta)\right) r\ dr\ d\theta = \omega_{ij}^2 \delta_{ip}\delta_{jq} \tag{5.9c}$$

$$\int_b^a \int_0^{2\pi} \left(R_{ij}(r)\cos(j\theta)\right) D\nabla^4 \left(R_{pq}(r)\sin(q\theta)\right) r\ dr\ d\theta = 0 \quad \forall i, j, p, q \tag{5.9d}$$

where $\delta_{ij} = 1$ if $i = j$ and is zero otherwise.

Samples of the modal functions, also referred to as *eigenfunctions* or *mode shapes*, for a clamped-free annular plate with $b/a = 0.5$ are shown in Figures 5.2.

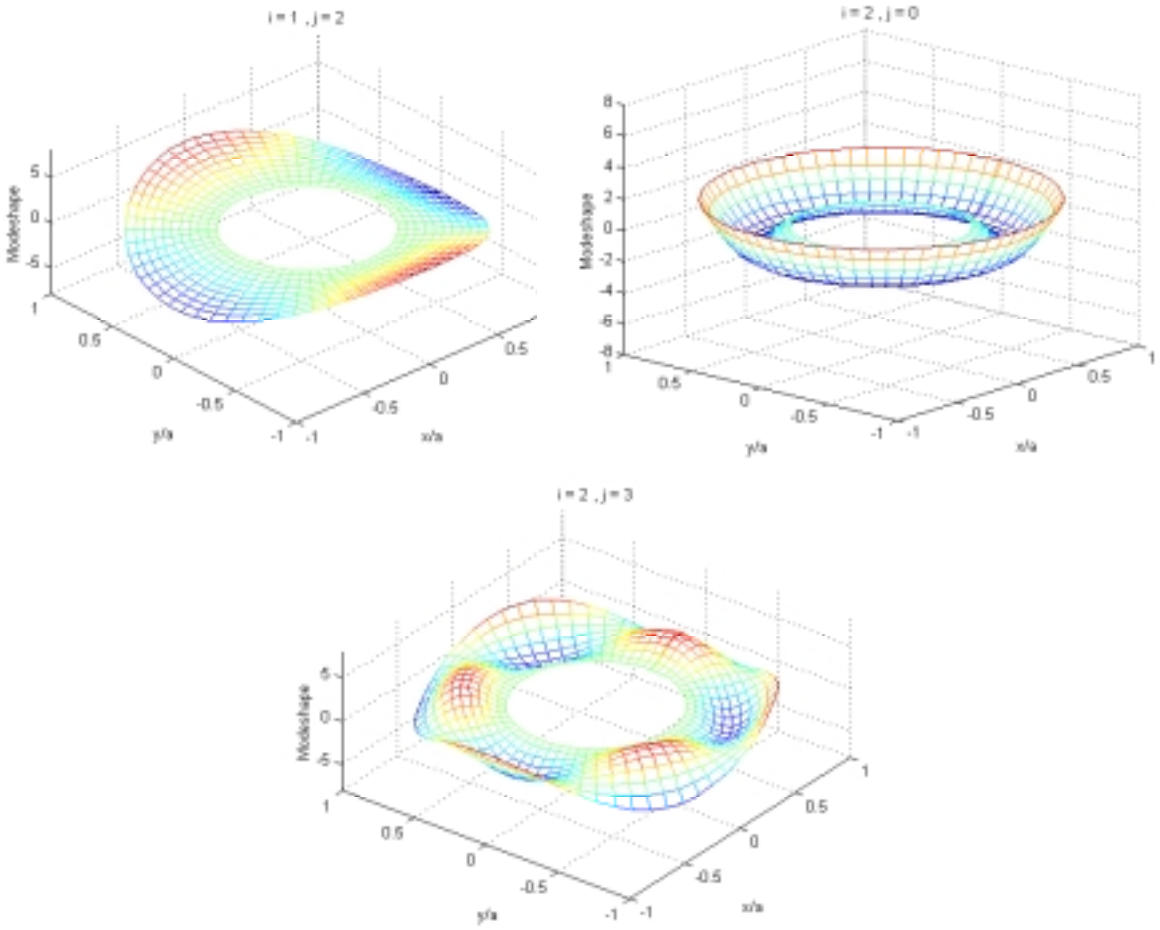

Figure 5.2: Annular plate modes with b/a=0.5, (a) i=1, j=2, (b) i=2, j=0, (c) i=2, j=3

SOLUTION OF THE FORCED EQUATION

The forcing $F(r,\theta,t)$ on the right hand side of equation (5.1) provides a means by which the annular plate model can be coupled to a contacting dynamic system. In this case a rotating mass-spring-damper (SMD) system similar to the one studied by Iwan et al. [9, 10] is considered. The SMD system rotates at a (dimensional) angular velocity $\tilde{\Omega}$. The downward contact force is dependent on m, k, and c as well as on the vertical motion of the plate at the contact point. Note that for disc brake system applications,

there are normal forces on both the inboard and outboard sides of the rotor. It is assumed that there is no net normal force due to the static brake pressure.

It is known that friction can have a destabilizing effect in rotational systems. To understand this phenomenon, a friction follower force is included at the contact point. The follower force, denoted as F_θ, is assumed initially to be constant in magnitude but tangent to the local contact surface at all times. The assumption of constant magnitude follower force is consistent with the assumption that the brake force is much larger than the variable forces due to m, c, and k. (When dither is considered, the assumption of constant magnitude will be relaxed.) In this case, $F(r,\theta,t)$ can be expressed as

$$F(r,\theta,t) = -\delta(\theta - \tilde{\Omega}t)\frac{\delta(r-r_0)}{r}\left[m\left(\frac{\partial}{\partial t} + \tilde{\Omega}\frac{\partial}{\partial \theta}\right)^2 + c\left(\frac{\partial}{\partial t} + \tilde{\Omega}\frac{\partial}{\partial \theta}\right) + k - \frac{F_\theta}{r}\frac{\partial}{\partial \theta}\right] w(r,\theta,t) \tag{5.10}$$

where $\delta(.)$ denotes the Dirac delta function. At this point, the modal expansion (5.6) can be substituted into (5.10) with the result being substituted into (5.1). Invoking the orthogonality of the eigenfunctions would result in a set of coupled, linear ordinary differential equations in time. Unfortunately, these equations would have periodic coefficients, making the determination of stability more difficult to ascertain. Later, this formulation is used as a basis for approximate analyses. Alternatively, Iwan and Stahl [9] introduced a rotating reference frame, where the location of the mass-spring-damper system is fixed at $\phi = 0$

$$\phi = \theta - \tilde{\Omega}t \tag{5.11}$$

Using the angle ϕ, expansion (5.6) can be re-written in the form

$$w(r,\theta,t)=\hat{w}(r,\phi,t)=\sum_{i=1}^{N_r}\sum_{j=0}^{N_\theta} R_{ij}(r)\left(A_{ij}(t)\cos(j\phi)+B_{ij}(t)\sin(j\phi)\right) \tag{5.12}$$

It must be realized that derivatives with respect to t must include the effect of the rotating frame; in light of (5.11) the partial derivatives in the moving reference frame become:

$$\frac{d}{dt}\rightarrow\frac{\partial}{\partial t}+\frac{\partial}{\partial\phi}\frac{\partial\phi}{\partial t}=\frac{\partial}{\partial t}-\tilde{\Omega}\frac{\partial}{\partial\phi} \tag{5.13a}$$

$$\frac{d^2}{dt^2}\rightarrow\frac{\partial^2}{\partial t^2}-2\tilde{\Omega}\frac{\partial^2}{\partial\phi\partial t}+\tilde{\Omega}^2\frac{\partial^2}{\partial\phi^2} \tag{5.13b}$$

$$\frac{\partial}{\partial\theta}\rightarrow\frac{\partial}{\partial\phi} \tag{5.13c}$$

Substitution of (5.13) into (5.1) and (5.10) yields

$$\begin{aligned}\rho h\left(\frac{\partial^2}{\partial t^2}-2\tilde{\Omega}\frac{\partial^2}{\partial\phi\partial t}+\tilde{\Omega}^2\frac{\partial^2}{\partial\phi^2}\right)\hat{w}(r,\phi,t)+D\nabla^4\hat{w}(r,\phi,t)=\\ -\delta(\phi)\frac{\delta(r-r_0)}{r}\left(m\frac{\partial^2}{\partial t^2}+c\frac{\partial}{\partial t}+k-\frac{F_\theta}{r}\frac{\partial}{\partial\phi}\right)\hat{w}(r,\phi,t)\end{aligned} \tag{5.14}$$

When the expansion (5.12) is substituted into (5.14) and orthogonality of the eigenfunctions is invoked, a set of linear ordinary differential equations in time is obtained. Unlike in the fixed reference frame, the equations have constant coefficients, so stability can be determined by a mere eigenvalue calculation. The form of the differential equations is

$$\ddot{A}_{pq} - 2q\tilde{\Omega}\dot{B}_{pq} + \left(\omega_{pq}^2 - q^2\tilde{\Omega}^2\right)A_{pq} = -\sum_{i=1}^{N_r}\sum_{j=0}^{N_\theta} R_{ij}(r_0)R_{pq}(r_0)\left(m\ddot{A}_{ij} + c\dot{A}_{ij} + kA_{ij} - \frac{F_\theta}{r_0}jB_{ij}\right) \tag{5.15}$$

$$\ddot{B}_{pq} + 2q\tilde{\Omega}\dot{A}_{pq} + \left(\omega_{pq}^2 - q^2\tilde{\Omega}^2\right)B_{pq} = 0 \qquad for\ p = 1,2,...;\ q = 0,1,2,...$$

where the generalized coordinate B_{p0} may be discarded for $p = 1,2,...$

The following new variables are introduced, as defined in Chan et al. [51].

$$\tau = \omega_{cr}t, \quad \beta_{pq} = \frac{\omega_{pq}}{\omega_{cr}}, \quad \Omega = \frac{\tilde{\Omega}}{\omega_{cr}} \tag{5.16}$$

where the critical frequency is defined as

$$\omega_{cr} = \min\left[\frac{\omega_{pq}}{q};\ \mathrm{p} = 1,2,...,N_r;\ q = 1,2,...,N_\theta\right] \tag{5.17}$$

The scaled equations of motion are

$$\frac{d^2A_{pq}}{d\tau^2} - 2q\Omega\frac{dB_{pq}}{d\tau} + \left(\beta_{pq}^2 - q^2\Omega^2\right)A_{pq} = -\sum_{i=1}^{N_r}\sum_{j=0}^{N_\theta} R_{ij}(r_0)R_{pq}(r_0)\left(m\frac{d^2A_{pq}}{d\tau^2} + \frac{c}{\omega_{cr}}\frac{dA_{pq}}{d\tau} + \frac{k}{\omega_{cr}^2}A_{ij} - \frac{F_\theta j}{r_0\omega_{cr}^2}B_{ij}\right) \tag{5.18}$$

$$\frac{d^2B_{pq}}{d\tau^2} + 2q\Omega\frac{dA_{pq}}{d\tau} + \left(\beta_{pq}^2 - q^2\Omega^2\right)B_{pq} = 0 \qquad for\ p = 1,2,...;\ q = 0,1,2,...$$

It is noted that equation (5.18) constitutes $N_{tot} = N_r\left(2N_\theta + 1\right)$ linear, second-order differential equations with constant coefficients. A vector of generalized coordinates, denoted by $\tilde{y}$, may be defined as

$$\tilde{y} = \left[A_{10} \;\; A_{11} \cdots A_{1N_\theta} \;\; \cdots A_{N_r N_\theta} \;\; B_{11} \;\; B_{12} \cdots B_{1N_\theta} \;\; \cdots B_{N_r N_\theta} \right]^T \tag{5.19}$$

Then, a state vector $\tilde{x}$ can be formed from $\tilde{y}$ and its derivative with respect to τ

$$\tilde{x} = \begin{Bmatrix} \tilde{y} \\ \dfrac{d\tilde{y}}{d\tau} \end{Bmatrix} \tag{5.20}$$

Using $\tilde{x}$, equation (5.18) can be cast in the form

$$\frac{d\tilde{x}}{d\tau} = \left[A(\Omega) \right] \; \tilde{x} \tag{5.21}$$

where $\left[A(\Omega) \right]$ is a $2N_{tot} \times 2N_{tot}$ matrix function of the scaled rotation speed, Ω. The eigenvalues of (5.21) can be computed as a function of scaled rotation speed and examined for stability.

STABILITY WITHOUT DITHER

The supercritical range of the scaled rotational speed, i.e. $\Omega > 1$, is generally not a concern for engineering applications such as brake systems. The only influential parameter in the subcritical range of the scaled rotational speed, i.e. $0 < \Omega \leq 1$, is the friction follower force amplitude F_θ. Figures 5.3 to 5.5 show typical stability maps.

Figure 5.3 depicts a stability map for a plate having $h/a = 0.01$, $b/a = 0.05$, $r_0/a = 0.5$. Two sets of values for the SMD properties m, c/ω_{crit}, and k/ω_{crit}^2 are examined. The stability of this system is computed using one radial mode and three azimuthal modes, i.e. $N_r = 1$ and $N_\theta = 2$. Figure 5.3 shows a region mostly stable for the scaled friction force $f = F_\theta / r_0 \omega_{crit}^2$ lower than 1×10^{-5} and 1×10^{-6}, in case (a) and case

(b), respectively. Nevertheless, several thin bands of instability arise as the scaled friction force is increased.

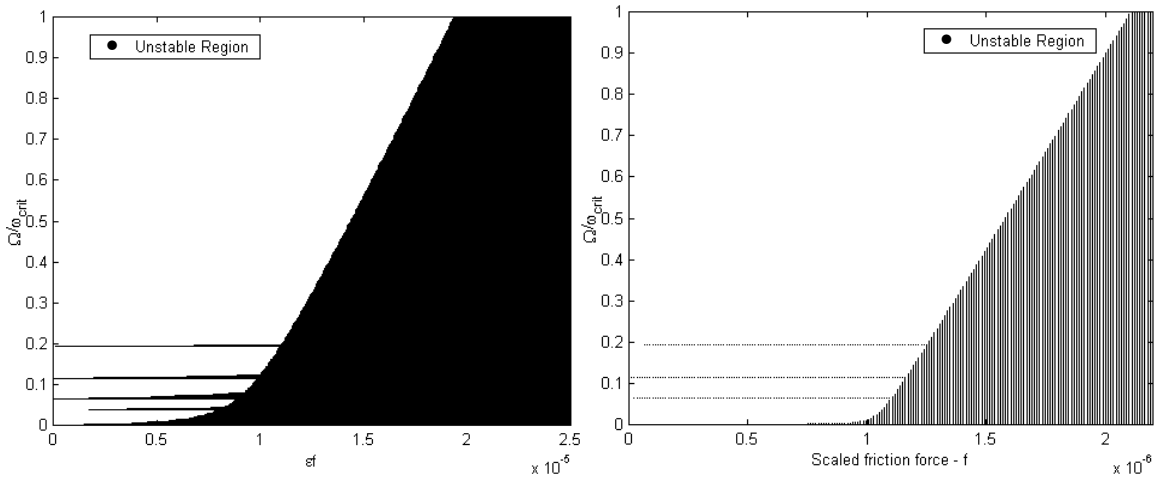

Figure 5.3: Stability map as a function of scaled rotational speed Ω and scaled friction force $f=F_\theta/r_0\omega^2_{crit}$. Parameters: h/a=0.01, b/a=0.05, $r_0/a=0.5$, $N_r=1$, $N_\theta=2$, (a) $m=c/\omega_{crit}=k/\omega^2_{crit}=0.1$, and (b) $m=c/\omega_{crit}=k/\omega^2_{crit}=0.01$.

Figure 5.4 depicts a stability map for identical system parameters, except that the model has been enriched to represent up to six azimuthal modes, i.e. $N_\theta = 5$. The same bands of instability are found in this plot, but additional unstable regions are also present. The addition of azimuthal modes seems to have created additional instability regions. Figure 5.5 depicts a stability map for identical system parameters as Figure 5.4, except that the model has been enriched to represent up to two radial modes, i.e. $N_r = 2$. The same bands of instability are found in this plot, and additional unstable regions are also present now. It may be concluded that both radial and azimuthal modes add new unstable rotational speeds to the system.

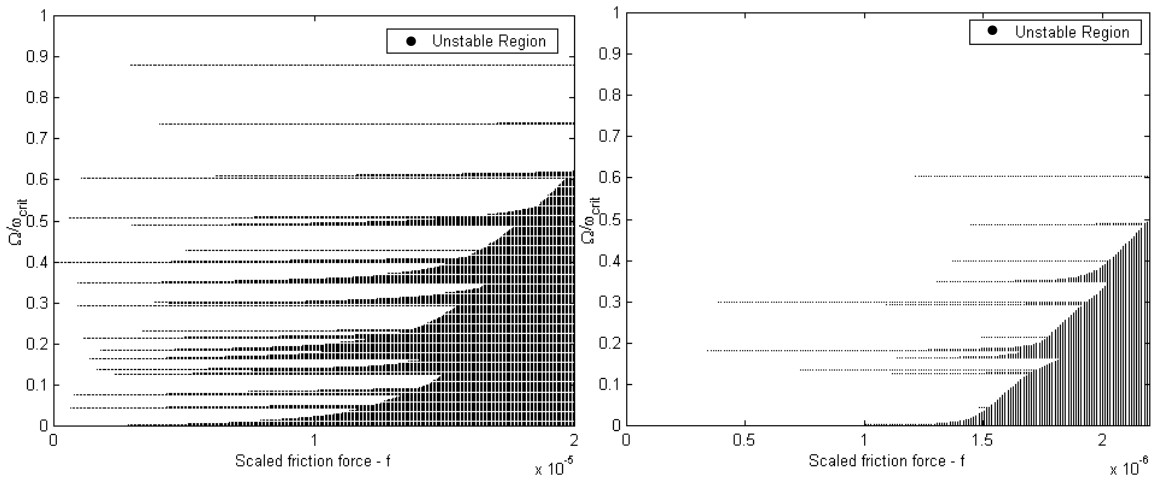

Figure 5.4: Stability map as a function of scaled rotational speed Ω and scaled friction force $f=F_\theta/r_0\omega^2_{crit}$. Parameters: h/a=0.01, b/a=0.05, $r_0/a=0.5$, $N_r=1$, $N_\theta=5$, (a) $m=c/\omega_{crit}=k/\omega^2_{crit}=0.1$, and (b) $m=c/\omega_{crit}=k/\omega^2_{crit}=0.01$.

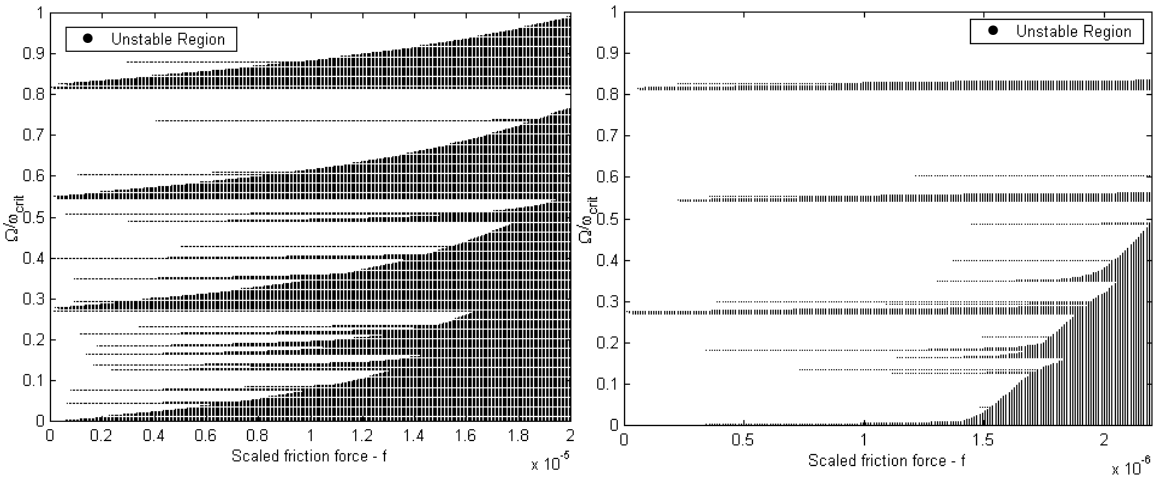

Figure 5.5: Stability map as a function of scaled rotational speed Ω and scaled friction force $f=F_\theta/r_0\omega^2_{crit}$. Parameters: h/a=0.01, b/a=0.05, $r_0/a=0.5$, $N_r=2$, $N_\theta=5$, (a) $m=c/\omega_{crit}=k/\omega^2_{crit}=0.1$, and (b) $m=c/\omega_{crit}=k/\omega^2_{crit}=0.01$.

EQUATION FOR THE DITHERED SYSTEM

Normal Dither

Applying a dither signal to the normal load in the system results in a time varying normal force, which in turn induces a time varying friction force. Thus the friction follower force has both a constant and an oscillatory component. In this case the force $F(r,\theta,t)$ can be expressed as

$$F(r,\theta,t) = -\delta(\theta-\tilde{\Omega}t)\frac{\delta(r-r_0)}{r}\left[m\left(\frac{\partial}{\partial t}+\tilde{\Omega}\frac{\partial}{\partial\theta}\right)^2 + c\left(\frac{\partial}{\partial t}+\tilde{\Omega}\frac{\partial}{\partial\theta}\right)+k-\frac{F_\theta}{r}\left(1+\alpha\cos(\omega t+\psi_0)\right)\frac{\partial}{\partial\theta}\right]w(r,\theta,t) \tag{5.22}$$

where α, ω and ψ_0 denote the normal dither amplitude, frequency, and initial phase angle, respectively. It is important to note that the dither amplitude parameter α cannot exceed unity because it would give rise to time intervals of negative friction force. This physical constraint for normal dither can be stated as follows

$$0<\alpha<1 \qquad \text{with } \alpha\in\mathbb{R} \tag{5.23}$$

Substitution of (5.13) into (5.1) and (5.22) yields

$$\rho h\left(\frac{\partial^2}{\partial t^2}-2\tilde{\Omega}\frac{\partial^2}{\partial\phi\partial t}+\tilde{\Omega}^2\frac{\partial^2}{\partial\phi^2}\right)\hat{w}(r,\phi,t)+D\nabla^4\hat{w}(r,\phi,t) = -\delta(\phi)\frac{\delta(r-r_0)}{r}\left[m\frac{\partial^2}{\partial t^2}+c\frac{\partial}{\partial t}+k-\frac{F_\theta}{r}\left(1+\alpha\cos(\omega t+\psi_0)\right)\frac{\partial}{\partial\phi}\right]\hat{w}(r,\phi,t) \tag{5.24}$$

When the expansion (5.12) and the variables (5.16) are substituted into (5.24) and orthogonality of the eigenfunctions is invoked, a set of linear ordinary differential

equations in time is obtained. Unlike in the case without dither excitation, the equations now have time dependent coefficients. The form of the scaled differential equations is

$$\frac{d^2A_{pq}}{d\tau^2} - 2q\Omega\frac{dB_{pq}}{d\tau} + \left(\beta_{pq}^2 - q^2\Omega^2\right)A_{pq} = -\sum_{i=1}^{N_r}\sum_{j=0}^{N_\theta} R_{ij}(r_0)R_{pq}(r_0) \times\left[m\frac{d^2A_{pq}}{d\tau^2} + \frac{c}{\omega_{cr}}\frac{dA_{pq}}{d\tau} + \frac{k}{\omega_{cr}^2}A_{ij} - \frac{F_\theta j}{r_0\omega_{cr}^2}\left(1+\alpha\cos(R\tau+\psi_0)\right)B_{ij}\right] \quad (5.25)$$

$$\frac{d^2B_{pq}}{d\tau^2} + 2q\Omega\frac{dA_{pq}}{d\tau} + \left(\beta_{pq}^2 - q^2\Omega^2\right)B_{pq} = 0 \qquad for\ p = 1,2,...;\ q = 0,1,2,...$$

where $R = \dfrac{\omega}{\omega_{cr}}$ is the dither frequency ratio.

Tangential Dither

Applying a dither signal tangentially to the plane at the contact point corresponds to effectively forcing the mass into a tangential oscillatory motion around its mean rotational motion on the plate. If the mass can be forced into an angular displacement $\varphi(t)$ such that its effect on the mass total rotation are negligible, i.e. $\Omega t + \varphi(t) \simeq \Omega t$, and its slip velocity is mainly oscillatory, i.e. $\Omega + \dot{\varphi}(t) \quad \dot{\varphi}(t)$, then the follower friction force will be periodic. Both conditions can be fulfilled if the angular displacement engendered by tangential dither is taken as follows

$$\varphi(t) = \varphi_0 \sin(\omega t) \quad with\ \varphi_0 = O\left(\omega^{n_1}\right)\ and\ -1 < n_1 < 0 \qquad (5.26)$$

where φ_0 is the amplitude of the angular displacement and ω is the tangential dither frequency. If the tangential dither frequency is high enough, the mass' total rotation and slip velocity in the limit of dither frequency going to infinity is given by

$$\lim_{\omega\to\infty}\left\{\Omega t+\varphi(t)\right\}=\lim_{\omega\to\infty}\left\{\Omega t+\varphi_0\sin(\omega t)\right\}=\Omega t \tag{5.27}$$

$$\lim_{\omega\to\infty}\left\{\Omega+\dot{\varphi}(t)\right\}=\lim_{\omega\to\infty}\left\{\Omega+\omega\,\varphi_0\cos(\omega t)\right\}=\dot{\varphi}(t) \tag{5.28}$$

Note that the tangential dither force D_T required to create an oscillatory friction follower force could be very high as

$$D_T=O\left(\ddot{\varphi}(t)\right)=O\left(\omega^{n_2}\right)\ \ and\ 1<n_2<2 \tag{5.29}$$

Since the slip velocity is changing sign, the friction force becomes oscillatory, alternating values between $+F_\theta$ and $-F_\theta$ if a constant friction coefficient is assumed. The friction follower force is then a square wave with fundamental frequency equal to that of the tangential dither frequency. In order to proceed with this analysis, only the fundamental frequency is considered. In other words, the friction follower force is assumed to be sinusoidal of the form $F_\theta\cos(\omega t+\psi_0)$.

Forced by a tangential dither as defined in (5.29), the rotating spring-mass-damper system force $F(r,\theta,t)$ can still be expressed as

$$\begin{aligned}F(r,\theta,t)=-\delta(\theta-\tilde{\Omega}t)\frac{\delta(r-r_0)}{r}\Bigg[&m\left(\frac{\partial}{\partial t}+\tilde{\Omega}\frac{\partial}{\partial\theta}\right)^2\\&+c\left(\frac{\partial}{\partial t}+\tilde{\Omega}\frac{\partial}{\partial\theta}\right)+k-\frac{F_\theta\cos(\omega t+\psi_0)}{r}\frac{\partial}{\partial\theta}\Bigg]w(r,\theta,t)\end{aligned} \tag{5.30}$$

where ω and ψ_0 denotes the tangential dither frequency and the initial phase angle, respectively.

Substitution of (5.13) into (5.1) and (5.30) yields

$$\rho h\left(\frac{\partial^2}{\partial t^2}-2\tilde{\Omega}\frac{\partial^2}{\partial\phi\partial t}+\tilde{\Omega}^2\frac{\partial^2}{\partial\phi^2}\right)\hat{w}(r,\phi,t)+D\nabla^4\hat{w}(r,\phi,t)= \\ -\delta(\phi)\frac{\delta(r-r_0)}{r}\left[m\frac{\partial^2}{\partial t^2}+c\frac{\partial}{\partial t}+k-\frac{F_\theta\cos(\omega t+\psi_0)}{r}\frac{\partial}{\partial\phi}\right]\hat{w}(r,\phi,t) \tag{5.31}$$

When the expansion (5.12) and the variables (5.16) are substituted into (5.31) and orthogonality of the eigenfunctions is invoked, a set of linear ordinary differential equations in time is obtained

$$\frac{d^2A_{pq}}{d\tau^2}-2q\Omega\frac{dB_{pq}}{d\tau}+\left(\beta_{pq}^2-q^2\Omega^2\right)A_{pq}=-\sum_{i=1}^{N_r}\sum_{j=0}^{N_\theta}R_{ij}(r_0)R_{pq}(r_0) \\ \times\left[m\frac{d^2A_{pq}}{d\tau^2}+\frac{c}{\omega_{cr}}\frac{dA_{pq}}{d\tau}+\frac{k}{\omega_{cr}^2}A_{ij}-\frac{F_\theta j}{r_0\omega_{cr}^2}\cos(R\tau+\psi_0)B_{ij}\right] \tag{5.32}$$

$$\frac{d^2B_{pq}}{d\tau^2}+2q\Omega\frac{dA_{pq}}{d\tau}+\left(\beta_{pq}^2-q^2\Omega^2\right)B_{pq}=0 \qquad for\ p=1,2,...;\ q=0,1,2,...$$

where $R=\dfrac{\omega}{\omega_{cr}}$ is the dither frequency ratio.

STABILITY OF THE DITHERED SYSTEM

Unlike in the equations of motion without dither (5.18), equations (5.25) and (5.32) have time dependent coefficients, so stability cannot be determined by an eigenvalue calculation. A crucial feature of the coefficients of equations (5.25) and (5.32) is that they are periodic with period $T=2\pi/R$. The periodicity in the coefficients allows the use of Floquet theory to obtain the system stability.

When the parameters of the rotating spring-mass-damper system are very small, a perturbation method may be used to approximate the solution. The method of multiple

scales is used to infer stability in an analytical fashion. The validity of the stability predictions lies in the assumption of small parameters.

Floquet Theory

Floquet theory is described in many dynamics textbooks, for example see [28, 29, 52] for an in-depth treatment. The following definitions and theorems are taken from Jordan and Smith's textbook [29]:

Definition 5.1:

Let $\phi_1(t),\ \phi_2(t),\ ...,\ \phi_n(t)$ *be n linearly independent solution vectors of the homogeneous system* $\dot{x} = A(t)x$. *Then the matrix*

$$\Phi(t) = \left[\phi_1(t),\ \phi_2(t),\ ...,\ \phi_n(t)\right] = \begin{bmatrix} \phi_{11} & \phi_{12} & \cdots & \phi_{1n} \\ \phi_{21} & \phi_{22} & \cdots & \phi_{2n} \\ & & & \\ \phi_{n1} & \phi_{n2} & \cdots & \phi_{nn} \end{bmatrix} \tag{5.33}$$

is called a fundamental matrix of the homogeneous system $\dot{\underset{\sim}{x}} = A(t)\underset{\sim}{x}$.

Theorem 5.1:

The solution of the homogeneous system $\dot{\underset{\sim}{x}} = A(t)\underset{\sim}{x}$ *with initial conditions* $\underset{\sim}{x}(t_0) = \underset{\sim}{x}_0$ *is given by* $\underset{\sim}{x}(t) = \Phi(t)\Phi^{-1}(t_0)\underset{\sim}{x}_0$, *where* Φ *is any fundamental matrix of the system.*

Theorem 5.2: (Floquet's theorem)

The regular system $\dot{x} = A(t)x$, *where* $A(t)$ *is an* $n \times n$ *matrix with minimal period* T, *has at least one non-trivial solution* $\underset{\sim}{x} = \underset{\sim}{\chi}(t)$ *such that*

$$\underset{\sim}{\chi}(t+T)=\mu\,\underset{\sim}{\chi}(t) \qquad \forall t\in\mathbb{R} \tag{5.34}$$

where μ *is a constant.*

Definition 5.2:

The constants μ *in Theorem 5.2 are the eigenvalues of matrix* E*, defined as* $E=\Phi^{-1}(t_0)\Phi(t_0+T)$*, are called characteristic numbers or multipliers of the equation* $\dot{\underset{\sim}{x}}=A(t)\underset{\sim}{x}$.

Theorem 5.3:

The constants μ *in Theorem 5.2 are independent of the choice of* Φ.

Definition 5.3:

A solution of the equation $\dot{\underset{\sim}{x}}=A(t)\underset{\sim}{x}$ *satisfying (5.34) is called a normal solution.*

Definition 5.4: (Characteristic exponent)

Let μ *be a characteristic number of equation* $\dot{\underset{\sim}{x}}=A(t)\underset{\sim}{x}$ *corresponding to the minimal period* T *of* $A(t)$*. Then* ρ*, defined by*

$$e^{\rho T}=\mu \tag{5.35}$$

is called the characteristic exponent of the system. Note that ρ *is defined only to within an additive multiple of* $2\pi i/T$*. It will be fixed by requiring* $-\pi<\mathrm{Im}(\rho T)\le\pi$*, or by* $\rho=\ln(\mu)/T$*, where the principal value of the logarithm is taken.*

Theorem 5.4:

Suppose that matrix E of Definition 5.2 has n distinct eigenvalues μ_i, for $i = 1, 2, ..., n$. Then the equation $\dot{\underset{\sim}{x}} = A(t)\underset{\sim}{x}$ has n linearly independent normal solutions of the form

$$\underset{\sim}{x}_i = \underset{\sim}{p}_i(t)e^{\rho_i T} \tag{5.36}$$

where the ρ_i are the characteristic exponents corresponding to μ_i, and the $\underset{\sim}{p}_i(t)$ are functions with period T.

Equations (5.25) and (5.32) are particular examples of a general *n*-dimensional first-order systems

$$\dot{\underset{\sim}{x}} = P(t)\underset{\sim}{x} \qquad \text{with } \underset{\sim}{x} \in \mathbb{R}^n,\ P(t) \in \mathbb{R}^{n\times n} \tag{5.37}$$

where $P(t)$ is periodic with minimal period $T = 2\pi/R$, that is

$$P(t+T) = P(t) \qquad \forall t \in \mathbb{R} \tag{5.38}$$

The systems of equations (5.25) and (5.32) can be time simulated for a variety of frequency ratios R, and dither amplitudes α in the case of normal dither, and over a time interval with duration $T = 2\pi/R$, i.e. $[t_0, t_0 + T]$, $\forall t_0 \in \mathbb{R}$. For a $n \times n$ matrix P, n different initial conditions must be used. In this study, the n Cartesian axes vectors are used. Using the set of Theorems 5.1-5.4, the stability can be inferred from the sign of the characteristic exponents ρ_i, *for* $i = 1, 2, ..., n$. If all characteristic exponents have negative real parts, then the Floquet multipliers μ_i have magnitude less than one. Thus using Theorem 5.2, it can be shown that the system response is a contracting mapping, and the system response only gets smaller with time. On the other hand, when there is at

least one positive characteristic exponent, the corresponding Floquet multiplier has magnitude greater than one, and the system response grows as time increases. Figure 5.6 depicts typical responses of a single degree of freedom system in cases where the characteristic exponent is positive, zero, and negative.

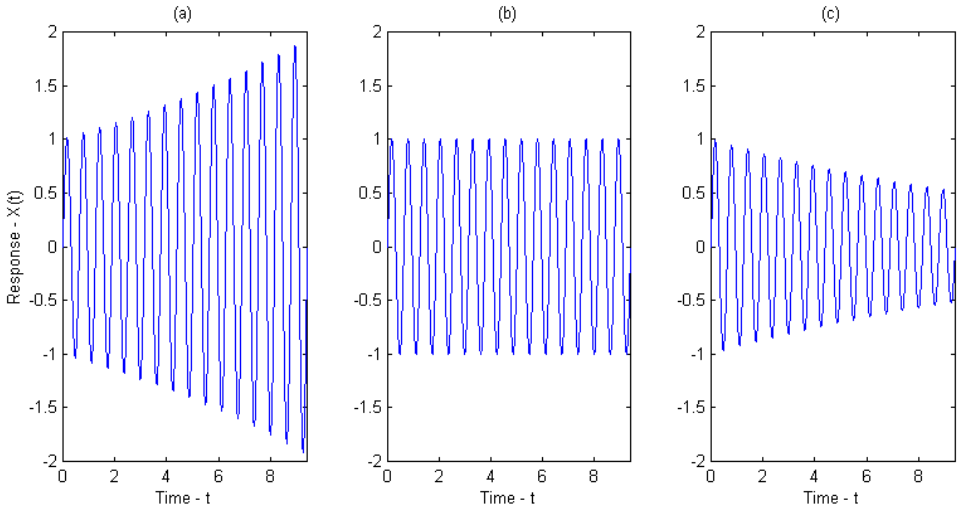

Figure 5.6: Typical SDOF system responses, (a) $Re(\rho_i)>0$, (b) $Re(\rho_i)=0$, and (c) $Re(\rho_i)<0$.

The stability for the system without dither determined numerically using Floquet theory is in strong agreement with the eigenvalue analysis described in the previous section. The downside of the Floquet method is that it is computationally very intensive compared to the eigenvalue analysis.

Multiple Scales Method

When the parameters of the rotating spring-mass-damper system are very small, the method of multiple scales may be used to approximate the solution. Therefore the mass, damping, stiffness and friction are assumed very small in this section.

The multiple scales method is used to assess the effects on system stability of both normal and tangential dither signals. Finally, the special case of tangential dither excitation in the presence of a high amplitude friction force is discussed.

Normal Dither Excitation

The development in this section will be made for the case of normal dither, as it is a more restrictive case. Results for tangential dither will then be easily derived from that analysis. It will be shown that the instabilities at subcritical rotation rates are caused by interactions of various disc modes. To show this, it is much easier for the derivation to start with a complex form of the modal expansion:

$$w(r,\theta,t)=\sum_{k=1}^{N_r}\sum_{l=-N_\theta}^{N_\theta} R_{kl}(r)\exp(il\theta)\,q_{kl}(t) \tag{5.39}$$

where the $q_{kl}(t)$ are now complex. As with the real-valued modal expansion, it is possible to normalize the eigenfunctions and to demonstrate their orthogonality.

Substitution of (5.22) into (5.1) yields

$$\begin{aligned}\left(\rho h\frac{\partial^2}{\partial t^2}+D\nabla^4\right)w(r,\theta,t)&=-\delta(\theta-\tilde{\Omega}t)\frac{\delta(r-r_0)}{r}\\ &\times\left[m\left(\frac{\partial}{\partial t}+\tilde{\Omega}\frac{\partial}{\partial\theta}\right)^2+c\left(\frac{\partial}{\partial t}+\tilde{\Omega}\frac{\partial}{\partial\theta}\right)+k-\frac{F_\theta}{r}\left(1+\alpha e^{i\omega t}+\alpha^* e^{-i\omega t}\right)\frac{\partial}{\partial\theta}\right]w(r,\theta,t)\end{aligned} \tag{5.40}$$

When the expansion (5.39) is substituted into (5.40) and orthogonality of the eigenfunctions is invoked, a set of linear ordinary differential equations in time is obtained

$$\ddot{q}_{kl}+\omega_{kl}^2 q_{kl}=-\sum_{r=1}^{N_r}\sum_{s=-N_\theta}^{N_\theta} R_{kl}(r_0)R_{rs}(r_0)\exp\left[i\left(s-l\right)\tilde{\Omega}t\right]$$
$$\times\left[m\left(\ddot{q}_{rs}+i2s\tilde{\Omega}\dot{q}_{rs}-s^2\tilde{\Omega}^2 q_{rs}\right)+c\left(\dot{q}_{rs}+is\tilde{\Omega}q_{rs}\right)\right. \tag{5.41}$$
$$\left.+\left(k-i\frac{sF_\theta}{r_0}\left(1+\alpha e^{i\omega t}+\alpha^* e^{-i\omega t}\right)\right)q_{rs}\right]$$

The following new variables, as defined in [51], are introduced

$$\varepsilon\gamma=m,\quad \varepsilon\zeta=\frac{c}{\omega_{cr}},\quad \varepsilon\kappa=\frac{k}{\omega_{cr}^2},\quad \varepsilon f=\frac{F_\theta}{\omega_{cr}^2 r_0} \tag{5.42}$$

The ε is used to remind the reader that the quantities are assumed very small, which will be referred to as order $O(\varepsilon)$ quantities. Using (5.16) and (5.42), the differential equation can be written as

$$\frac{d^2 q_{kl}}{d\tau^2}+\beta_{kl}^2 q_{kl}=-\varepsilon\sum_{r=1}^{N_r}\sum_{s=-N_\theta}^{N_\theta} R_{kl}(r_0)R_{rs}(r_0)\exp\left[i\left(s-l\right)\Omega\tau\right]$$
$$\times\left[\gamma\left(\frac{d}{d\tau}+is\Omega\right)^2+\zeta\left(\frac{d}{d\tau}+is\Omega\right)+\kappa-isf\left(1+\alpha e^{iR\tau}+\alpha^* e^{-iR\tau}\right)\right]q_{rs} \tag{5.43}$$

Following the standard procedure outlined by Nayfeh and Mook [52], new independent variables, or time scales, are introduced in terms of integer powers of ε

$$T_n=\varepsilon^n\tau \quad for\ n=0,1,2,... \tag{5.44}$$

The derivatives with respect to τ become expansions of partial derivatives with respect to the T_n according to

$$\frac{d}{d\tau}=\frac{dT_0}{d\tau}\frac{\partial}{\partial T_0}+\frac{dT_1}{d\tau}\frac{\partial}{\partial T_1}+...=D_0+\varepsilon D_1+\varepsilon^2 D_2+... \tag{5.45a}$$

$$\frac{d^2}{d\tau^2}=D_0^2+\varepsilon\left(2D_0D_1\right)+\varepsilon^2\left(D_1^2+2D_0D_2\right)+... \tag{5.45b}$$

One assumes that the solution of equation (5.43) can be represented by the following expansion

$$q_{kl}=q_{kl}^{(0)}\left(T_0,T_1,T_2,...\right)+\varepsilon q_{kl}^{(1)}\left(T_0,T_1,T_2,...\right)+\varepsilon^2 q_{kl}^{(2)}\left(T_0,T_1,T_2,...\right)+... \tag{5.46}$$

Substituting (5.45) and (5.46) into (5.43) and equating the coefficients of orders $O(1)$, and $O(\varepsilon)$ to zero yields:

$$\left(D_0^2+\beta_{kl}^2\right)q_{kl}^{(0)}=0 \tag{5.47}$$

$$\begin{aligned}\left(D_0^2+\beta_{kl}^2\right)q_{kl}^{(1)}=&-\left(2D_0D_1\right)q_{kl}^{(0)}-\sum_{r=1}^{N_r}\sum_{s=-N_\theta}^{N_\theta}R_{kl}(r_0)R_{rs}(r_0)\exp\left[i\left(s-l\right)\Omega T_0\right]\\&\times\left[\gamma\left(D_0+is\Omega\right)^2+\zeta\left(D_0+is\Omega\right)+\kappa-isf\left(1+\alpha e^{iRT_0}+\alpha^* e^{-iRT_0}\right)\right]q_{rs}^{(0)}\end{aligned} \tag{5.48}$$

The solution of (5.47) can be written in the form

$$q_{kl}^{(0)}=A_{kl}\left(T_1,T_2\right)\exp\left(i\beta_{kl}T_0\right)+B_{kl}\left(T_1,T_2\right)\exp\left(-i\beta_{kl}T_0\right) \tag{5.49}$$

where A_{kl} and B_{kl} are unknown complex functions, depending on the other time scales $T_n,\ for\ n=1,2,...$

Substituting (5.49) into (5.48) leads to

$$\begin{aligned}\left(D_0^2+\beta_{kl}^2\right)q_{kl}^{(1)} &= -2D_0D_1\left(A_{kl}\exp\left(i\beta_{kl}T_0\right)+B_{kl}\exp\left(-i\beta_{kl}T_0\right)\right)\\ &\quad -\sum_{r=1}^{N_r}\sum_{s=-N_\theta}^{N_\theta}R_{kl}(r_0)R_{rs}(r_0)\exp\left[i\left(s-l\right)\Omega T_0\right]\\ &\quad \times\Big[\gamma\left(D_0+is\Omega\right)^2+\zeta\left(D_0+is\Omega\right)\\ &\quad\quad +\kappa-isf\left(1+\alpha e^{iRT_0}+\alpha^* e^{-iRT_0}\right)\Big]\\ &\quad \times\left(A_{rs}\exp\left(i\beta_{rs}T_0\right)+B_{rs}\exp\left(-i\beta_{rs}T_0\right)\right)\end{aligned} \tag{5.50}$$

This latter equation can be rearranged in the form

$$\begin{aligned}\left(D_0^2+\beta_{kl}^2\right)q_{kl}^{(1)} &= -2i\beta_{kl}D_1\left(A_{kl}e^{i\beta_{kl}T_0}-B_{kl}e^{-i\beta_{kl}T_0}\right)\\ &\quad -\sum_{r=1}^{N_r}\sum_{s=-N_\theta}^{N_\theta}R_{kl}(r_0)R_{rs}(r_0)e^{i(s-l)\Omega T_0}\left(D_{rs}^{+}A_{rs}e^{i\beta_{rs}T_0}+D_{rs}^{-}B_{rs}e^{-i\beta_{rs}T_0}\right)\\ &\quad +\sum_{r=1}^{N_r}\sum_{s=-N_\theta}^{N_\theta}R_{kl}(r_0)R_{rs}(r_0)e^{i(s-l)\Omega T_0}\left(isf\alpha\right)\left(A_{rs}e^{i(\beta_{rs}+R)T_0}+B_{rs}e^{-i(\beta_{rs}-R)T_0}\right)\\ &\quad +\sum_{r=1}^{N_r}\sum_{s=-N_\theta}^{N_\theta}R_{kl}(r_0)R_{rs}(r_0)e^{i(s-l)\Omega T_0}\left(isf\alpha^*\right)\left(A_{rs}e^{i(\beta_{rs}-R)T_0}+B_{rs}e^{-i(\beta_{rs}+R)T_0}\right)\end{aligned} \tag{5.51}$$

where

$$\begin{aligned}D_{rs}^{+} &= \kappa-\gamma\left(C_{rs}^{+}\right)^2+i\left[\zeta C_{rs}^{+}-sf\right] \qquad C_{rs}^{+}=\beta_{rs}+s\Omega\\ D_{rs}^{-} &= \kappa-\gamma\left(C_{rs}^{-}\right)^2-i\left[\zeta C_{rs}^{-}+sf\right] \qquad C_{rs}^{-}=\beta_{rs}-s\Omega\end{aligned} \tag{5.52}$$

Tangential Dither Excitation

Equations (5.51) and (5.52) can be adapted to the case of tangential dither. The term $f\left(1+\alpha e^{iR\tau}+\alpha^* e^{-iR\tau}\right)$ in equation (5.43) is replaced with $\left(fe^{iR\tau}+f^* e^{-iR\tau}\right)$. This procedure yields:

$$
\begin{aligned}
\left(D_0^2+\beta_{kl}^2\right)q_{kl}^{(1)} &= -2i\beta_{kl}D_1\left(A_{kl}e^{i\beta_{kl}T_0}-B_{kl}e^{-i\beta_{kl}T_0}\right)\\
&-\sum_{r=1}^{N_r}\sum_{s=-N_\theta}^{N_\theta}R_{kl}(r_0)R_{rs}(r_0)e^{i(s-l)\Omega T_0}\left(D_{rs}^{+}A_{rs}e^{i\beta_{rs}T_0}+D_{rs}^{-}B_{rs}e^{-i\beta_{rs}T_0}\right)\\
&+\sum_{r=1}^{N_r}\sum_{s=-N_\theta}^{N_\theta}isf\,R_{kl}(r_0)R_{rs}(r_0)e^{i\left[(s-l)\Omega+R\right]T_0}\left(A_{rs}e^{i\beta_{rs}T_0}+B_{rs}e^{-i\beta_{rs}T_0}\right)\\
&+\sum_{r=1}^{N_r}\sum_{s=-N_\theta}^{N_\theta}isf^{*}R_{kl}(r_0)R_{rs}(r_0)e^{i\left[(s-l)\Omega-R\right]T_0}\left(A_{rs}e^{i\beta_{rs}T_0}+B_{rs}e^{-i\beta_{rs}T_0}\right)
\end{aligned}
\tag{5.53}
$$

where

$$
\begin{aligned}
D_{rs}^{+} &= \kappa-\gamma\left(C_{rs}^{+}\right)^2+i\zeta C_{rs}^{+} \qquad C_{rs}^{+}=\beta_{rs}+s\Omega\\
D_{rs}^{-} &= \kappa-\gamma\left(C_{rs}^{-}\right)^2-i\zeta C_{rs}^{-} \qquad C_{rs}^{-}=\beta_{rs}-s\Omega
\end{aligned}
\tag{5.54}
$$

Effect of Normal and Tangential Dither on Stability

Following the methodology used by Shen [53], it is found that *single-mode resonances* will occur at rotation speeds close to

$$2l\Omega = 2\beta_{kl} \qquad for\ l>0 \tag{5.55a}$$

$$2l\Omega = \pm\beta_{kl}\pm\beta_{kl}\pm R \qquad for\ l>0,\ R>0 \tag{5.55b}$$

and that *combination-mode resonances* will occur at rotation speeds close to

$$(s\pm l)\Omega = \beta_{rs}\pm\beta_{kl} \qquad for\ s>l,\ l\geq 0 \tag{5.56a}$$

$$(s\pm l)\Omega = \pm\beta_{rs}\pm\beta_{kl}\pm R \qquad for\ s>l,\ l\geq 0,\ R>0 \tag{5.56b}$$

It is seen that neither normal nor tangential dither can suppress the system parametric resonances induced by the rotating spring-mass-damper system, given by conditions (5.55a) and (5.56a). In other words, R has no effect on these resonances. Furthermore

both normal and tangential type dither forces have a destabilizing effect on the system by adding additional instability bands at rotation speeds given by conditions (5.55b) and (5.56b).

Special Case of High Amplitude Friction Force

The special case of high amplitude friction force is considered in this section. The amplitude is chosen such that

$$\frac{F_\theta}{\omega_{cr}^2 r_0} = O\left(\sqrt{\varepsilon}\right) \tag{5.57}$$

Therefore the system parameters used in (5.42) can be rewritten as

$$\varepsilon\gamma = m, \quad \varepsilon\zeta = \frac{c}{\omega_{cr}}, \quad \varepsilon\kappa = \frac{k}{\omega_{cr}^2}, \quad \varepsilon^{\frac{1}{2}} f = \frac{F_\theta}{\omega_{cr}^2 r_0} \tag{5.58}$$

New time scales are introduced as multiples of half-integer powers of ε

$$T_n^{'} = \varepsilon^{\frac{n}{2}}\tau \quad for\ n = 0,1,2,... \tag{5.59}$$

The derivatives with respect to τ become expansions of partial derivatives with respect to the $T_n^{'}$ according to

$$\frac{d}{d\tau} = \frac{dT_0^{'}}{d\tau}\frac{\partial}{\partial T_0^{'}} + \frac{dT_1^{'}}{d\tau}\frac{\partial}{\partial T_1^{'}} + ... = D_0^{'} + \varepsilon^{\frac{1}{2}} D_1^{'} + \varepsilon D_2^{'} + ... \tag{5.60a}$$

$$\frac{d^2}{d\tau^2} = D_0^{'2} + \varepsilon^{\frac{1}{2}}\left(2D_0^{'}D_1^{'}\right) + \varepsilon\left(D_1^{'2} + 2D_0^{'}D_2^{'}\right) + ... \tag{5.60b}$$

One assumes that the solution of equation (5.43) can be represented by the following expansion

$$q_{kl} = q_{kl}^{(0)}\left(T_0^{'}, T_1^{'}, T_2^{'}, \ldots\right) + \varepsilon^{\frac{1}{2}} q_{kl}^{(1)}\left(T_0^{'}, T_1^{'}, T_2^{'}, \ldots\right) + \varepsilon q_{kl}^{(2)}\left(T_0^{'}, T_1^{'}, T_2^{'}, \ldots\right) + \ldots \tag{5.61}$$

Equation (5.43) can be adapted to the case of tangential dither excitation as follows

$$\begin{aligned} \frac{d^2 q_{kl}}{d\tau^2} + \beta_{kl}^2 q_{kl} = -\sum_{r=1}^{N_r} \sum_{s=-N_\theta}^{N_\theta} & R_{kl}(r_0) R_{rs}(r_0) \exp\left[i(s-l)\Omega\tau\right] \\ & \times \left[\varepsilon^{\frac{1}{2}} f\left(-ise^{iR\tau}\right) + \varepsilon^{\frac{1}{2}} f^*\left(-ise^{-iR\tau}\right)\right. \\ & \left. + \varepsilon\gamma\left(\frac{d}{d\tau} + is\Omega\right)^2 + \varepsilon\zeta\left(\frac{d}{d\tau} + is\Omega\right) + \varepsilon\kappa\right] q_{rs} \end{aligned} \tag{5.62}$$

Substituting (5.60) and (5.61) into (5.62) and equating the coefficients of orders $O(1)$, and $O\left(\varepsilon^{\frac{1}{2}}\right)$ to zero

$$\left(D_0^{'2} + \beta_{kl}^2\right) q_{kl}^{(0)} = 0 \tag{5.63}$$

$$\begin{aligned} \left(D_0^{'2} + \beta_{kl}^2\right) q_{kl}^{(1)} = & -2 D_0^{'} D_1^{'} q_{kl}^{(0)} \\ & + \sum_{r=1}^{N_r} \sum_{s=-N_\theta}^{N_\theta} isf\, R_{kl}(r_0) R_{rs}(r_0) e^{i\left[(s-l)\Omega + R\right]T_0^{'}} q_{rs}^{(0)} \\ & + \sum_{r=1}^{N_r} \sum_{s=-N_\theta}^{N_\theta} isf^*\, R_{kl}(r_0) R_{rs}(r_0) e^{i\left[(s-l)\Omega - R\right]T_0^{'}} q_{rs}^{(0)} \end{aligned} \tag{5.64}$$

Equation (5.63) is the same as equation (5.47); therefore the solution for the order $O(1)$ is also of the form (5.49), i.e.

$$q_{kl}^{(0)} = A_{kl}\left(T_1^{'}, T_2^{'}\right)\exp\left(i\beta_{kl} T_0^{'}\right) + B_{kl}\left(T_1^{'}, T_2^{'}\right)\exp\left(-i\beta_{kl} T_0^{'}\right) \tag{5.65}$$

where A_{kl} and B_{kl} are unknown complex functions, depending on the other time scales $T_n^{'},\ for\ n = 1, 2, \ldots$

Substituting (5.65) into (5.64) leads to

$$\left(D_0^{'2}+\beta_{kl}^2\right)q_{kl}^{(1)}=-2i\beta_{kl}D_1^{'}\left(A_{kl}e^{i\beta_{kl}T_0^{'}}-B_{kl}e^{-i\beta_{kl}T_0^{'}}\right)$$
$$+\sum_{r=1}^{N_r}\sum_{s=-N_\theta}^{N_\theta} isf\ R_{kl}(r_0)R_{rs}(r_0)e^{i\left[(s-l)\Omega+R\right]T_0^{'}}\left(A_{rs}e^{i\beta_{rs}T_0^{'}}+B_{rs}e^{-i\beta_{rs}T_0^{'}}\right) \qquad (5.66)$$
$$+\sum_{r=1}^{N_r}\sum_{s=-N_\theta}^{N_\theta} isf^{*}R_{kl}(r_0)R_{rs}(r_0)e^{i\left[(s-l)\Omega-R\right]T_0^{'}}\left(A_{rs}e^{i\beta_{rs}T_0^{'}}+B_{rs}e^{-i\beta_{rs}T_0^{'}}\right)$$

Following the methodology used by Shen [53], equation (5.66) shows that tangential dither will suppress the initial parametric resonances occurring at rotation speeds given by (5.55a) and (5.56a), but will induce additional resonances at rotation speeds given by (5.55b) and (5.56b).

Numerical Results

The stability for the system without dither has been assessed calculating the eigenvalues of (5.21), whereas the system with dither has been determined numerically using Floquet theory. The scaled rotation speeds that have been considered in the numerical simulations are exclusively subcritical, i.e. $0<\Omega\leq 1$, as this range is the most relevant to many engineering problems like brake systems.

The undithered system exhibits resonances induced by the rotating SMD. They occur at scaled rotation speeds denoted by Ω_i, given in table 5.1, and obtained using equations (5.55a) and (5.56a). Additional resonances are induced by dither excitation. They occur at scaled rotation speeds denoted by Ω_i^{*}, given in table 5.2, and obtained using equations (5.55b) and (5.56b).

Table 5.1: System scaled rotation speeds. Parameters: h/a=0.01, b/a=0.05, N_r=1, N_θ=2.

Ω_1	Ω_2	Ω_3	Ω_4	Ω_5
0.036	0.064	0.114	0.192	1

Table 5.2: Dither induced scaled rotation speeds. Parameters: h/a=0.01, b/a=0.05, N_r=1, N_θ=2, R=2.7.

Ω_1^*	Ω_2^*	Ω_3^*	Ω_4^*	Ω_5^*	Ω_6^*	Ω_7^*	Ω_8^*
0.325	0.369	0.458	0.536	0.675	0.836	0.879	0.964

Normal Dither Excitation

Figures 5.7 and 5.8 show the stability maps for a given set of system parameters with and without normal dither, for no plate damping and modal damping $\xi=10^{-3}$, respectively. The initial parametric resonances Ω_i induced by the SMD system are still present in the dithered system. However normal dither seems to stabilize the system over a very small range of friction parameter values near rotation speeds $\Omega = 0.7$ and $\Omega = 0.88$. But overall, it is seen that normal dither is not capable to suppress the system unstable region. The importance of plate damping in stabilizing the system is also clearly evident.

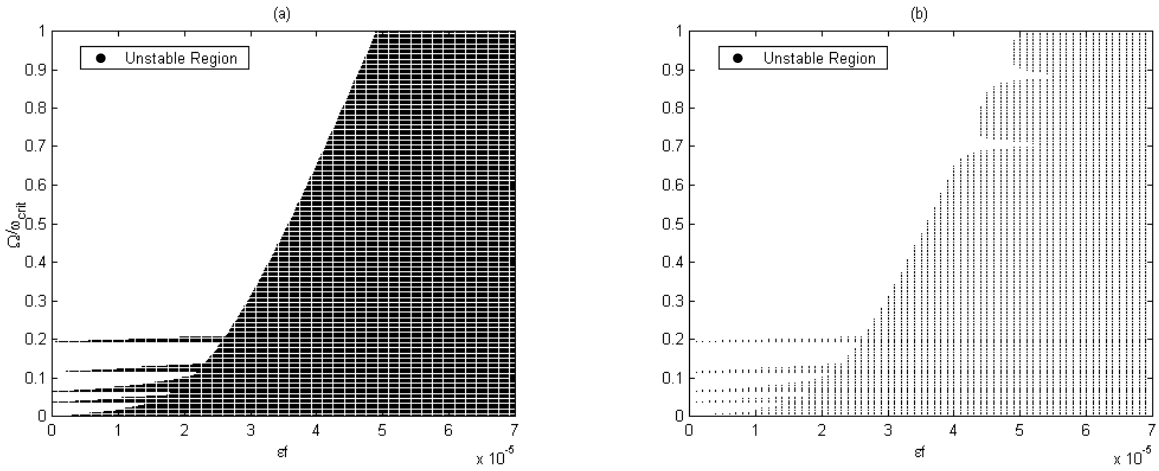

Figure 5.7: Stability map as a function of scaled rotational speed Ω and scaled friction force $\varepsilon f=F_\theta/r_0\omega^2_{crit}$ for a system with normal dither. Parameters: h/a=0.01, b/a=0.05, r_0/a=0.5, $\varepsilon\gamma$=0.3, $\varepsilon\varsigma$=0.3, $\varepsilon\kappa$=0.3, N_r=1, N_θ=2, ξ=0, (a) α=0, and (b) α=1, R=2.7

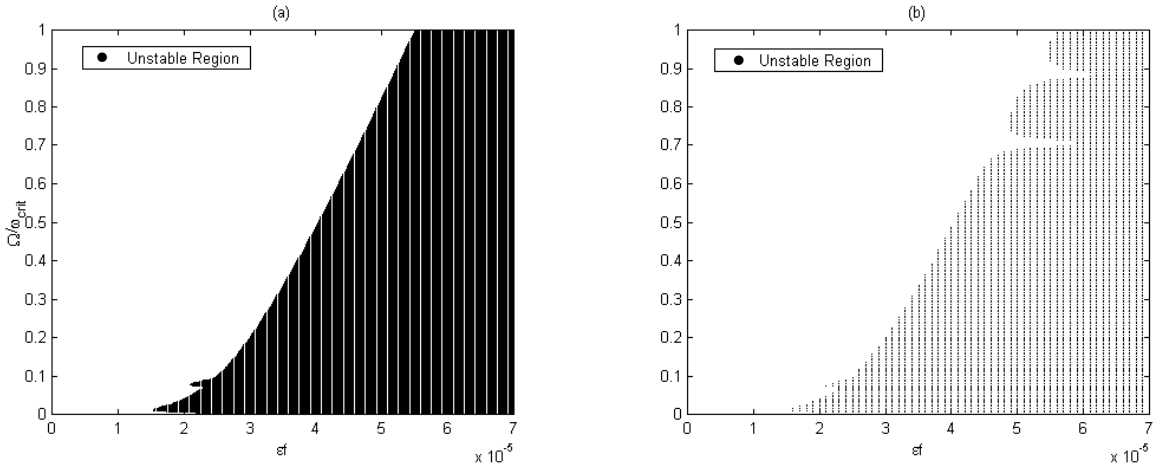

Figure 5.8: Stability map as a function of scaled rotational speed Ω and scaled friction force $\varepsilon f=F_\theta/r_0\omega^2_{crit}$ for a system with normal dither. Parameters: h/a=0.01, b/a=0.05, r_0/a=0.5, $\varepsilon\gamma$=0.3, $\varepsilon\varsigma$=0.3, $\varepsilon\kappa$=0.3, N_r=1, N_θ=2, $\xi=10^{-3}$, (a) α=0, and (b) α=1, R=2.7

Tangential Dither Excitation

Figures 5.9–5.11 show the stability maps for a given set of system parameters with and without tangential dither, for no plate damping and a variety of SMD parameters $(\varepsilon\gamma,\ \varepsilon\varsigma\ and\ \varepsilon\kappa)$ ranging from 0.1 to 0.3.

The stability maps of the undithered system are depicted in the left plots of Figures 5.9–5.11. The initial parametric resonances induced by the SMD system, listed in Table 5.1, are present in the undithered system, as predicted by equations (5.55a) and (5.56a). Also, note that the system is unstable for all rotation speeds when $\varepsilon f \geq 2\times10^{-5}$ for $\varepsilon\gamma = \varepsilon\varsigma = \varepsilon\kappa = 0.1$, when $\varepsilon f \geq 3.5\times10^{-5}$ for $\varepsilon\gamma = \varepsilon\varsigma = \varepsilon\kappa = 0.2$, and when $\varepsilon f \geq 5\times10^{-5}$ for $\varepsilon\gamma = \varepsilon\varsigma = \varepsilon\kappa = 0.3$.

The stability maps of the system excited with tangential dither of amplitude $\alpha = 1$ and frequency ratio $R = 2.7$ are depicted in the right plots of Figures 5.9–5.11. The initial parametric resonances induced by the SMD system are still present in the dithered system, but they occur only when friction reaches a high value, i.e. when $\varepsilon f \simeq 1\times10^{-4}$ for Ω_1 and $\varepsilon f \simeq 3\times10^{-5}$ for Ω_4. Moreover these instability bands, associated with the scaled rotation speeds Ω_i, are very narrow. As predicted by equations (5.55b) and (5.56b), additional resonances are induced by dither excitation. As can be seen in the right plots of Figures 5.9–5.11, they occur at scaled rotation speeds Ω_1^*, Ω_2^*, and Ω_3^*. The instability band associated with the rotation speed Ω_4^* is also present in Figure 5.9 in the case $\varepsilon\gamma = \varepsilon\varsigma = \varepsilon\kappa = 0.1$. Therefore, it can be concluded that tangential dither can substantially reduce the parametric resonances induced by the SMD system, but leads to additional resonances at different rotation speeds.

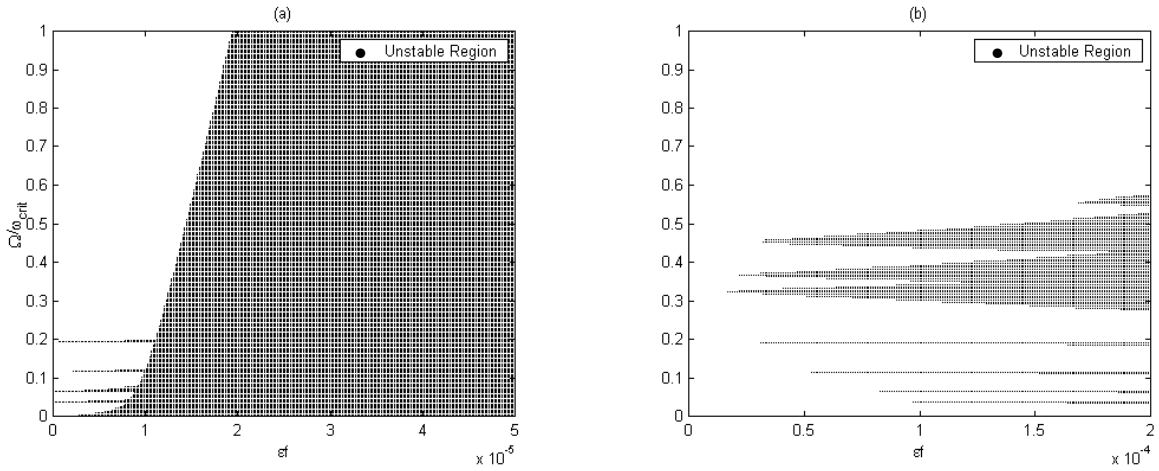

Figure 5.9: Stability map as a function of scaled rotational speed Ω and scaled friction force $\varepsilon f=F_\theta/r_0\omega^2_{crit}$ for a system with tangential dither. Parameters: h/a=0.01, b/a=0.05, $r_0/a=0.5$, $\varepsilon\gamma=0.1$, $\varepsilon\varsigma=0.1$, $\varepsilon\kappa=0.1$, $N_r=1$, $N_\theta=2$, $\xi=0$, (a) $\alpha=0$, and (b) $\alpha=1$, R=2.7

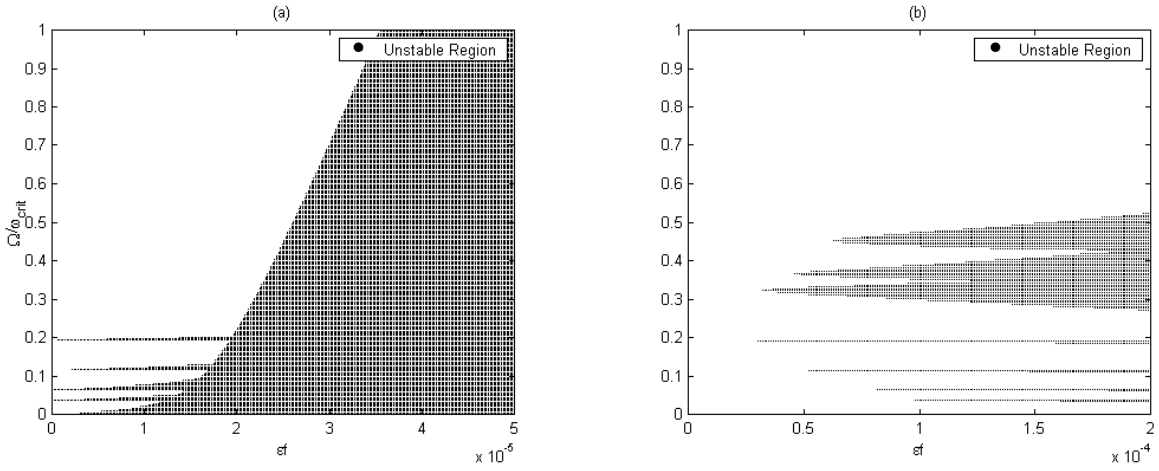

Figure 5.10: Stability map as a function of scaled rotational speed Ω and scaled friction force $\varepsilon f=F_\theta/r_0\omega^2_{crit}$ for a system with tangential dither. Parameters: h/a=0.01, b/a=0.05, $r_0/a=0.5$, $\varepsilon\gamma=0.2$, $\varepsilon\varsigma=0.2$, $\varepsilon\kappa=0.2$, $N_r=1$, $N_\theta=2$, $\xi=0$, (a) $\alpha=0$, and (b) $\alpha=1$, R=2.7

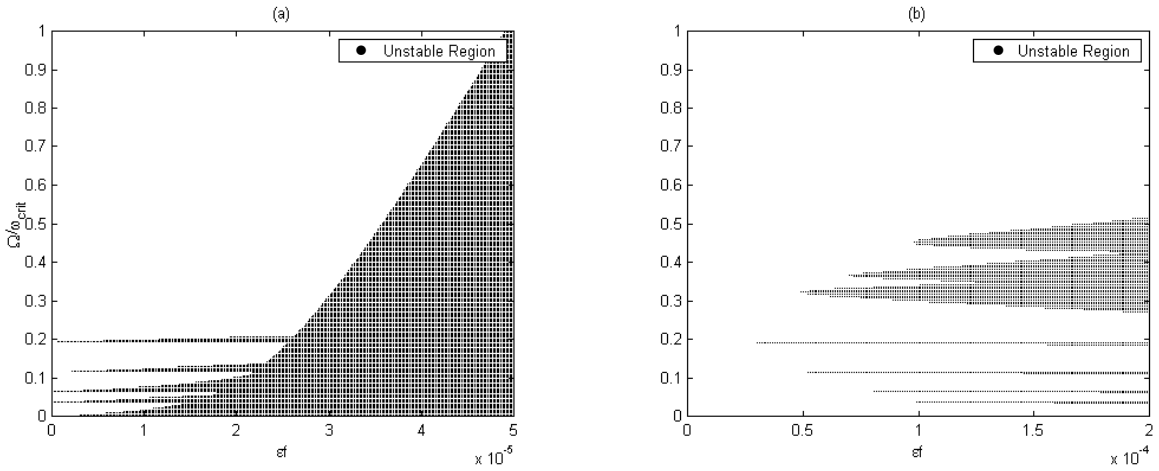

Figure 5.11: Stability map as a function of scaled rotational speed Ω and scaled friction force $\varepsilon f=F_\theta/r_0\omega^2_{crit}$ for a system with tangential dither. Parameters: h/a=0.01, b/a=0.05, $r_0/a=0.5$, $\varepsilon\gamma=0.3$, $\varepsilon\varsigma=0.3$, $\varepsilon\kappa=0.3$, $N_r=1$, $N_\theta=2$, $\xi=0$, (a) $\alpha=0$, and (b) $\alpha=1$, R=2.7

Figures 5.12–5.15 show the stability maps for a given set of system parameters with and without tangential dither, for $\varepsilon\gamma=\varepsilon\varsigma=\varepsilon\kappa=0.3$ and a variety of plate modal damping ranging from $\xi=0$ to $\xi=10^{-3}$.

The stability maps of the undithered system are depicted in the left plots of Figures 5.12–5.15. All the initial parametric resonances induced by the SMD system are present in the undithered system with light damping, i.e. $\xi=0$ and $\xi=10^{-5}$, as predicted by equations (5.55a) and (5.56a) and listed in Table 5.1. When the plate modal damping is increased to $\xi=10^{-4}$, only instabilities associated with rotation speeds Ω_2 and Ω_3 are remaining, as seen in Figure 5.14. The instability associated with only the rotation speed Ω_2 is left when the plate modal damping is increased up to $\xi=10^{-3}$, as seen in Figure 5.15.

The stability maps of the system excited with tangential dither of amplitude $\alpha=1$ and frequency ratio $R=2.7$ are depicted in the right plots of Figures 5.12–5.15. The

initial parametric resonances induced by the SMD system are still present in the dithered system with no plate damping, as seen in Figure 5.12. However they occur only when friction reaches a high value, i.e. when $\varepsilon f \simeq 1\times10^{-4}$ for Ω_1 and $\varepsilon f \simeq 3\times10^{-5}$ for Ω_4.

When the plate modal damping is increased to $\xi = 10^{-5}$, only instabilities associated with rotation speeds Ω_3 (when $\varepsilon f \simeq 1.4\times10^{-4}$) and Ω_4 (when $\varepsilon f \simeq 1.8\times10^{-4}$) are remaining, as seen in Figure 5.13. When the plate modal damping is increased further, i.e. $\xi = 10^{-4}$ and $\xi = 10^{-3}$, the initial parametric resonances induced by the SMD system are completely removed from the system in the range of friction considered, i.e. for $0 \le \varepsilon f \le 2\times10^{-4}$, as seen in Figures 5.14 and 5.15. As predicted by equations (5.55b) and (5.56b), additional resonances are induced by dither excitation. As can be seen in the right plots of Figures 5.12–5.15, they occur at scaled rotation speeds Ω_1^*, Ω_2^*, and Ω_3^*. Therefore, it can be concluded that in a more realistic model including light plate modal damping tangential dither can effectively cancel the parametric resonances induced by the SMD system, but leads to additional resonances at different rotation speeds.

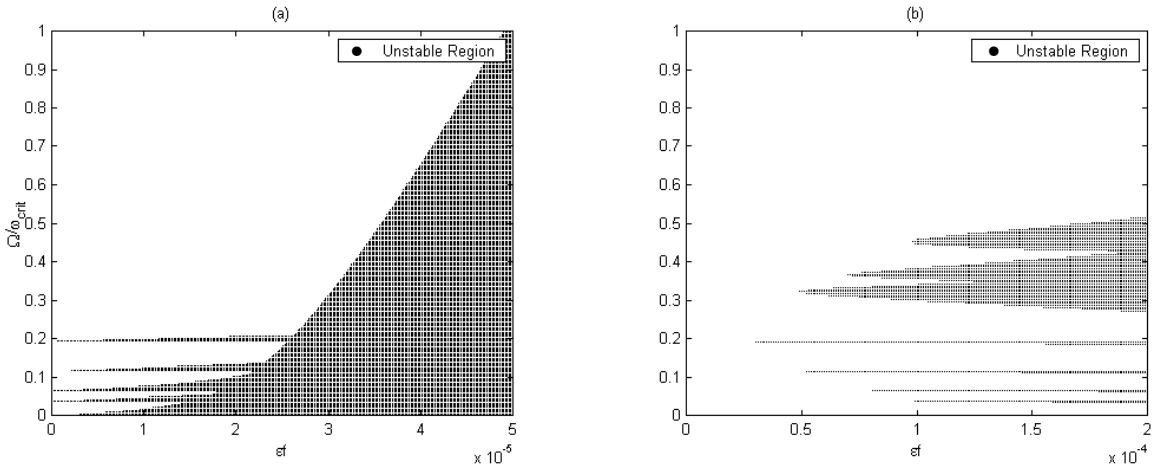

Figure 5.12: Stability map as a function of scaled rotational speed Ω and scaled friction force $\varepsilon f=F_\theta/r_0\omega^2_{crit}$ for a system with tangential dither. Parameters: h/a=0.01, b/a=0.05, $r_0/a=0.5$, $\varepsilon\gamma=0.3$, $\varepsilon\varsigma=0.3$, $\varepsilon\kappa=0.3$, $N_r=1$, $N_\theta=2$, $\xi=0$, (a) $\alpha=0$, and (b) $\alpha=1$, R=2.7

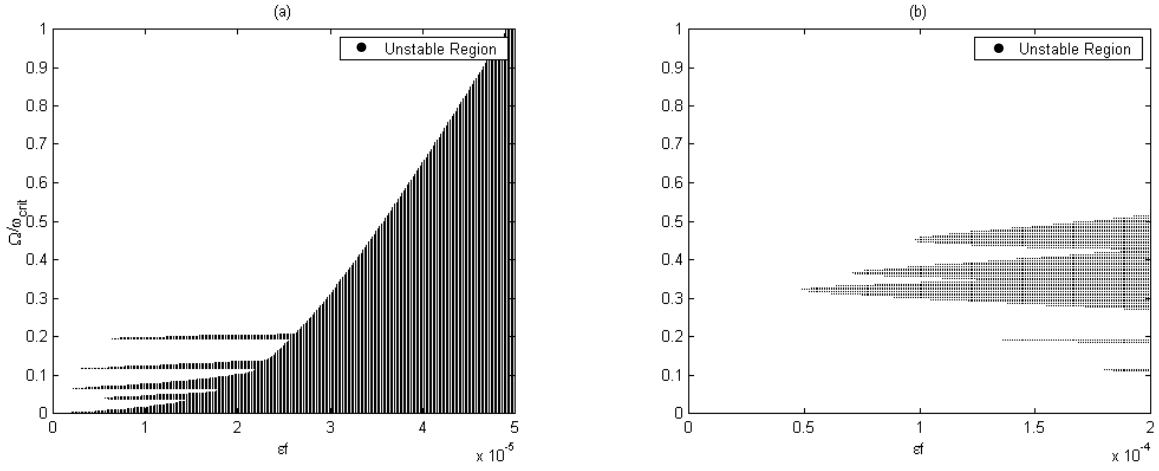

Figure 5.13: Stability map as a function of scaled rotational speed Ω and scaled friction force $\varepsilon f=F_\theta/r_0\omega^2_{crit}$ for a system with tangential dither. Parameters: h/a=0.01, b/a=0.05, $r_0/a=0.5$, $\varepsilon\gamma=0.3$, $\varepsilon\varsigma=0.3$, $\varepsilon\kappa=0.3$, $N_r=1$, $N_\theta=2$, $\xi=10^{-5}$, (a) $\alpha=0$, and (b) $\alpha=1$, R=2.7

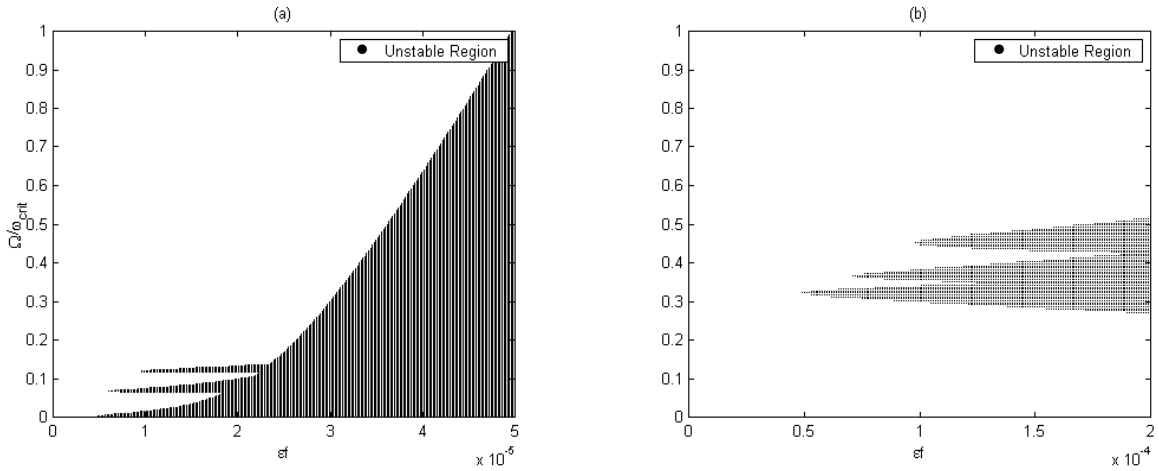

Figure 5.14: Stability map as a function of scaled rotational speed Ω and scaled friction force $\varepsilon f=F_\theta/r_0\omega^2_{crit}$ for a system with tangential dither. Parameters: h/a=0.01, b/a=0.05, r_0/a=0.5, $\varepsilon\gamma$=0.3, $\varepsilon\varsigma$=0.3, $\varepsilon\kappa$=0.3, N_r=1, N_θ=2, $\xi=10^{-4}$, (a) α=0, and (b) α=1, R=2.7

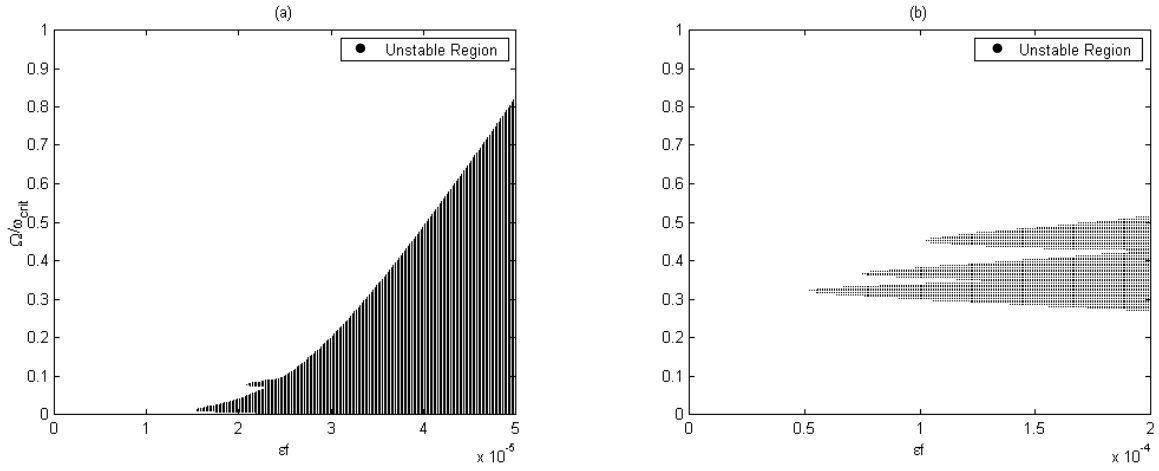

Figure 5.15: Stability map as a function of scaled rotational speed Ω and scaled friction force $\varepsilon f=F_\theta/r_0\omega^2_{crit}$ for a system with tangential dither. Parameters: h/a=0.01, b/a=0.05, r_0/a=0.5, $\varepsilon\gamma$=0.3, $\varepsilon\varsigma$=0.3, $\varepsilon\kappa$=0.3, N_r=1, N_θ=2, $\xi=10^{-3}$, (a) α=0, and (b) α=1, R=2.7

CONCLUSION

In light of the multiple scale analysis, it can be concluded that normal dither cannot suppress the system parametric resonances induced by the rotating spring-mass-damper system.

On the other hand, tangential dither can substantially reduce the parametric resonances induced by the SMD system, but leads to additional instability regions at different rotation speeds. In addition, if a more realistic model including light plate modal damping is used, tangential dither can effectively cancel the initial parametric resonances induced by the SMD system.

Numerical simulations using Floquet theory confirm the predictions made by the multiple scale analysis, for both normal and tangential dither excitations.

An important feature of the tangential dither capability to stabilize the system is that there is no constraint on the excitation frequency R. Thus, as R can be arbitrarily chosen, it can be used to cancel squeal arising at a particular rotor speed.

CHAPTER 6

CONCLUSION

The objective of this research was to study the influence of dither on self-excited frictional oscillations. More precisely, the “stick-slip” and the “mode coalescence” theories for brake squeal have been investigated.

The “stick-slip” explanation for brake squeal has been studied using the mass-on-moving-belt single degree of freedom model. Two representative friction models have been selected: the decreasing friction model that has a decreasing friction coefficient with increasing slip velocity, and the Stribeck friction that also have a decreasing friction coefficient with increasing slip velocity, but also a “lubricated” regime, where the friction force is similar to viscous friction.

SDOF WITH STRIBECK FRICTION MODEL

It is found that unstable, self-excited oscillations in the system having the Stribeck friction model can always be stabilized by applying tangential dither of sufficient amplitude. This result holds for tangential dither with sinusoidal, triangular and square waveforms. On the other hand, normal dither can stabilize the system for some system parameters, but not in general.

The effect of tangential dither with various waveforms on stability has been quantified and can be predicted using the averaging technique. The averaging technique shows that sinusoidal waveforms requires a higher dither force than square waveforms, but a lower force than triangular waveforms in order to achieve stability of an undithered unstable system, regardless of belt velocity.

The averaging technique developed for tangential dither has been extended to normal dither. A numerical procedure for computing effective friction characteristic when normal dither is injected in the system has been implemented. The effective friction characteristics obtained with the extended averaging technique are in agreement with the ones obtained with the numerical procedure. The averaging technique shows that normal dither requires a higher dither force than in the tangential dither case.

Amplitude-frequency combinations that cause the steady-state dithered response to decrease to 5% of the undithered response show a very repeatable correlation with the stability boundary predicted by the averaging technique. This result holds for tangential and normal dither with sinusoidal, triangular and square waveforms.

Numerical simulations show that, for a given dither force amplitude, triangular waveforms achieve a lower level of control than sinusoidal waveforms, and square waveforms achieve a higher level of control than sinusoidal waveforms.

SDOF WITH DECREASING FRICTION MODEL

The behavior of the system with a decreasing friction law differs from that of the system with the Stribeck friction model in one important respect. While dither is found to always be a stabilizing influence in the case of the Stribeck friction model, the system with the decreasing friction model can be either stabilized or destabilized by dither.

Both the averaging technique and numerical simulations show that a system undergoing stable, steady sliding can be destabilized by applying dither of intermediate strength. When the undithered system is unstable, it is always possible to find a tangential dither signal that stabilizes the system. These results hold for tangential dither with sinusoidal, triangular and square waveforms.

For a given belt velocity, the range of dither amplitudes that destabilizes the system is broad and within high amplitude levels for the triangular waveforms, and is narrow and within low amplitude levels for the square waveforms. The range of destabilizing dither amplitudes for sinusoidal waveforms lies between that of the triangular and the square waveforms.

When the undithered system is unstable, unlike the case of tangential dither, it is not always possible to find a normal dither signal that stabilizes the system, since the dither amplitude is limited by the requirement that the total normal force be positive.

In this case, the stability threshold predicted by the averaging technique again correlates well with the 5% performance level found using numerical integration.

CONTINUOUS PLATE MODEL

In light of the multiple scale analysis, it can be concluded that normal dither cannot suppress the system parametric resonances induced by the rotating spring-mass-damper system.

On the other hand, tangential dither can substantially reduce the parametric resonances induced by the SMD system, but leads to additional instability regions at different rotation speeds. In addition, if a more realistic model including light plate modal damping is used, tangential dither can effectively cancel the initial parametric resonances induced by the SMD system. An important feature of the tangential dither capability to stabilize the system is that there is no constraint on the excitation frequency R. Thus, as R can be arbitrarily chosen, it can be used to cancel squeal arising at a particular rotor speed.

FUTURE RESEARCH SUGGESTIONS

There is a legitimate need for experimental validations of the results obtained in this thesis. The results obtained for the SDOF model should be verified using a simple experimental setup.

The dynamics of the caliper needs to be understood in order to model the brake system more accurately. This requires measuring precisely the motion of the caliper in the brake system experimentally. This knowledge can be used to include additional modes of displacement of the contacting pads and caliper system. Thus a more refined model of the pad and caliper assembly could then be used for simulation.

The plate model represents the pad/caliper interface by a single point. A natural extension is to model the interface in a more distributed nature. Another interesting feature for the modeling of the contact interface is to allow for both sticking and slipping regions at the same time.

APPENDIX A - SINUSOIDAL WAVEFORMS

Sinusoidal waveforms can be expressed as

$$g(x)=\sin(x) \tag{A.1}$$

The integral of this signal is given by

$$G(x)=\int \sin(x)dx=-\cos(x) \tag{A.2}$$

Using equation (A.2) into (3.36b) leads to the following integral

$$\begin{aligned}&\int_0^{2\pi}\exp\left(sign(v_r)\frac{\alpha_T}{v_m}\cos(R_T\tau)\right)d(R_T\tau)\\&\quad=2\int_0^{\pi}\exp\left(sign(v_r)\frac{\alpha_T}{v_m}\cos(R_T\tau)\right)d(R_T\tau)\\&\quad=2\pi I_0\left(\frac{\alpha_T}{v_m}\right)\end{aligned} \tag{A.3}$$

where $I_0(.)$ is the modified Bessel function of order zero.

Therefore, the effective friction characteristic in the case of sinusoidal waveforms, when $|v_r|\geq\alpha_T$, can be expressed using equations (A.3) into (3.36b)

$$\bar{\mu}(v_r)=sign(v_r)\left\{\alpha_0+\alpha_1 I_0\left(\frac{\alpha_T}{v_m}\right)\exp\left(-\frac{|v_r|}{v_m}\right)\right\}\quad for\,|v_r|\geq\alpha_T \tag{A.4}$$

APPENDIX B - TRIANGULAR WAVEFORMS

Triangular waveforms can be expressed as

$$g(x)=triang(x)=\begin{cases}\dfrac{2}{\pi}x & for\ 0\le x\le\dfrac{\pi}{2}\\ 2-\dfrac{2}{\pi}x & for\ \dfrac{\pi}{2}\le x\le\dfrac{3\pi}{2}\\ -4+\dfrac{2}{\pi}x & for\ \dfrac{3\pi}{2}\le x\le 2\pi\end{cases} \tag{B.1}$$

The integral of this signal is given by

$$G(x)=\int triang(x)dx=\begin{cases}-\dfrac{\pi}{4}+\dfrac{1}{\pi}x^2 & for\ 0\le x\le\dfrac{\pi}{2}\\ \dfrac{\pi}{4}-\dfrac{1}{\pi}(x-\pi)^2 & for\ \dfrac{\pi}{2}\le x\le\dfrac{3\pi}{2}\\ -\dfrac{\pi}{4}+\dfrac{1}{\pi}(x-2\pi)^2 & for\ \dfrac{3\pi}{2}\le x\le 2\pi\end{cases} \tag{B.2}$$

Using equation (B.2) into (3.36) leads to the following integrals

$$\begin{aligned}&\int_0^{R_T\tau_1}\exp\left(\frac{v_r+\alpha_T\int triang(x)dx}{v_m}\right)d(R_T\tau)\\ &\quad=\left[\frac{\exp\left(\dfrac{v_r}{v_m}-\dfrac{\alpha_T}{v_m}\dfrac{\pi}{4}\right)\sqrt{\pi}\ erfi\left(\sqrt{\dfrac{\alpha_T}{v_m\pi}}x\right)}{2\sqrt{\dfrac{\alpha_T}{v_m\pi}}}\right]_0^{R_T\tau_1}\\ &\quad=\exp\left(\frac{v_r}{v_m}-\frac{\alpha_T}{v_m}\frac{\pi}{4}\right)\frac{\pi}{2}\sqrt{\frac{v_m}{\alpha_T}}\left[erfi\left(\sqrt{\frac{\pi\alpha_T}{4v_m}-\frac{v_r}{v_m}}\right)-erfi(0)\right]\end{aligned} \tag{B.3}$$

$$
\begin{aligned}
&\int_{R_T\tau_1}^{R_T\tau_2} \exp\left(-\frac{\nu_r+\alpha_T\int triang(x)dx}{\nu_m}\right)d\left(R_T\tau\right)\\
&=\int_{R_T\tau_1}^{\pi/2}\exp\left(-\left(\frac{\nu_r}{\nu_m}+\frac{\pi\alpha_T}{4\nu_m}\right)-\frac{\alpha_T}{\pi\nu_m}x^2\right)dx+\int_{-\pi/2}^{\pi/2}\exp\left(-\left(\frac{\nu_r}{\nu_m}+\frac{\alpha_T\pi}{4\nu_m}\right)+\frac{\alpha_T}{\pi\nu_m}x^2\right)dx\\
&\quad+\int_{-\pi/2}^{-R_T\tau_1}\exp\left(-\left(\frac{\nu_r}{\nu_m}+\frac{\pi\alpha_T}{4\nu_m}\right)-\frac{\alpha_T}{\pi\nu_m}x^2\right)dx\\
&=\left[\exp\left(-\left(\frac{\nu_r}{\nu_m}+\frac{\pi\alpha_T}{4\nu_m}\right)\right)\frac{\pi}{2}\sqrt{\frac{\nu_m}{\alpha_T}}\right]\times\left(\begin{array}{l}erf\left(\sqrt{\frac{\pi\alpha_T}{4\nu_m}}\right)+erf\left(-\sqrt{\frac{\pi\alpha_T}{4\nu_m}}-\frac{\nu_r}{\nu_m}\right)\\-erf\left(-\sqrt{\frac{\pi\alpha_T}{4\nu_m}}\right)-erf\left(\sqrt{\frac{\pi\alpha_T}{4\nu_m}}-\frac{\nu_r}{\nu_m}\right)\\+erfi\left(\sqrt{\frac{\pi\alpha_T}{4\nu_m}}\right)-erfi\left(-\sqrt{\frac{\pi\alpha_T}{4\nu_m}}\right)\end{array}\right)\\
&=\left[\exp\left(-\left(\frac{\nu_r}{\nu_m}+\frac{\pi\alpha_T}{4\nu_m}\right)\right)\pi\sqrt{\frac{\nu_m}{\alpha_T}}\right]\\
&\quad\times\left(erf\left(\sqrt{\frac{\pi\alpha_T}{4\nu_m}}\right)-erf\left(\sqrt{\frac{\pi\alpha_T}{4\nu_m}}-\frac{\nu_r}{\nu_m}\right)+erfi\left(\sqrt{\frac{\pi\alpha_T}{4\nu_m}}\right)\right)
\end{aligned}
\tag{B.4}
$$

$$
\begin{aligned}
&\int_{R_T\tau_2}^{2\pi}\exp\left(\frac{\nu_r+\alpha_T\int triang(x)dx}{\nu_m}\right)d\left(R_T\tau\right)\\
&\quad=\int_{-R_T\tau_1}^{0}\exp\left(\left(\frac{\nu_r}{\nu_m}-\frac{\pi\alpha_T}{4\nu_m}\right)+\frac{\alpha_T}{\pi\nu_m}x^2\right)dx\\
&\quad=\exp\left(\frac{\nu_r}{\nu_m}-\frac{\alpha_T}{\nu_m}\frac{\pi}{4}\right)\frac{\pi}{2}\sqrt{\frac{\nu_m}{\alpha_T}}\left[erfi\left(0\right)+erfi\left(\sqrt{\frac{\pi\alpha_T}{4\nu_m}}-\frac{\nu_r}{\nu_m}\right)\right]
\end{aligned}
\tag{B.5}
$$

$$
\begin{aligned}
&\int_0^{2\pi} \exp\left(-sign(v_r)\frac{\alpha_T}{v_m}\int triang(x)dx \right) d(R_T\tau) \\
&\quad = \int_{-\pi/2}^{\pi/2} \exp\left(-sign(v_r)\left[\frac{\alpha_T}{v_m}\left(-\frac{\pi}{4} + \frac{(R_T\tau)^2}{\pi} \right) \right] \right) d(R_T\tau) \\
&\qquad + \int_{-\pi/2}^{\pi/2} \exp\left(-sign(v_r)\left[\frac{\alpha_T}{v_m}\left(\frac{\pi}{4} - \frac{(R_T\tau)^2}{\pi} \right) \right] \right) d(R_T\tau) \\
&\quad = \int_{-\pi/2}^{\pi/2} \exp\left(\frac{\pi\alpha_T}{4v_m} - \frac{\alpha_T}{\pi v_m}(R_T\tau)^2 \right) + \exp\left(-\frac{\pi\alpha_T}{4v_m} + \frac{\alpha_T}{\pi v_m}(R_T\tau)^2 \right) d(R_T\tau) \\
&\quad = \pi\sqrt{\frac{v_m}{\alpha_T}}\left[\exp\left(\frac{\pi\alpha_T}{4v_m} \right) erf\left(\sqrt{\frac{\pi\alpha_T}{4v_m}} \right) + \exp\left(-\frac{\pi\alpha_T}{4v_m} \right) erfi\left(\sqrt{\frac{\pi\alpha_T}{4v_m}} \right) \right]
\end{aligned}
\tag{B.6}
$$

where the function $erfi(.)$ is the imaginary error function, defined as

$$
erfi(x) \equiv \frac{2}{\sqrt{\pi}} \int_0^x e^{t^2} dt \tag{B.7}
$$

and can be expressed as a series of odd polynomials

$$
erfi(x) = \frac{2}{\sqrt{\pi}} \sum_{k=0}^{\infty} \frac{x^{2k+1}}{k!(2k+1)} \tag{B.8}
$$

Its derivative is given by

$$
\frac{\partial erfi(x)}{\partial x} = \frac{2}{\sqrt{\pi}} e^{x^2} \tag{B.9}
$$

Therefore, the effective friction characteristic in the case of triangular waveforms can be expressed using equations (B.3) to (B.6) into (3.36)

$$\bar{\mu}(v_r)=\left\{\alpha_0\left(1-\sqrt{1-\frac{4|v_r|}{\pi\alpha_T}}\right)+\frac{\alpha_1}{2}\sqrt{\frac{v_m}{\alpha_T}}\exp\left(-\frac{|v_r|}{v_m}-\gamma\right)\right.$$
$$\times\left(erf\left(\sqrt{\gamma}\right)-erf\left(\sqrt{\gamma-\frac{|v_r|}{v_m}}\right)+erfi\left(\sqrt{\gamma}\right)\right) \qquad for\,|v_r|\le\frac{\pi}{4}\alpha_T \quad \text{(B.10a)}$$
$$\left.-\frac{\alpha_1}{2}\sqrt{\frac{v_m}{\alpha_T}}\exp\left(\frac{|v_r|}{v_m}-\gamma\right)erfi\left(\sqrt{\gamma-\frac{|v_r|}{v_m}}\right)\right\}sign(v_r)$$

$$\bar{\mu}(v_r)=sign(v_r)\left\{\alpha_0+\frac{\alpha_1}{2}\exp\left(-\frac{|v_r|}{v_m}\right)\sqrt{\frac{v_m}{\alpha_T}}\right.$$
$$\left.\times\left[\exp(\gamma)erf\left(\sqrt{\gamma}\right)+\exp(-\gamma)erfi\left(\sqrt{\gamma}\right)\right]\right\} \qquad for\,|v_r|\ge\frac{\pi}{4}\alpha_T \quad \text{(B.10b)}$$

where $\gamma=\dfrac{\pi\alpha_T}{4v_m}$.

APPENDIX C - SQUARE WAVEFORMS

Square waveforms can be expressed as

$$g(x) = sqr(x) = \begin{cases} 1 & for\ 0 \le x \le \pi \\ -1 & for\ \pi < x \le 2\pi \end{cases} \tag{C.1}$$

The integral of this signal is given by

$$G(x) = \int sqr(x)dx = \begin{cases} -\frac{\pi}{2} + x & for\ 0 \le x \le \pi \\ \frac{3\pi}{2} - x & for\ \pi < x \le 2\pi \end{cases} \tag{C.2}$$

Using equation (C.2) into (3.36) leads to the following integrals

$$\begin{aligned} \int_0^{R_T\tau_1} \exp\left(\frac{v_r + \alpha_T \int sqr(x)dx}{v_m} \right) d(R_T\tau) &= \frac{v_m}{\alpha_T}\left[\exp\left(\frac{v_r}{v_m} + \frac{\alpha_T}{v_m}\left(x - \frac{\pi}{2} \right) \right) \right]_0^{R_T\tau_1} \\ &= \frac{v_m}{\alpha_T}\left[1 - \exp\left(\frac{2v_r - \pi\alpha_T}{2v_m} \right) \right] \end{aligned} \tag{C.3}$$

$$\begin{aligned} &\int_{R_T\tau_1}^{R_T\tau_2} \exp\left(-\frac{v_r + \alpha_T \int g(x)dx}{v_m} \right) d(R_T\tau) \\ &= -\frac{v_m}{\alpha_T}\left[\exp\left(-\frac{v_r}{v_m} - \frac{\alpha_T}{v_m}\left(x - \frac{\pi}{2} \right) \right) \right]_{R_T\tau_1}^{\pi} + \frac{v_m}{\alpha_T}\left[\exp\left(-\frac{v_r}{v_m} - \frac{\alpha_T}{v_m}\left(\frac{3\pi}{2} - x \right) \right) \right]_{\pi}^{R_T\tau_2} \\ &= 2\frac{v_m}{\alpha_T}\left[1 - \exp\left(-\frac{2v_r + \pi\alpha_T}{2v_m} \right) \right] \end{aligned} \tag{C.4}$$

$$\int_{R_T\tau_2}^{2\pi} \exp\left(\frac{v_r+\alpha_T\int g(x)dx}{v_m}\right)d\left(R_T\tau\right)=-\frac{v_m}{\alpha_T}\left[\exp\left(\frac{v_r}{v_m}+\frac{\alpha_T}{v_m}\left(\frac{3\pi}{2}-x\right)\right)\right]_{R_T\tau_2}^{2\pi}$$
$$=\frac{v_m}{\alpha_T}\left[1-\exp\left(\frac{2v_r-\pi\alpha_T}{2v_m}\right)\right] \qquad \text{(C.5)}$$

$$\begin{aligned}&\int_0^{2\pi}\exp\left(-sign\left(v_r\right)\frac{\alpha_T}{v_m}\int sqr(x)dx\right)d\left(R_T\tau\right)=\\&=-sign\left(v_r\right)\frac{v_m}{\alpha_T}\left[\exp\left(-sign\left(v_r\right)\frac{\alpha_T}{v_m}\left(x-\frac{\pi}{2}\right)\right)\right]_0^{\pi}\\&+sign\left(v_r\right)\frac{v_m}{\alpha_T}\left[\exp\left(-sign\left(v_r\right)\frac{\alpha_T}{v_m}\left(\frac{3\pi}{2}-x\right)\right)\right]_{\pi}^{2\pi}\\&=2sign\left(v_r\right)\frac{v_m}{\alpha_T}\left[\exp\left(sign\left(v_r\right)\frac{\pi\alpha_T}{2v_m}\right)-\exp\left(-sign\left(v_r\right)\frac{\pi\alpha_T}{2v_m}\right)\right]\end{aligned} \qquad \text{(C.6)}$$

Therefore, the effective friction characteristic in the case of triangular waveforms can be expressed using equations (C.3) to (C.6) into (3.36)

$$\bar{\mu}\left(v_r\right)=\frac{2\alpha_0}{\pi\alpha_T}v_r+\frac{2\alpha_1}{\pi}\frac{v_m}{\alpha_T}\exp\left(-\frac{\pi\alpha_T}{2v_m}\right)\sinh\left(\frac{v_r}{v_m}\right) \qquad for\left|v_r\right|\le\frac{\pi}{2}\alpha_T \qquad \text{(C.7a)}$$

$$\bar{\mu}\left(v_r\right)=sign\left(v_r\right)\left\{\alpha_0+\frac{2\alpha_1 v_m}{\pi\alpha_T}\exp\left(-\frac{\left|v_r\right|}{v_m}\right)\sinh\left(\frac{\pi\alpha_T}{2v_m}\right)\right\} \quad for\left|v_r\right|\ge\frac{\pi}{2}\alpha_T \qquad \text{(C.7b)}$$

REFERENCES

1. ASME, *Research Needs and Opportunities in the Area of Interaction of Friction and System Dynamics*, . 1994.

2. ASME, *Research Needs and Opportunities in the Area of Friction and System Dynamics*, . 1997.

3. Kinkaid, N.M., O.M. O'Reilly, and P. Papadopoulos, *Automotive disc brake squeal.* Journal of Sound and Vibration, 2002. **267**(1): p. 105-166.

4. Mottershead, J.E., *Vibrations and Friction-Induced Instability in Discs.* Dynamics with Friction: Modeling, Analysis, and Experiment, Part II, 2001. **Vol. 7**(Series on Stability, Vibration, and Control of Structures, World Scientific Publishing): p. p. 29-74.

5. Haynes, J.H., *The Haynes Automotive Brake Manual*. 1994, Somerset, England: Haynes Publishing Group.

6. Mills, H.R., *Brake Squeak.* Technical Report 9000 B, Institution of Mechanical Engineers, 1938.

7. Spurr, R.T., *Brake Squeal.* The Institute of Mechanical Engineers-Vibration and Noise in Motor Vehicles, 1972. **C95/71**: p. 13-16.

8. Spurr, T.R., *A theory of Brake Squeal.* Proceedings of the Automobile Division, Institution of Mechanical Engineers, 1961. **1**: p. p. 33-52.

9. Iwan, W.D. and K.J. Stahl, *The Response of an Elastic Disk With a Moving Mass System.* Journal of Applied Mechanics, Transactions ASME, 1973. **40**(2): p. 445-451.

10. Iwan, W.D. and T.L. Moeller, *The Stability of a Spinning Elastic Disk With a Transverse Load System.* Transactions of the ASME. Series E, Journal of Applied Mechanics, 1976. **43**(September 1976): p. 485-490.

11. Fieldhouse, J.D. and P. Newcomb, *The Application of Holographic Interferometry to the Study of Disc Brake Noise*, in *SAE Paper 9830805*. 1998.

12. Ichiba, Y. and Y. Nagasawa, *Experimental Study On Disc Brake Squeal*, in *SAE Paper 930802*. 1993.

13. Rye, R., *Investigation of Brake Squeal via Sound Intensity and Laser Vibrometry*, . 2000, Georgia Institute of Technology.

14. Sherif, H.A., *Experimental Investigation of Self-Excited Squeal*, in *SAE Paper 892451*. 1989.

15. Ikeuchi, T., *Anti-Squeal Shim In A Disc Brake*, . 1988: US.

16. Yano, K., *Shim for Preventing Brake Squeal In a Disk Brake*, . 1998: US.

17. Fieldhouse, J.D. and M. Rennison. *The value of noise fix shims, a case study*. in *Second International Seminar on Automitive Braking*. 1998: Professional Engineering Publishing, London.

18. Brosilow, J.L., *Shim Structure For Sound Dampening Brake Squeal Noise*, . 1996: US.

19. Heppes, P. *Noise Insulators for Brake Squeal Reduction - Influence and Selection of the Damping Material*. in *The Second International Seminar On Automotive Braking*. 1998: Professional Engineering Publishing Limited.

20. Nishizawa, Y., *Vibration Damping Device*, . 1999: United States.

21. Earles, S.W.E. and P.W. Chambers, *Disc brake squeal noise generation: predicting its dependency on system parameters including damping.* International Journal of Vehicle Design, 1987. **8**(4/5/6): p. 538-552.

22. Ibrahim, R.A., *Friction-Induced Vibration, Chatter, Squeal, and Chaos- Part I: Mechanics of Contact and Friction; - Part II: Dynamics and Modeling.* Applied Mechanics Reviews, 1994. **47**(7): p. 209-253.

23. Nishizawa, Y., H. Saka, and S. Nakajima, *Development of an Electronically Controlled Disc Brake Noise Canceling System.* SEI Technical Review, 1998(45): p. 145-151.

24. Graf, A., *Active Control of Automotive Disc Brake Rotor Squeal Using Dither*, in *Mechanical Engineering*. 2001, Georgia Institute of Technology: Atlanta.

25. Armstrong-Hélouvry, B., P. Dupont, and C. Canudas De Wit, *A Survey of Models, Analysis Tools and Compensation Methods for the Control of Machines with Friction.* Automatica, 1994. **30**(7): p. 1083-1138.

26. Cunefare, K.A. and A.J. Graf, *Experimental active control of automotive disc brake rotor squeal using dither.* Journal of Sound and Vibration, 2002. **250**(4): p. 579-590.

27. Badertscher, J., *Experimental Investigation of Dither Control on Effective Braking Torque*, in *Mechanical Engineering*. 2005, Georgia Institute of Technology: Atlanta. p. 56.

28. Khalil, H.K., *Nonlinear Systems*. 1992: Macmillan. 564.

29. Jordan, D.W. and P. Smith, *Nonlinear Ordinary Differential Equations: An Introduction to Dynamical Systems*. 3rd edition (August 1, 1999) ed. Oxford Applied and Engineering Mathematics. 1977: Oxford University Press. 550.

30. Oldenburger, R., *Signal Stabilization of a Control System.* ASME Transactions, 1957. **79**(8): p. 1869-72.

31. Oldenburger, R. and T. Nakada, *Signal Stabilization of Self-Oscillating Systems.* IRE Transactions on Automatic Control, 1961(September): p. 319-325.

32. Oldenburger, R. and R.C. Boyer, *Effetcs of Extra Sinusoidal Inputs to Nonlinear Systems.* Transaction of the ASME - Journal of Basic Engineering, 1962(December): p. 559-570.

33. Gelb, A. and W. Vander Velde, *Multiple-Input Describing Functions and Non-Linear System Design*. 1968, New York: McGraw-Hill.

34. Meerkov, S.M., *Vibrational Control Theory.* Journal of the Franklin Institute, 1977. **303**(2): p. 117-128.

35. Meerkov, S.M., *Principle of Vibrational Control: Theory and Applications.* IEEE Transactions on Automatic Control, 1980. **AC-25**: p. 755-762.

36. Canudas de Wit, C. and A. Pervozvanski, *Vibrational Smoothing in Systems with Dynamic Friction.* Nonlinear Control Systems Design, 1998.

37. Canudas de Wit, C. and A. Pervozvanski, *Asymptotic analysis of the dither effect in systems with friction.* Automatica, 2002. **38**(1): p. 105-113.

38. Armstrong-Hélouvry, B., *Control of Machines with Friction*. 1991, Norwell, MA: Kluwer Academic Publishers.

39. Morgul, O., *On the control of chaotic systems in Lur'e form by using dither.* IEEE Transactions on Circuits and Systems I: Fundamental Theory and Applications, 1999. **46**(10): p. p 1301-1305.

40. Morgül, O., *On The Control of Some Chaotic Systems by Using Dither.* Physics Letters A, 1999. **262**(2-3): p. 144-151.

41. Thomsen, J.J., *Using fast vibrations to quench friction-induced oscillations.* Journal of Sound and Vibration, 1999. **228**(5): p. 1079-1102.

42. Thomsen, J.J., *Some general effects of strong high-frequency excitation: stiffening, biasing and smoothening.* Journal of Sound and Vibration, 2002. **253**(4): p. 807-831.

43. Thomsen, J.J. and A. Fidlin, *Analytical Approximations For Stick-Slip Vibration Amplitude.* International Journal of Non-Linear Mechanics, 2003. **38**: p. 389-403.

44. Shin, K., *et al.*, *Analysis Of Disc Brake Noise Using A Two-Degree-Of-Freedom Model.* Journal of Sound and Vibration, 2002. **254**(5): p. 837-848.

45. Chen, J.-S. and D.B. Bogy, *Mathematical Structure of Modal Interactions in a Spinning Disk-Stationary Load System.* Journal of Applied Mechanics, 1992. **59**(june 1992): p. 390-397.

46. Ono, K., J.-S. Chen, and D.B. Bogy, *Stability Analysis for the Head-Disk Interface in a Flexible Disk Drive.* Journal of Applied Mechanics, 1991. **58**(december 1991): p. 1005-1014.

47. Ouyang, H., *et al.*, *Friction-Induced Parametric resonances in Discs: Effect of a negative Friction-Velocity Relationship.* Journal of Sound and Vibration, 1998. **209**(2): p. p. 251-264.

48. Dzirasa, M., *Eperimental Investigation of Dither Control for the Suppression of Automotive Brake Squeal*, in *Mechanical Engineering*. 2002, Georgia Institute of Technology: Atlanta.

49. Chen, J.-S. and D.M. Bogy, *Effects of a space-fixed friction force on the in-plane stress and stability of transverse vibrations of a spinning disk.* Journal of Applied Mechanics, Transactions ASME, 1993. **60**(3): p. 646-648.

50. Vogel, S.M. and D.W. Skinner, *Natural Frequencies of Transversely Vibrating Uniform Annular Plates.* ASME Journal of Applied Mechanics, 1965. **32**(December): p. 926-931.

51. Chan, S.N., J.E. Mottershead, and M.P. Cartmell, *Parametric resonances at subcritical speeds in discs with rotating frictional loads.* Proceedings of the Institution of Mechanical Engineers, Part C: Journal of Mechanical Engineering Science, 1994. **208**(6): p. 417-425.

52. Nayfeh, A.H. and D.T. Mook, *Nonlinear Oscillations*. Reprint edition (March, 1995) ed. Wiley Classics Library. 1979: Wiley-Intersciences. 720.

53. Shen, I.Y., *Response of a stationary, damped, circular plate under a rotating slider bearing system.* Journal **of** Vibration, Acoustics, Stress, and Reliability in Design, 1993. **115**(1): p. 65-69.